APPLAuSE

review letters

Magnetic reconnection in astrophysical and laboratory plasma

Fast and Heavy - review of target normal sheath acceleration
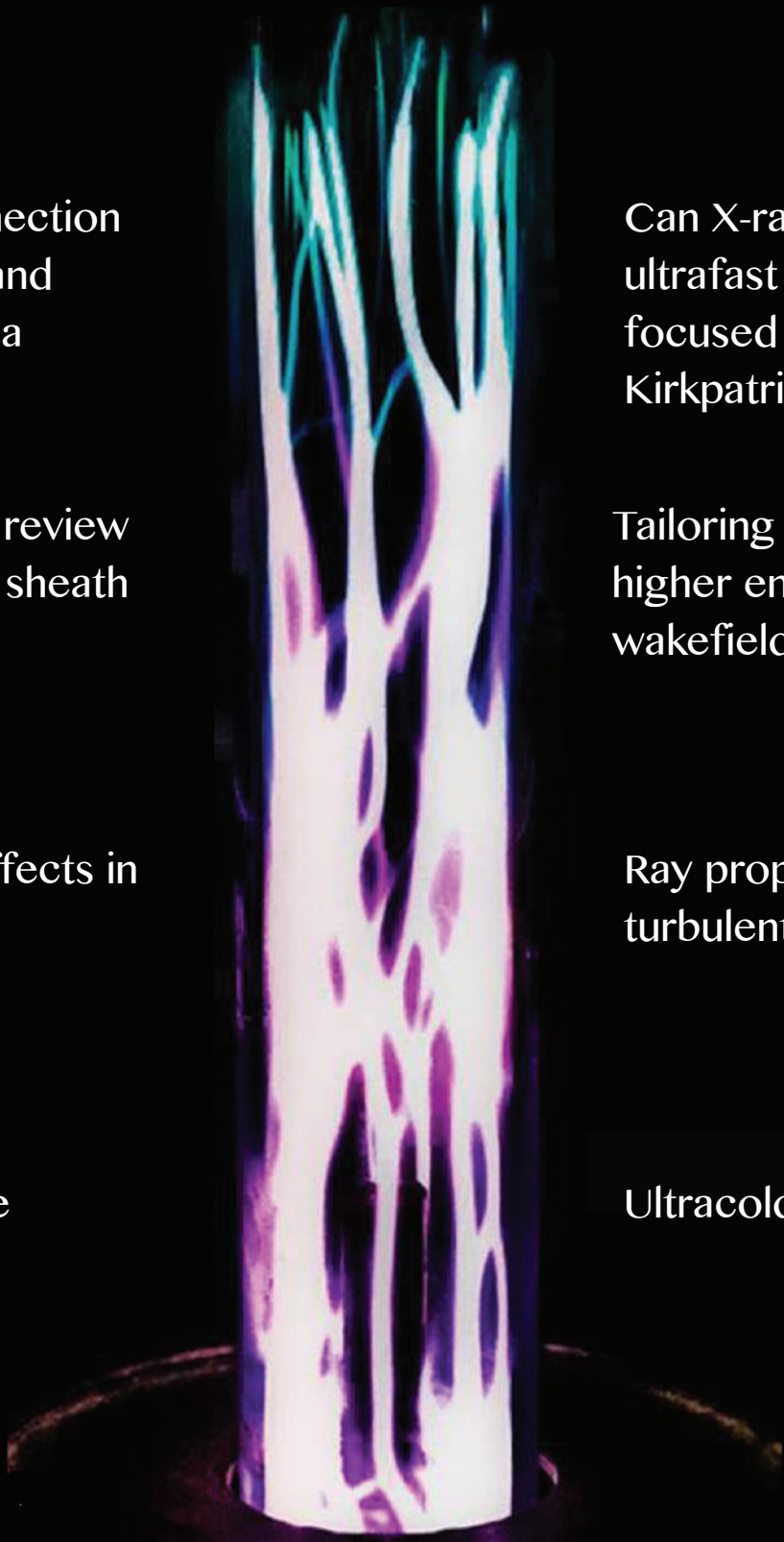
Strong gravity effects in ideal plasmas

Low temperature plasma medicine

Can X-ray pulses of ultrafast microscopy be focused with a Kirkpatrick-Baez optic?

Tailoring plasma towards higher energy quality wakefield accelerators

Ray propagation on turbulent media

Ultracold neutral plasmas

APPLAuSE Review Letters

As Part of the Intensive Course on

TRANSVERSE SKILLS

Organized and Supervised by

Dr. Marta Fajardo

Guest Editor

Rogério Jorge

Cover/Back Pages

Giannandrea Inchingolo

ARL

2015

Editor foreword

Welcome to the inaugural issue of APPLAUSE Review Letters: a peer-refereed academic journal on Advances on Plasma Physics. This journal is the result of an intensive module on Transverse Skills of the APPLAUSE Doctoral Program, a course designed to improve the APPLAUSE students academic achievement. The papers presented in the APPLAUSE Review Letters show review work on selected topics, or advances made during the Laboratory Rotations hosted by teams from the Instituto de Plasmas e Fusão Nuclear (IPFN). These papers were presented as part of the summer assignment for the course, and refereed by students and senior researchers from IPFN, who generously gave their time to the course, and to whom we are very grateful. This year's course benefited from the pioneering work led by the first APPLAUSE cohort in 2014, whom the Editors would also like to thank.

This years Guest Editor is Rogério Jorge, the 2015 cohort's Delegate, to whom we are indebted for putting together the magazine, and for instituting the Best Figure Award. We would also like to thank Giannandrea Inchingolo for the cover page, and all the 2015 APPLAUSE students for the work carried out for the course.

We hope that the APPLAUSE Review Letters will inspire next years cohort, by showcasing the level of maturity that could be reached, in a such a tight schedule, by first year PhD students. As the coordinator of the module, it was my pleasure and my privilege to work with the 2015 APPLAUSE students.

Marta Fajardo
Instituto de Plasmas e Fusão Nuclear, Instituto Superior Técnico, Lisboa
E-mail address: marta.fajardo@tecnico.ulisboa.pt
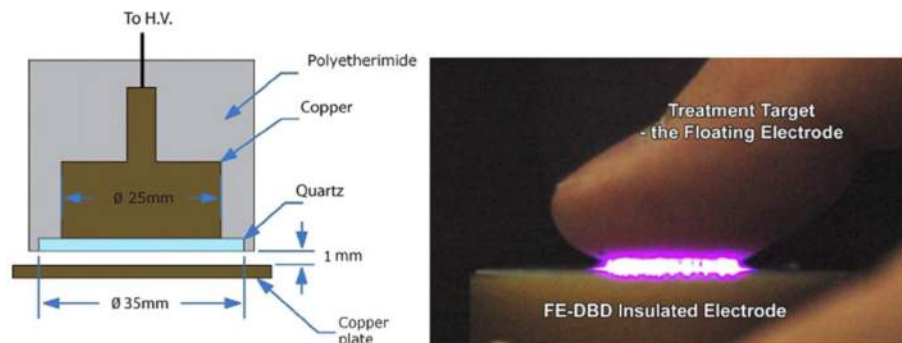
Best Figure Award

Figure 1. Marija - Fridman G et. al, Plasma Chem. Plasma Process. 26 (4) (2006)

We are glad to announce that this year's Best Figure Award goes to Marija Grofulović!

Looking for a figure that could summarize the purpose of the Applause Review Letters, we have found that Marijas selection of works by *Fridman G et. al, Plasma Chem. Plasma Process. 26 (4) (2006)* not only clearly depicts the technical details on the production of the plasma, but also shows an important, direct application.

Contents

Magnetic Reconnection in Astrophysical and Laboratory Plasmas

Adwiteey hails from Orai,Uttar Pradesh, northern India. He obtained his BS-MS Dual degree from the Indian Institute of Science Education and Research, Pune. He completed his graduation in Basic Sciences in 2014. He carried his master thesis entitled Study of tokamak Equilibria using variation moment method at the Institute for Plasma Research, Gandhinagar, India. He then spent another six months there to further develop a free boundary code for PF coils optimization.

He has a strong interest in computational physics and plasma physics. He has done internships at several institutes in India during his dual degree, where he gradually developed his interest in computational and plasma physics. These covered various topics such as data analysis of solar coronographs, formulating rhelogical flow, MHD turbulence, CMEs dynamics study, and Tokamak PF coils optimization.

Adwiteey received the prestigious KVPY fellowship for his dual degree course, and has co-authored several conference proceedings and a paper in The Astrophysical Journal. His hobbies lie in programming, trekking and sketching.

Adwiteey Mauriya

Instituto de Plasmas e Fusão Nuclear (IPFN), Instituto Superior Técnico,
Avenida Rovisco Pais, 1049-001 Lisboa, Portugal

E-mail: `amauriya@ipfn.ist.utl.pt`

September 2015

Abstract. In this review article, fundamentals of reconnection theory, it's application and observations from space satellites have been discussed. Magnetic reconnection is a topological rearrangement of magnetic field lines that leads to conversion of magnetic energy to other form of macroscopic energies such as flow and thermal energies. From Astrophysical flares to earth's magnetosphere and γ ray bursts to saw tooth crashes in laboratory, all are driven by reconnection. Reconnection is necessary for dynamos and large scale restructuring which is known as magnetic self-organization. After the brief description of reconnection process, experimental and theoretical works are discussed.

1. Introduction

Many of activities in universe are observed through magnetic fields e.g. Earth's magnetosphere, solar corona. It ranges from interstellar medium to galactic clusters. Magnetic reconnection is topological transformation of magnetic field lines, restructure magnetic energy of plasmas to macroscopic quantities such as flow and thermal energies. Magnetic energy is the primary source to drive these processes to convert through magnetic reconnection.Magnetic reconnection occurs in generation and evolution of stars, accretion disks, galactic clusters. Magnetic reconnection has been observed in laboratory as well. In laboratory it plays a key role to confine fusion plasmas by restructuring plasma current profiles.

For example, In sawtooth oscillations, plasma current profile rearrange current profiles periodically through magnetic reconnection. It is seen in evolution of solar flares, coronal mass ejection and interaction of solar winds in earth's magnetosphere and is reckoned to be the cause of formation of stars([8][30][5] [9])

Magnetic reconnection can be visualized in solar flares which have been investigated for more than half century. In figure 1 global topology of plasma currents of solar flares can be visualized[34] [35] [11] [21] [12]. Figure 1 has been taken in soft x-ray regime. Figure 1 is formed from Transition Region And Coronal Explorer (TRACE) satellite data [21].

Figure 1: Image of solar flare at 17.1 nm from TRACE satellite on 9 November 2000. From apod.nasa.gov

Conventionally, reconnection is described through Magnetohydrodynamics (MHD). In ideal case magnetic field lines are frozen in plasma along with flux conservation. Breakdown of frozen flux condition occurs during reconnection and its time scale is relatively shorter than plasma's classical diffusion time based on electron-ion collision. Magnetic field lines are frozen in whole region except where it breaks. In this review article we discuss about collisionless non-MHD regime, and its recent developments of two fluid physics. We have further discussed the magnetic anisotropy incorporated by magnetic fields.

2. Magnetic Reconnection

So the raised question is How do magnetic field lines reorganize in plasma? Ideal MHD describes dynamics of conducting plasma, where electric field parallel to magnetic field lines $E_\parallel$ vanishes ([28],[27][37], [18]) So magnetic field lines always move with plasma and remains intact. If the magnetic field lines intersect each other in plasma as in figure 2 then associated field gradients become strong at intersection point. Field lines
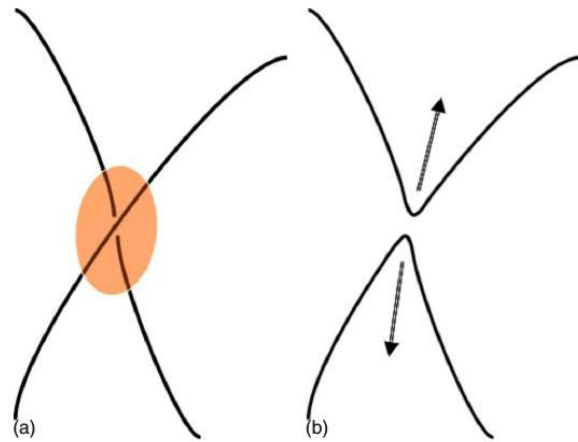
Figure 2: Cartoon of magnetic reconnection [41]

emerges at intersection point and forms singular current density sheet which triggers magnetic field lines to lose their identity. [7] showed that new current sheet formed by merging of magnetic field lines near X point of figure 3 and rejoined in current sheet. After field
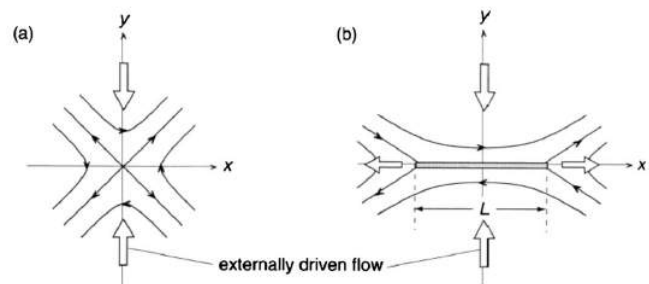

Figure 3: Current sheet formation through externally driven flow [13]

lines are reconnected, topology of magnetic configu-

ration of plasma changes lorentz force $\vec{J} \times \vec{B}$ and it converts the magnetic energy to other form of energy such as kinetic energy. Here is an important example shown in figure 4, depicts the interaction of solar wind with earth's magnetosphere. As we can see in the figure 4 solar wind lines are different from earth's magnetosphere, it is impossible for solar winds to penetrate earth's magnetosphere. It reconnects with earth's magnetic field lines and self-reorganises the emerged magnetic field lines in different fashion. This is how magnetic reconnection changes any astrophysical activity. Since plasma in solar wind is not infinitely conducting although conductivity is very high. So magnetic field lines of solar winds get attached to earth's magnetosphere and allow it to penetrate the magnetosphere. As a result cosmic rays enters into the atmosphere that
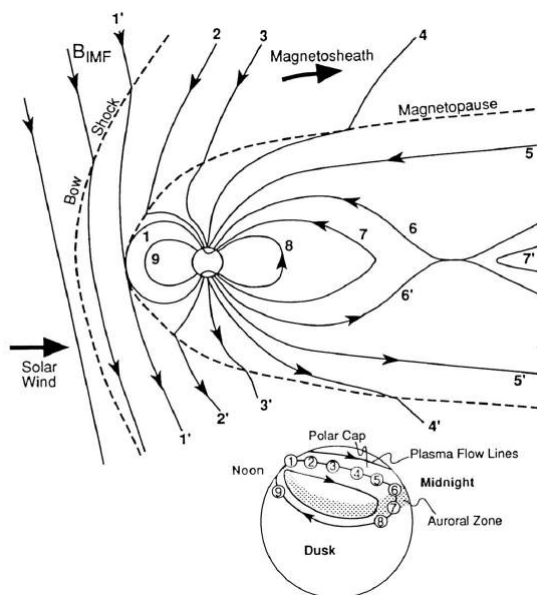

Figure 4: schematic picture of earth magnetosphere's cross section view interacting with solar wind. Solar wind magnetic field line($1^{'}$) connects with earth's magnetic field line(1) at magnetopause emerged earth's magnetic field lines 6 and $6^{'}$ connects at X point at tail ([39])

can be directly observed.
There have been plenty of research work proceeded since last 50 years about physical process occur at kinetic scale. Lots of experiments, simulation and observation into space was done to understand reconnection. In the beginning it was tried to explain through ideal MHD case but observed reconnection rates of any activities were not sufficed for fast reconnection rate event. As a result, more sophisticated physics were developed to gain better insight.
In later years, to understand the physics of magnetic reconnection, it got bifurcated in three streams of re-

search interests: laboratory experiments, astrophysical plasmas, theory and numerical simulations. Observations in space and experiments performed for fusion plasmas led to the motivation for fundamental research in reconnection. Theory and numerical simulations breakdown the process of complex reconnection process in smaller pieces to gain better insight at small simpler process. Magnetic fusion experiments vitalize the fundamental of reconnection physics by measuring key plasma parameters at many points in the reconnection region ([24]). In contrast, space satellites provide only few points in reconnection region of flares. So proposed experiments for understanding reconnection possess a mediator between space observation and theoretical development ([27]). Due to advancing technology of data acquisition of space satellite probes, it allows us to observe parameters with better resolution. As an example, there are 30 magnetic probes located in magnetic reconnection experiment (MRX) ([26] [23])
After discussing observation and experiments on magnetic reconnection in section 3 section 4, we explain more about well known theories of magnetic reconnection in section 5. There are two steady state MHD theories of slow and fast reconnection. One theory is for spontaneous, time dependent MHD reconnection initiated by tearing mode instability.

3. Space observation to understand Reconnection

3.1. Reconnection in solar corona

Magnetic reconnection changes the magnetic topology along with converting magnetic energy to kinetic energy as it dissipates the electron's energy with ohmic heating and since ions are heavier it dissipates ion's energy to alfvenic jets. Magnetic reconnection have played a major role in studying dynamics of solar corona, solar flares, prominence and coronal mass ejections (CMEs) ([8] [35][9]) But solar flares were always the main area of interest of research. Earlier solar flares were defined as flash of high intensity beam in chromosphere in $H\alpha$ region. Through spectroscopic measurements of photosphere of sun, showed the presence of both positive and negative polarities in flares. Several space observatories i.e. SMM, Yohkoh, SOHO, TRACE, RHESSI and Hinode are observing interstellar space including sun at span of wavelengths from γ rays to radio waves with high temporal and spatial resolution and various spectroscopic measurements. Review of flare physics have been discussed in ([2][32][29][6][33][16]). Large coronal loops changes their magnetic topology in figure 1 in very short time scale of few minutes. Reconnection considered to occur in solar corona because its temperature is higher

than photoshpere. One of the main unsolved problem in solar physics is to investigate the cause of coronal heating ([17]). As magnetic energy being dominated in solar corona that motivates to understand magnetic reconnection mechanism.

On the other hand, magnetic field changes rapidly in photoshpere. Magnetic flux on photosphere completely changes in every 14 hours ([22]) which was investigated in lower corona through SOHO data. Reconnection time in photosphere was found to be 1.5 hours. It infers that reconnection rate is quite high. There have been several models proposed ([29]) proposed tectonics model in which gradient of current sheets form at the separatrix of corona which resembles earth's tectonic plates.

Coronal mass ejections (CMEs) are massive eruption of ionized gas and magnetic flux from corona to interplanetary space. They are result of shifting the magnetic topology of coronal magnetic fields. A generic CME contains approximately 10^{15} Weber of magnetic flux and 10^{13} Kilograms of plasma. Usually one CME is observed each day when solar atmosphere is very active. Magnetic reconnection occurs at the foot of CME to detach it from corona.

3.2. Reconnection on earth's magnetosphere

Earth's magnetosphere forms through the liquid metal at core of earth which acts like a dynamo and generates the magnetic field. Solar winds are plasma particles which erupts from sun. It travels towards earth and interact with magnetosphere. It reconnects with the magnetic field lines of earth's magnetosphere in figure 4. Where magnetic field lines are in opposite direction they cancel each other and form neutral current sheets. It can be seen in the day(magnetopause) as well as at night(magnetotail) in figure 4 [37] [18][20] where solar wind's magnetic field lines connects with earth's magnetic field lines. It is formed all around the earth. Through satellite observation it was found that current sheet thickness of magnetosphere is of the order of ion's skin depth or ion gyroradius. Typically ion skin depth in magnetosphere is of the order of 100-200 km but it is 10 times even larger at magnetotail. In this scenario MHD theory (which is basically fluid theory) can't describe reconnection. It can be described through two-fluid physics and kinetic approach because of electron's and ion's different behaviour at reconnection region. So reconnection could be turbulent in both spatial and temporal scales because drift of electrons and ions can lead to electromagnetic or electrostatic fluctuations. There are some observations at magnetotail which were turbulent in nature.

4. Reconnection in laboratory plasmas

Many experiments were performed to investigate magnetic reconnection in 70s. In the beginning, short pulse pinch experiments were performed ([3][36] [14]). It was conducted in collisional plasma. In 1979 some more experiments were performed by ([31]) in less collisional plasma and strong field. However these experiments could not produce the same condition as space plasma where global structure is governed by MHD theory.

A large amount of reconnection events have been observed in fusion plasma research. Mostly, magnetic confinement fusion research experiments performed in toroid shaped plasma device (Tokamak) which satisfy the MHD conditions. Magnetic fields in fusion plasma generated by internal plasma currents by producing pinch forces to confine high pressure plasma in tokamak. Toroidal currents are used to heat and confine the plasma. This kind of confinement mechanism is applied in Tokamak, Spheromak, reversed field pinch (RFP) and field reversed configuration (FRC). Magnetic reconnection mechanism plays a crucial role in achieving plasma equilibrium in this type of confinement mechanism. In tokamak, magnetic reconnection
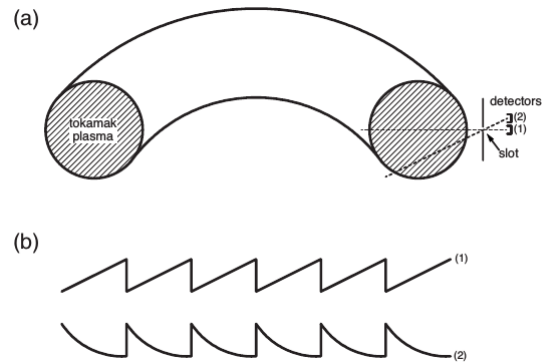

Figure 5: a) Schematic diagram of tokamak's cross section with two inner and outer chord, b) Soft X ray signals obtained from probe 1 and 2. It denotes the profile of electron's temperature in plasma [41]

occurs in sawtooth oscillations of plasmas at very high lundquist number ($\sim 10^7$).Sawtooth oscillations was discovered by ([38]) in tokamak plasma. It is observed as typical oscillation in which there is a peak and sudden flattening in electron temperature (T_e) in minor cross section of tokamak, shown in figure 5 ([1][19]).

In tokamak plasma, MHD stability is measured by safety factor q. Moreover, in axis symmetric tokamak, each nested magnetic flux surfaces considered to have constant electron temperature (figure 6) and peak currents are slightly higher because of electron electron collision becomes prominent in this case. This makes plasma unstable and forms MHD kink mode. That he-

lically formed flux surface at $q = 1$ triggers magnetic reconnection, shown in figure 6. This reconnection leads to structural rearrangement of flux surfaces by converting magnetic energy to other forms. [1] found that reconnection event at q=1 leads to uniform current density of plasma and constant electron temperature profile Many experiments have been conducted to
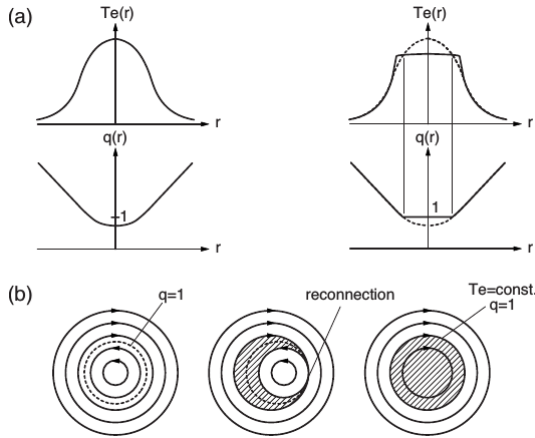

Figure 6: a) Schematic diagram of temperature profiles and safety factors of electrons in poloidal plane of tokamak during sawtooth oscillations. b) Pictorial representation of kadomstov model in poloidal plane at m=1, n=1 as MHD instability develops at q=1 configurations which leads to magnetic reconnection [1] [41]

.

understand more about magnetic reconnection in these fusion devices to confine and control plasmas. In these devices magnetic reconnection depends globally on its 3D geometry and plasma parameters of reconnection region.

5. Theoretical study of reconnection

Theoretical study of reconnection consists of its analytical development and numerical simulation. In this review article we are more focused on analytical insight than numerical counterparts. In this section we briefly describe theoretical models of reconnection, its time dependent effects and instabilities.

5.1. Sweet Parker theory

Parker(1957) and Sweet (1958) proposed a model of magnetic reconnection in which there is local flow of plasma in reconnection region towards diffusion region. In simpler term, two oppositely directed magnetic fields in reconnection region of plasma density ρ and conductivity σ balance each other at neutral line at

speed v_{in} at characteristic distance $2L$, shown in figure 7. At the center of neutral line there is null point with width 2δ. After reconnection emerged plasma move out at speed v_{out}. It is one of very simple case, is known as steady state reconnection. Sweet
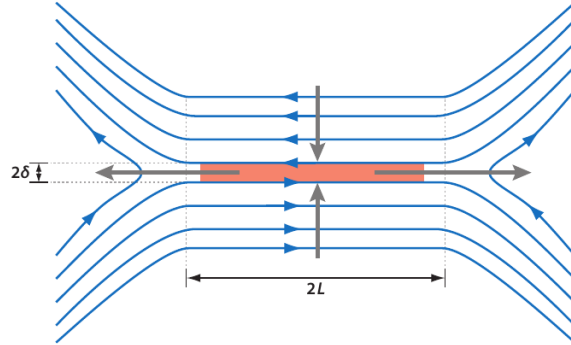

Figure 7: Schematic diagram of magnetic field lines in sweet parker reconnection theory. Anti parallel magnetic fields are at characteristic lengths $2L$ and reconnects in diffusion region of width 2δ

parker theory predicts the reconnection rate and based on three principles a) Outflow speed is alfven speed in gaussian unit $v_A = B/\sqrt{4\pi\rho}$. We assume that magnetic energy get converted to kinetic energy by resistive heating, which is the cause of rise in magnetic tension force and results in bending of field lines at X point. This accelerates the fluid to roughly at v_A. b) Conservation of mass. It verifies through $v_{in}L = v_{out}\delta$, here $v_{out} = v_A$ c) Electric field E is perpendicular to plane of flow and it follows resistive MHD forms with non zero resistivity.

$$\vec{E} = -\frac{v \times \vec{B}}{c} + \frac{\vec{J}}{\sigma} \tag{1}$$

In reconnection region circulation of $\vec{E}$ vanishes so electric field at X point and in upstream region are equal. .So after scaling the (1) roughly we obtain $v_{in}B/c \sim J/\sigma$. From faraday's law we can find $J \sim cB/(4\pi\delta)$. We consider magnetic diffusivity $\eta \sim c^2/(4\pi\sigma)$. From conservation we get

$$\frac{\delta}{L} = \frac{v_{in}}{v_A} = S^{-1/2} \tag{2}$$

Here S is Lundquist number which is ratio of global ohmic diffusion time $\tau_{diff} = L^2/\eta$ to global alfvenic time $\tau_A = L/v_A$.

Most of the astrophysical system have large S. So the reconnection velocity (or rate) v_{in} will be small. Resistive length must also be thin because thats how current density can be large enough to dissipate incoming magnetic energy. But the resistive length is also the width of outflow which will result the mass flow small. This is how it constrains reconnection

velocity v_{in}. Other theories are also not able to explain reconnection thoroughly.

5.2. Fast MHD reconnection

Sweet Parker model of magnetic reconnection is slow because mass flow of plasma particles are channelize through thin resistive layer. [15] proposed that reconnection can be faster if there is an extra force provided to widen the resistive layer. That can be provided through shock waves. According to petschek model shock waves starts at the end of sweet parker layer.

From the mass conservation argument of sweet parker theory, if we replace the length of neutral line L from figure 7 with shorter length scale $L^{'}$. It increases the reaction rate by a factor of $\sqrt{L/L'}$. Petschek further derived the reconnection by substituting $L^{'}$, which reduces the length L to $L(8\ln S/\pi\sqrt{S})^2$. And it increases the reconnection speed to $v_A(\pi/8\ln S)$. Reconnection speed is around few percent of alfven speed, which is considerably fast for astrophysical events. This theory is widely accepted to understand fast reconnection mechanism.

To verify this theory, magnetic diffusivity η should be higher at X point, otherwise reconnection will not occur by just imposing this as an initial condition. It had been verified through MHD simulations. From qualitative perspective, if η is high then field lines will be reconnected faster. And during reconnection first η reaches maximum and rapidly decreases, it creates large reconnection and speed up the reconnection mechanism. In opposite to sweet parker model, in reconnection most of the energy converted to ion's kinetic energy and little energy go into electron's kinetic energy.

5.3. Collisionless Reconnection

Magnetic reconnection is explained through resistive MHD model, where electric field is defined in (1). Ohm's law is valid only for steady state in which lorentz force of electrons are balanced by frictional or drag force due to collisions. Thus v in 1 is understood to be electron's velocity. Current density of plasma flow is $J = n_e e(v_i - v_e)$ and assuming $v \sim v_i$, Ohm's law can be rewritten when $v_e \neq v_i$

$$\vec{E} + \frac{\vec{v} \times \vec{B}}{c} - \frac{\vec{J} \times \vec{B}}{en_e c} = \frac{\vec{J}}{\rho} \tag{3}$$

Third term on the left hand side of (3) represents Hall effect. When Hall term in (3) predominates, direction of electron's flow velocity coincides with current direction in reconnection plane. This model differs from Sweet-Parker and Petschek model, in which current is perpendicular to reconnection plane.

By taking out of plane ($\vec{y}$) component of (3) near X point. We can show that ion velocity $v_i \sim v$ is zero below ion skin depth scale. We can take ion skin depth as gyroradius of ion at alfven speed. Thus at $\delta < \delta_i$, Electric field $\vec{E}$ is predominated by Hall terms or resistive term in (3). Out of plane ($\vec{y}$) component of Hall term can be written as

$$\left(\frac{\vec{J} \times \vec{B}}{en_e c}\right)_y = \frac{\vec{B} \cdot \nabla \vec{B_y}}{4\pi en_e} \tag{4}$$

Equation (4) shows in plane current generates magnetic field B_y perpendicular to it. We can calculate the B_y from J_x and J_z by ampere's law at X point. Here J_x and J_z current densities of electron in flow and out flow and $J_x \propto x$, $J_y \propto -z$. From Ampere's law, $B_y \propto xz$, so this field will have quadrupole term. In MHD reconnection, electric field is resistive in reconnection region and inductive outside the reconnection region. Hall effect comes into picture when length scale is lesser than ion skin depth (δ_i), thus hall reconnection occurs when $\delta_{SP} < \delta_i$, through (2) we obtained

$$\frac{\delta_{SP}}{\delta_i} = \left(\frac{L}{\lambda_{mfp}}\right)^{1/2} \left(\frac{m_e}{m_i}\right)^{1/4} \tag{5}$$

where λ_{mfp} is mean free path of of electrons. We have assumed $v_A \sim v_{thi}$, $T_e = T_i$ and $\eta_\perp \sim 2\eta_\parallel$ applying to magnetic field ([40]). From (5) we can see that Hall effect dominates inn system when length of current sheet L is comparable to λ_{mfp}. In that case Hall effect causes collisionless reconnection.

5.4. Instabilities and time dependent effects

In any plasma system if relative speed electrons and ions (current) is larger than electron thermal speed, it creates two stream instability that leads to anomalous resistivity in the system. When thickness of reconnection region (X point) is lesser than ion skin depth, it increases reconnection rate as well as resistivity. This anomalous resistivity of plasma have other key effects which supports magnetic reconnection. It helps in keeping reconnection layer as thick as ion skin depth. Thinner layer of reconnection region will increase the resistivity in large amount and also increase magnetic diffusion which would retain the layer thickness to ion skin depth. Reconnection layer thickness in collisionless reconnection is thicker than sweet parker reconnection layer, that would allow reconnection faster. Thus the increased resistivity heats up the plasma where it balances the outside magnetic pressure. Other type of collision less plasma and hall effect do not heat the plasma. Increased resistivity also increase the rate of breaking field lines at X point.

Large scale instabilities and micro-instabilities have key importance in reconnection mechanism. It can

change the reconnection rate with time like it occurs in solar flares. These instabilities can create turbulence in the system which will lead to accelerate and heat up the particles. It is not discussed in detail in this review article.

[4] computed the model of turbulent MHD reconnection model. [10] investigated a model of collisionless reconnection [25]. Even though fluctuations in reconnection systems gives better insight of its evolution, but it still does not unveil the mystery of MHD reconnection time scales. This area of research is very interesting in scientific community.

6. Summary, Discussions and unsolved problems

Magnetic reconnection is topological self-rearrangement of magnetic field lines at X point. It is very important process in plasma physics. Magnetic reconnection occurs in astrophysical plasma as well as in laboratory plasmas. In astrophysics, it is studied to understand the dissipative process. In this review article we discussed the fundamentals of magnetic reconnection and recent advances and discoveries. How it converts magnetic energy in sawtooth oscillations and change its magnetic topology during magnetic self organization process.We discussed about observation of reconnection in space and laboratory. To observe solar corona there are several spacecrafts observing in different spectrum with various spectroscopic measurements. Different models of reconnection were discussed. Sweet Parker theory, Petschek theory of fast reconnection mechanism and collision-less reconnection.

Various issues in reconnection physics have not been figured out yet. Like, How magnetic energy get converted to kinetic energy of electrons and ions? How reconnection layer forms by global boundary of plasma? Why is reconnection fast in collisionless plasma? How do turbulence and fluctuation affect reconnection dynamics? In what channel energy flow take place? What is the cause of structure of reconnection layers?

References

[1] Kadomtsev B. *Sov. J. Plasma Phys.*, 1, 1975.

[2] Gary DE. Bastian TS, Benz AO. *Annu. Rev. Astron. Astrophys.*, 36, 1998.

[3] P. Baum and A. Bratenahl. *Phys. Fluid*, 17, 1974.

[4] Ambrosiano J Matthaeus WH Goldstein ML Plante D. *J. Geophys. Res.*, 93, 1988.

[5] Biskamp D. *Magnetic Reconnection in Plasmas*. Cambridge University Press, Cambridge, 2000.

[6] Krucker S. Dennis BR, Hudson HS. *Lect. Notes Phys.*, 725, 2007.

[7] Dungey. *Philos. Mag.*, 44, 1953.

[8] Parker E. *Cosmical Magnetic Fields*. Clarendon, Oxford, 1979.

[9] Priest E and T Forbes. *Magnetic Reconnection-MHD theory and Applications*. Cambridge University Press, 2000.

[10] E. M. E.M. de Gouveia Dal Pino and A. A. Lazarian. *A and A*, 441, 2005.

[11] Gabriel A H et al. Performance and early results from the golf instrument flown on the soho mission. *Sol. Phys.*, 175, 1997.

[12] Lin R P et al. Rhessi observations of particle acceleration and energy release in an intense solar gamma-ray line flare. *The Astrophysical Journal Letters*, 595, 2003.

[13] Forbes T G. *In reconnection of Magnetic fields: Magnetohydrodynamics and collisionless theory and observations*. Cambridge University Press, Cambridge, 2007.

[14] Frank A. G. *Izdatelstvo Nauka Moscow*, 1974.

[15] Petschek H. *Proceedings of the AAS-NASA Symposium on the Physics of Solar Flares*, 1964.

[16] Hudson HS. *Heliophysics II. Energy Conversion Processes ed. CJ Schrijver, GL Siscoe. In press*, 2009.

[17] Birn J. and E. R. Priest. *Reconnection of Magnetic Fields: Magnetohydrodynamics and Collisionless Theory and Observations*. Cambridge University Press, Cambridge, 2007.

[18] Dungey J. *Physics of the Magnetopause*. A G Monograph Vol 90, Washington D C, 1995.

[19] Wesson J. *Tokamaks*. Clarendon, Oxford, 1987.

[20] M. Kivelson and C. Russell. *Introduction to Space Physics*. Cambridge University Press, London, 1995.

[21] Golub L., J. Bookbinder, E. Deluca, M. Karovska, H. Warren, C. J. Schrijver, R. Shine, T. Tarbell, J. Wolfson, B. Handy, and C. Kankelborg. A new view of the solar corona from the transition region and coronal explorer (trace). *Phys. Plasmas.*, 6, 1999.

[22] Close R. M. C. E. Parnell D. W. Longcope and E. R. Priest. *Astrophys. J. Lett.*, 612, 2004.

[23] Yamada M. *Magnetic Helicity in Space and Laboratory Plasmas*. A G U Monograph, 1999.

[24] Yamada M. *Earth, Planets Space*, 53, 2001.

[25] Drake JF Swisdak M Che H Shay MA. *Nature*, 443, 2006.

[26] Yamada M. H. Ji S. Hsu T. Carter R. Kulsrud N. Bretz F. Jobes Y. Ono and F. Perkins. *Phys. Plasmas.*, 4, 1997a.

[27] Sweet P. *In Electromagnetic Phenomena in Cosmical Physics.* Lehnert Cambridge University Press, 1958.

[28] parker E. Sweet's mechanism for merging magnetic fields in conducting fluids. *Journ of Geophysical Research*, 62, 1957.

[29] Forbes TW. Priest ER. *Astron. Astrophys. Rev.*, 10, 2002.

[30] Kulsrud R. Magnetic reconnection in magnetohydrodynamic plasma. *Physics of Plasmas*, 1599(5), 1998.

[31] Stenzel R. and W. Gekelman. *Phys. Rev. Lett.*, 42, 1979.

[32] Mandzhavidze N. Ramaty R. *IAU Symp.*, 195, 2000.

[33] Murphy RJ. *Space Sci. Rev.*, 130, 2007.

[34] Masuda S, T Kasugi, H Hara, S Tsunets, and Y Ogawara. A loop-top hard x-ray source in a compact solar flare as evidence for magnetic reconnection. *Nature London*, 371, 1994.

[35] Tsuneta S. Interacting active regions in the solar corona. *The Astrophysical Journal Letters*, 456(1), 1996.

[36] S. I. A. G. Frank Syrovatskii and A. Z. Khodzhaev. *Sov. Phys. Tech. Phys.*, 18, 1973.

[37] Vasyliunas V. Theoretical models of magnetic field line merging. *Review of Geophysics and Space Physics*, 13, 1975.

[38] von Goeler S. W. Stodiek and N. Sauthoff. *Phys. Rev. Lett.*, 33, 1974.

[39] Hughes W. *Introduction to space physics.* Cambridge university Press, London, 1995.

[40] M. Y. Ren H. Ji J. Breslau S. Gerhardt R. Kulsrud Yamada and A. Kuritsyn. *Phys. Plasmas*, 13, 2006.

[41] Masaaki Yamada, Russell Kulsrud, and Hantao Ji. Magnetic reconnection. *Rev. Mod. Phys.*, 82, 2010.

Fast and Heavy – Review of Target Normal Sheath Acceleration

Anton received his Diploma degree (equivalent to MSc) in Physics by the Technische Universität Dresden in the year 2014. His thesis topic was about laser-plasma interaction, especially the influence of spatial-temporal changes in laser pulses on particle acceleration.

His strong interest in physics started in high school, which was acknowledged with a special award Anerkennungspreis für Besondere Lernleistung. Alongside his studies at the university he was working at the Helmholtz-Zentrum Dresden-Rossendorf on the theoretical modeling of laser particle acceleration.

Anton Helm

Instituto Superior Técnico
Instituto de Plasmas e Fusão Nuclear
Av. Rovisco Pais, N. 1, 1049-001 Lisboa

E-mail: `ahelm@ipfn.tecnico.ulisboa.pt`

September 2015

Abstract. Ion acceleration driven by intense laser pulses is attracting more attention over the past few years. The extremely promising properties such as small source size and outstanding beam characteristics, such as ultrashort duration, high brilliance and low emittance, are responsible for high interest as new acceleration sources. In addition to it, more and more facilities with high quality and high energy lasers are in development which will push the generation of laser driven ions to new frontiers. Nowadays, multi-MeV proton and ion beams in a wide range of experiments have been demonstrated. An overview is given of the state of the art of target normal sheath acceleration.

1. Introduction

Around 30 years ago, the community of beam accelerators believed in a steady growth of the beam energy by conventional accelerators which was driven by continuous innovations in acceleration techniques [1]. During the years of construction of facilities like Superconducting Super Collider (SSC) it was seen that growth in energy comes with an extensive amount of investment. Therefore the energy frontier did not proceeded to grow on the same rate as predicted and even reached almost a saturation level. Nowadays facilities like Large Hadron Collider (LHC) are built by a large portion of investments (several billions Euros) to provide beam energies of 6.5 TeV [2] in a 27 km long tunnel. For this particular reason novel techniques have to be explored, such as laser driven ion acceleration, to provide high energy and compact sources.
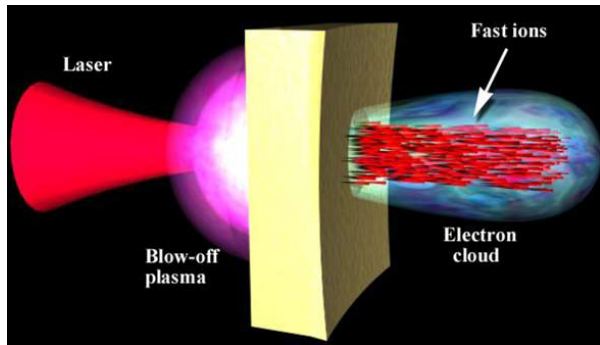

Figure 1. Schematic sketch of laser driven ion acceleration. The laser hits the front surface of the target which leads to an expansion of the electrons at the rear side and the acceleration of ions. The generated cloud of charged particles expands as a quasi-neutral cloud.

The first steps towards laser driven ion acceleration were already inspected by introducing the concept of "coherent acceleration" of quasineutral groups by [3]. The differences to traditional techniques were the proportionality between the accelerating field and the particles which are getting accelerated. It also included additional elements, such as automatic synchronization between the accelerating field and the particles, the localization in a small region, where the particles are, and the quasineutral groups of large number of energetic particles. These features are the key elements of ion acceleration driven by intense laser pulses. The ions are accelerated due to high accelerating fields generated by laser induced collective displacement of electrons. The accelerating field vanishes when a charge neutrality is restored. Therefore the electrons and the ions are moving in a ballistic way together. In Figure 1, an artistic sketch of the acceleration mechanism is shown.

In the year 2000 several experimental campaigns [4, 5, 6] reported observation of an intense emission of multi-MeV protons from solid targets of several microns thickness irradiated by high-intensity laser pulses. The protons were measured coming from the rear side of the target – opposite side to the irradiated surface – and it was a collimated beam along the target normal direction. It was not a big surprise to measure protons in metallic targets, which do not include hydrogen as a chemical compound, as it was indicated by previous observations. In previous experiments it was shown that protons from impurities, i.e., thin layers of water or hydrocarbons which are ordinarily present on solid surfaces under standard experimental conditions, are likely to be accelerated first due to their low charge-to-mass-ratio [7, 8, 9, 10]. For this particular reason the measurements with metallic targets are showing a significant acceleration of protons.

The detection of such energetic protons raised an enormous interest in fundamental research and in an broad field of applications. A promising application is the usage of a peculiar feature of multi-MeV ions, the profile of energy deposition in dense matter. Compared to electrons or X-ray, protons and light ions deliver most of their energy at a energy specific latter point, the so-called Bragg peak [11, 12]. The reasoning for such behavior lies in the increased cross-section for lower energies. With such properties, protons and light ions are perfect candidates for beam therapy [13, 14, 15], the basis for warm dense matter [16, 17] and fast ignition of inertial confinement fusion targets [18].

While the strength of applicability was known, the physics of the acceleration mechanism was opened and still on debate, such as the region from which the protons have been accelerated and also the driving mechanism of the acceleration. Several sources [4, 5] suggested that the accelerated protons are coming from the front of the target. Another observation [6] provided evidence that protons are coming from the rear side [19]. This was supported by the introduced target normal sheath acceleration (TNSA) model by [20]. TNSA is driven by the space-charge field generated at the rear surface of the target by high relativistic electrons which have been accelerated at the front surface of the target, crossed the target bulk and escaped into the vacuum from the rear side.

The major aim of the research towards laser driven ion acceleration is to increase the energy up to several hundreds of MeV and beyond. With increasing laser intensities the ion energy scaling estimated for TNSA might breakdown and other mechanism will overcome. An analysis by [22, 23] indicated a $\left(I\lambda^2\right)^{1/2}$ scaling of the proton energy, where I is the laser intensity and
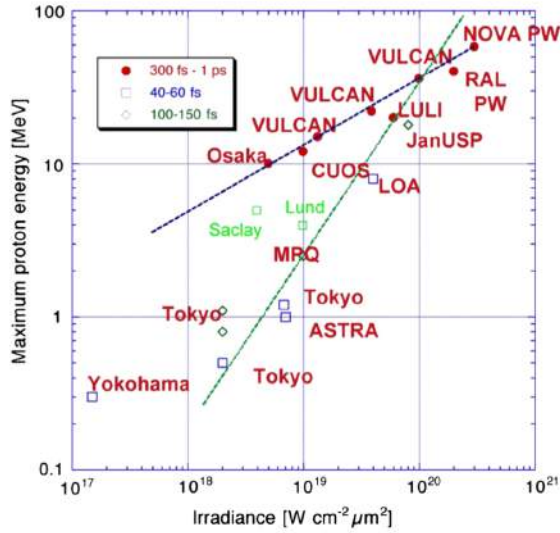
Figure 2. Highest proton energy obtained from laser driven acceleration as a function of the laser irradiance and for different pulse durations from experiments reported until 2008. Two lines are included, the blue dashed line represents a scaling of $I^{1/2}$ and the green dashed line represents a scaling proportional to I. Taken from [21].
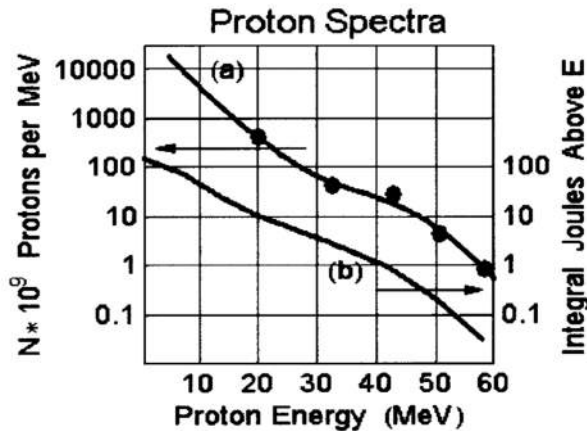

Figure 3. Proton spectrum from the rear side of a $100\,\mu\mathrm{m}$ solid target irradiated by an intense laser at normal incidence. The integrated energy of the protons indicates the conversation efficiency. Taken from [6].

λ is the laser wavelength. Figure 2 gives a overview of recent obtained maximum proton energies. It also includes results based on Ti:Sa laser systems. Typical Ti:Sa setups deliver short pulses in the range of a few tens of fs. Such laser systems indicate a $I\lambda^2$ scaling. As one can see it is crucial to establish the most relevant scaling parameters besides the improvement of beam parameters, such as beam emittance, brilliance and the particle number of mono-energetic ions. Ions and protons which are accelerated in the TNSA regime are highly laminar and have very low emittance, but

their energy spectrum is ordinarily broad (exponential distributed) and not bunched, as seen in Figure 3.

These problems lead to a search of novel mechanisms, by adapting of known mechanism which has been developed under a different context, such as radiation pressure acceleration (RPA) [24, 25, 26] and collisionless shock acceleration (CSA) [27, 28]. Other methods are based on advance target engineering and nonlinear relativistic optical effects by abusing transparency, such as break-out afterburner (BOA) [29, 30, 31]. Compared to TNSA, these mechanism are still under development, and require a deeper physical and experimental investigation.

In this paper we focus on giving a review on TNSA. In section 2, the basic principles behind TNSA will be presented. The presented principles can be easily extended towards a general theory of laser driven ion acceleration. At the end of the section we will highlight the most significant optimization and modeling efforts done in this area.

2. Principles of Target Normal Sheath Acceleration

Laser ion acceleration is generally performed with solid targets, mostly referred as overdense targets, where the electron density n_e is greater than the critical density n_c

$$n_c > n_e = \frac{m_e \omega^2}{4\pi e^2} = 1.1 \times 10^{21}\,\mathrm{cm}^{-3} \left(\frac{\lambda}{1\,\mu\mathrm{m}}\right)^{-2}. \quad (1)$$

The condition $n_e = n_c$ is equivalent to the condition of the laser frequency $\omega = 2\pi c/\lambda$ being the same as the plasma frequency $\omega_p = \left(4\pi n_e e^2/m_e\right)^{1/2}$. As the linear refractive index of a plasma is given by $\mathrm{n} = \left(1 - \omega_p^2/\omega^2\right)^{1/2} = (1 - n_e/n_c)^{1/2}$. For an overdense plasma the refractive index has imaginary values and the incoming laser pulse can not propagate through the target area. Therefore the interaction of the laser with the plasma occurs either in the "underdense" area where $n_e < n_c$ or near the "critical" surface where $n_e \simeq n_c$. The underdense area in front of the target is usually referred as the "preplasma" of the target which occurs by the interaction of an intense laser pulse reaching the target before the main pulse.

To extend the refractive index to a full description, one has to take relativistic effects into account. A qualitative description of the refractive index is to replace the electron mass by $m_e\gamma$ where the relativistic gamma is given by

$$\gamma = \sqrt{1 + \langle \mathbf{a}^2 \rangle} = \sqrt{1 + \frac{a_0^2}{2}}, \quad (2)$$

with $\mathbf{a} = e\mathbf{A}/m_e c^2$, the vector potential of a propagating plane wave $\mathbf{A} = \mathbf{A}\left(\mathbf{r}, t\right)$ and the angular

brackets to represent an average over the oscillation period [32]. The parameter a_0 is usually refered as the dimensionless amplitude which relates to the laser intensity [32] by

$$a_0 = 0.85 \left(\frac{I\lambda[\mu m]^2}{10^{18}\,\mathrm{W\,cm^{-2}}} \right)^{1/2} . \tag{3}$$

In above expression the intensity $I = c\langle E^2 \rangle / 4\pi$ and the electric field $\mathbf{E} = -(1/c)\,\partial\mathbf{A}/\partial t$ has been used.

The nonlinear behavior of the relativistic refractive index $n_{\mathrm{nonlinear}} = (1 - n_e/\gamma n_c)^{1/2}$ reduces the criteria of the refractive index to become imaginary for $n_e > \gamma n_c$. This extension of the refractive index increases the cutoff density for a plane monochromatic wave which is known as relativistic self-induced transparency. However, the problem of laser penetration inside a plasma is not trivial [33, 34, 35], due to the nonlinearity in the wave equation and the self-consistent modification of the plasma density, given by the ponderomotive force. For an oscillating, quasimonochromatic electromagnetic field described by a dimensionless vector potential $\mathbf{a}(\mathbf{r}, t)$ whose envelope is sufficiently smooth, the relativistic ponderomotive force, see [36, 32], is

$$\mathbf{f}_p = -m_e c^2 \nabla \left(1 + \langle \mathbf{a} \rangle^2 \right)^{1/2} . \tag{4}$$

The smoothness of the envelope has to fulfill the condition $|\delta| \ll \lambda$ where δ describes the displacement of the oscillating center of a particle. The ponderomotive force of an incoming quasi-plane wave results in the pushing of the electrons towards the incident direction, due to the lower mass.

Since the laser pulse cannot penetrate the bulk area of the target, a mechanism is needed to describe the energy absorption of the laser. The energy of the laser pulse will be absorbed by the so-called hot electrons. Hot electrons have a typical kinetic energy which is given by

$$E_p = m_e c^2 \left(\sqrt{1 + a_0^2/2} - 1 \right) \tag{5}$$

and it is commonly refered as ponderomotive energy [37], as it describes the cycle-averaged oscillation energy in the electric field of a laser in vacuum. The acceleration of the most energetic protons and ions is driven by the fast and hot electrons. The process of hot electron generation is quite complex and not fully understood yet, for further reading please see [38, 32]. It is worth mentioning that the condition under which the laser penetrates the plasma are crucial. Laser parameters are playing an important role for the absorption of the energy, parameters like polarization and incidence angle can not only change the amount of energy absorption, but also change the heating mechanism. Plasma parameters can affect the heating
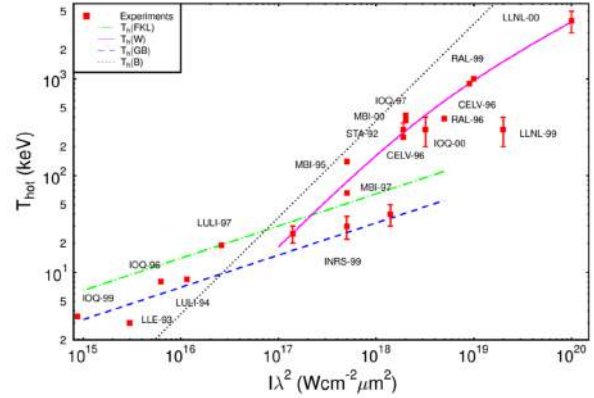

Figure 4. The temperature of hot electrons as a function of irradiance from different observation using a sub-ps laser system for laser-solid interaction. For further information about experimental paramers, diagnostics and references, see Table 5.2 in [38]. The lines represent scalings for the temperature obtained by different methods (FKL – Forslund, Kindel and Lee: [42], W – Wilks: [37], GB – Gibbon and Bell: [43], B – Brunel: [41]). Taken from [38].

as well. In addition, preplasma formation can lead to higher electron heating where electrons having even higher energies as given by (5), see [39]. The generation of the preplasma is not fully controllable and may fluctuate from shot to shot. A preplasma can be generated by a intense laser pulse, so-called prepulse, which ionize the target before the main pulse reaches it. With recent developed techniques, such as plasma mirrors [40], fluctuations can be reduced by delivering almost prepulse free pulses.

A popular electrostatic model of electron heating at step-boundary was proposed by [41]. In his model the electrons are taken out of a perfect conductor by an oscillating capacitor field. Electrons which absorb the energy are the ones who are half of cycle in vacuum and are pushed back again inside. They are the source of energy transfer which is in order of the oscillation energy in the external field. The difficulty lies in the perfect adoption of a heating model, such that simple model are usually not self-consistent. In this scenario, the capacitor field is assumed to vanish inside the target, implying a surface charge density.

The high dependency of hot electron generation on laser and plasma parameters is responsible for the scattering of data points and slightly difference of experimental data. In addition, the evolution of the prepulse effects can be only estimated which highlights further the complexity of the full understanding. Therefore the absorption values and characteristics of the hot electron distribution are taken from phenomenological assumption or by estimation from particle-in-cell (PIC) simulations. It is commonly accepted to assume the hot electron distribution to

be Maxwellian where the temperature T_h is given by (5). Figure 4 shows a collection of different electron temperatures from different measurements obtained by sub-ps pulses up to the year 2000. It indicates a nice fit to the scaling as $\left(I\lambda^2\right)^{1/2}$ of T_h which fulfills the assumption to characterize the temperature by (5) for high laser intensities. In addition one has to estimate the amount of total fractional absorption of hot electrons η_h which is usually estimated empirically to be in the range from $10\,\%$ to $30\,\%$ [44] with experimental indication that it might be higher at ultrarelativistic intensities [45]. To estimate the initial density of hot electrons n_h, an energy flux balance condition $\eta_h I = n_h v_h T_h$ with $v_h \simeq c$ can be applicable. In most scenarios it will be lower as n_c which fulfills the argument that the density cannot be higher as the density of the region of hot electron generation.

Inside the target area the can differ from the estimated n_h, due to angular divergence of the electron flow or electron refluxing effects, just to mention a few examples [46]. It is still possible to estimate the total number of hot electrons N_h by an energy balance relation $N_h \sim \eta_h U_L/T_h$ with the energy of the laser pulse U_L. Such rough estimation might change depending on the sheath field modeling which is taken into account [47].

The transport of hot electrons in solids has been extensively investigated due it high relevance into electron-driven fast ignition in inertial confinement fusion (see [48] for a survey). Key elements of investigation are regimes of high currents and self-generated fields. The generated high currents by the hot electrons will be neutralized locally by cold electrons contributing to the return current. Otherwise the generated fields, either by charge unbalance or by free flowing current would be strong enough to stop the hot electrons [49, 50]. In general the hot electrons will be separated as ω or 2ω bunches depending on incidence angle on polarization. Such separation and non-thermal condition can lead to deflection of high energetic protons or ions [51, 52].

A very intense current of high-energy hot electrons which has been generated at the front side of the target will reach the rear side and escape into vacuum. The charge unbalance generates a sheath field E_s to backhold the escaped electrons. The field strength required for the backholding can be empirically estimated with

$$eE_s \sim \frac{T_h}{L_s}, \tag{6}$$

where L_s is the spatial elongation of the sheath which can by estimated with the Debye length of the hot electrons $L_s \simeq \lambda_{\mathrm{D,h}} = \left(T_h/4\pi e^2 n_h\right)^{1/2}$. With typical setups, a sheath field in the order of $E_s \simeq 10^{11}\,\mathrm{V\,cm^{-1}}$ can be achieved which is sufficient enough to backhold
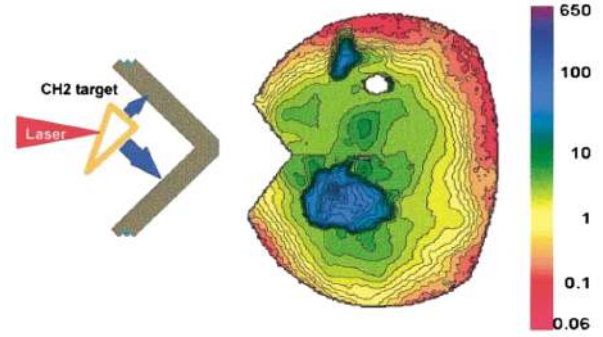

Figure 5. Proton emission from a laser irradiated wedge target which has effectively two rear surfaces. As seen, two separate spots are observed on the detector, showing that most of the high energetic protons are originate from the rear side. Taken from [6].

most of the escaping electrons. In addition to it, ionized atoms at the rear surface will be accelerated as well. If ions cross the sheath area then they will gain an energy $E \simeq ZeE_sL_s = ZT_h$ which will result in MeV energies and have a scaling of $I^{1/2}$ if $T_h \simeq E_p$ given by Eq. (5). Protons from thin layer impurities at the surface will be accelerated mainly, as they are located directly at boundaries, and therefore located at highest fields. Furthermore, protons have a higher charge-to-mass ratio as ions, such for example C^{4+}. This will result in a screening of the sheath field, due to reduced charge unbalance. It is a qualitative scenario for TNSA, which was introduced by [20], to describe the experimental observation of [19, 6].

The acceleration mechanism of TNSA relies on acceleration normal to the target surface with the highest field at the target boundaries. The field has the highest impact on protons, which can be present due to surface contaminants or as the constituents of the solid target, for example in plastic targets. On longer time scale, due to lower charge-to-mass ratio, part of the heavier ions will be accelerated as well, if the present protons cannot balance out the charge separation of the escaped electrons. The amount of present protons, coming from impurities of the target surface, can be removed before the interaction, for example, by preheating the target [53]. With such methods, ions of several different species may be favored for the acceleration process [54].

Most of the acceleration, in the TNSA regime, happens at the rear side as supported by several observations. As [6] already presented, that the emission was normal to the rear surface which was observed by using wedge targets with clearly two rear sides. Two different proton beams have been observed which have been orientated normal to the two rear surfaces, as seen in Figure 5. Further evidence of ions being accelerated at the rear side was given by

observation of a structured target at the rear side to produce a modulation of the proton beams [55].

Several models have been proposed which are based on general studies of plasma expansion and related ion acceleration, developed before [56, 57, 58, 59] and after [60, 61, 62, 63, 64, 65] initial TNSA experiments. All of them are considered as suitable simplifications, based on static assumptions, only light ions are accelerated initially and heavier over a long time, or on a dynamic approach, taking the sheath evolution into account. Most of these models assume a 1D geometry motivated on normal orientated fields which requires a sufficiently flat and a spatially uniform electron cloud. In addition to it, most of the models are phenomenological, i.e., they need input parameters which are not precisely known, and they don't allow a full description of the TNSA mechanism.

3. Conclusion and Outlook

Since the first observation of [6, 5, 4] a lot of research on ion acceleration driven by superintense laser pulses, which was reviewed in this paper, has been performed. Most of the research has been focused around the target normal sheath acceleration mechanism. In the next years, with the availability of higher intense lasers, new schemes, such as radiation pressure acceleration, shock acceleration or break-out afterburner, might get dominated and shift the focus of research. Fundamental theoretical ideas have been presented, together with promising experimental results. It is still an open debate which mechanism will supplement TNSA in the future.

With the developments and achievements in laser technology the area is not fully exploit. Questions about possible observations in the case of high laser intensity regimes, close to or even beyond the limit were ions are relativistic, are debatable or difficult to predict. In addition, it opens the possibility to provide further information about the scaling of ion acceleration or opens the availability to test theoretical ideas of fundamental physics in the quantum electrodynamics regime.

The first period of this research lead to a series of open questions. Can the threshold of the GeV/nucleon be overcome? Will the research lead to active and satisfactory control on the physics of laser ions acceleration by focusing on laser pulse control and optimizing target properties? Would it be possible to build up practical application on laser driven ion acceleration? Such question and other upcoming might find an answer in the future.

References

[1] Yordy 2010 Current and Future Developments in Accelerator Facilities URL http://www.hep.ucl.ac.uk/iop2010/talks/14.pdf
[2] O'Luanaigh C Proton beams are back in the LHC URL http://home.web.cern.ch/about/updates/2015/04/proton-beams-are-back-lhc
[3] Veksler 1957 *The Soviet Journal of Atomic Energy* **2** 525–528
[4] Clark and et al 2000 *Phys. Rev. Lett.* **84** 670–673
[5] Maksimchuk and et al 2000 *Phys. Rev. Lett.* **84** 4108–4111
[6] Snavely and et al 2000 *Physical Review Letters* **85** 2945–2948
[7] Gitomer and et al 1986 *Phys. Fluids* **29** 2679–2688
[8] Fews and et al 1994 *Physical Review Letters* **73** 1801–1804
[9] Beg and et al 1997 *Physics of Plasmas* **4** 447–457
[10] Clark and et al 2000 *Physical Review Letters* **85** 1654–1657
[11] Knoll 2010 Wiley: Radiation Detection and Measurement, Fourth Edition
[12] Ziegler, Biersack and Ziegler 2012 *SRIM: the stopping and range of ions in matter*
[13] Cobble and et al 2002 *Journal of Applied Physics* **92** 1775–1779
[14] Roth and et al 2002 *Phys. Rev. ST Accel. Beams* **5** 61301
[15] Borghesi and et al 2004 *Phys. Rev. Lett.* **92** 55003
[16] Patel and et al 2003 *Phys. Rev. Lett.* **91** 125004
[17] Snavely and et al 2007 *Physics of Plasmas* **14** 092703
[18] Roth and et al 2001 *Phys. Rev. Lett.* **86** 436–439
[19] Hatchett and et al 2000 *Physics of Plasmas* **7** 2076
[20] Wilks and et al 2001 *Phys. Plasmas* **8** 542
[21] Borghesi and et al 2008 *Plasma Physics and Controlled Fusion* **50** 124040
[22] Borghesi and et al 2006 *Fusion Science and Technology* **49** 412–439
[23] Fuchs and et al 2006 *Nat Phys* **2** 48–54
[24] Sentoku and et al 2003 *Physics of Plasmas* **10** 2009–2015
[25] Schlegel and et al 2009 *Physics of Plasmas* **16**
[26] Henig and et al 2009 *Phys. Rev. Lett.* **103**(24) 245003
[27] Denavit 1992 *Phys. Rev. Lett.* **69**(21) 3052–3055
[28] Silva and et al 2004 *Phys. Rev. Lett.* **92**(1) 015002
[29] Henig and et al 2009 *Phys. Rev. Lett.* **103**(4) 045002
[30] Albright and et al 2010 *Journal of Physics: Conference Series* **244** 042022
[31] Yan and et al 2010 *Applied Physics B* **98** 711–721
[32] Mulser and Bauer 2010 *High power laser-matter interaction*
[33] Cattani and et al 2000 *Physical Review E* **62** 1234–1237
[34] Goloviznin and Schep 2000 *Physics of Plasmas* **7** 1564–1571
[35] Shen and Xu 2001 *Physical Review E* **64** 056406
[36] Bauer, Mulser and Steeb 1995 *Phys. Rev. Lett.* **75** 4622
[37] Wilks and et al 1992 *Phys. Rev. Lett.* **69** 1383–1386
[38] Gibbon 2005 *Short pulse laser interactions with matter: an introduction*
[39] Esarey, Schroeder and Leemans 2009 *Reviews of Modern Physics* **81** 1229–1285
[40] Dromey and et al 2004 *Review of Scientific Instruments* **75** 645–649
[41] Brunel 1987 *Physical Review Letters* **59** 52–55
[42] Forslund, Kindel and Lee 1977 *Phys. Rev. Lett.* **39** 284–288
[43] Gibbon and Bell 1992 *Phys. Rev. Lett.* **68** 1535
[44] Theobald and et al 2006 *Physics of Plasmas* **13** –
[45] Ping and et al 2008 *Physical Review Letters* **100** 085004
[46] Mackinnon and et al 2002 *Phys. Rev. Lett.*
[47] Ridgers and et al 2011 *Physical Review E* **83** 036404
[48] Freeman and et al 2006 *Fusion Science and Technology* **49** 297–315
[49] Davies and et al 1997 *Physical Review E* **56** 7193–7203
[50] Passoni and et al 2004 *Physical Review E* **69** 1–11
[51] Zeil and et al 2012 *Nature Communications* **3** 874
[52] Helm 2014 *Influence of Spatial-Temporal Structure of Laser*

Pulses on Laser-Plasma Interaction (Diploma Thesis)

[53] Hegelich and et al 2002 *Physical Review Letters* **89** 085002

[54] Hegelich and et al 2005 *Physics of Plasmas* **12** 056314

[55] Cowan and et al 2004 *Physical Review Letters* **92** 204801

[56] Pearlman and Morse 1978 *Physical Review Letters* **40** 1652–1655

[57] Wickens, Allen and Rumsby 1978 *Physical Review Letters* **41** 243–246

[58] True, Albritton and Williams 1981 *Physics of Fluids* **24** 1885

[59] Kishimoto 1983 *Physics of Fluids* **26** 2308

[60] Kovalev and Bychenkov 2003 *Physical Review Letters* **90** 185004

[61] Mora 2003 *Physical Review Letters* **90** 185002

[62] Mora 2005 *Phys. Rev. E* **72** 56401

[63] Betti and et al 2005 *Plasma Physics and Controlled Fusion* **47** 521

[64] Ceccherini and et al 2006 *Laser Physics* **16** 594–599

[65] Peano and et al 2007 *Physical Review E* **75** 066403

Tailoring plasma composition and profile towards higher energy quality wakefield accelerators

Giannandrea studied at the University of Pisa, Italy, where he obtained an MSc degree in Plasma Physics in collaboration with the University "La Sapienza" of Rome.

During his master career, he became interested in inertial confinement fusion and participated in a summer school in Ohio, USA to improve his knowledge of fusion research. He focused his master thesis on the propagation of shock fronts throughout ICF targets, analyzing different transport models both theoretically and numerically.

He worked with the hydrodynamic code DUED and he presented his results in several posters and talks.

Giannandrea Inchingolo

Instituto de Plasmas e Fusão Nuclear (IPFN), Instituto Superior Técnico,
Avenida Rovisco Pais, 1049-001 Lisboa, Portugal

E-mail: `giannandrea.inchingolo@tecnico.ulisboa.pt`

Abstract. The use of Laser wakefield accelerators for medical and industrial application requires that the quality of the beam generated is very high. In this work we focus on the maximizing energy of the beam. To do this, we analyze a combination of ionization injection and tailored plasma density profile techniques. In particular, we use ionization injection of He:N gases mixture to generate the electron beam and then we use a step density profile of He to increase the energy quality of the beam. In this way, we will show that the maximum energy of the beam generated is increased by 68% compares with the case of just ionization injection and, also, the relative energy spread of the beam is reduced by 25%.

1. Introduction

Acceleration of electrons using laser driven plasma wakes is an active area of research. By sending a laser pulse into an underdense plasma, it is possible to create a longitudinal wake structure guided by the ponderomotive force of the pulse [1]. Electrons can be trapped in this wake structure and then accelerated by the longitudinal electric field to energies up to 1 GeV in few centimeters [2] [3]. Using standard accelerating techniques, the accelerating gradient achieved are on the order of 5 MeVm^{-1} [4]. The advantage of laser wakefield acceleration (LWFA) technique is to obtain higher acceleration fields reducing the size of the accelerators.

Consequently, LWFA technique represents the new frontier in accelerating system and then the use of this technique is investigated for several applications, for example cancer therapy, imaging or Lithography [5].

These kind of applications require very high quality of the electron beams generated, in order to control, for example, the position and the energy of the beam. Recently, several numerical and experimental works were made to improve the quality of the beam, reducing, for example, the divergence of the beam, increaseing the total charge [6] or the stability [7].

In this study, we investigated a combination of two techniques, ionization injection [8] and tailored plasma density [9], to increment the energy and reduce the relative energy spread of the beam.

To do this, we use the fully relativistic particle-in-cell (PIC) code OSIRIS [10] to analyze 1D simulations of the longitudinal direction of the propagation of the laser into the plasma.

In our work, we can distinguish two steps: first, we analyze the generation of the electron beam obtained through the ionization injection technique and then we improve the quality of the beam through tailored plasma profile.

2. Simulation setup

Before presenting the analysis of the results obtained, it is important to discuss first the set of parameters used in all the simulations. All the quantities are normalized to the standard PIC code normalization, i.e., the lenghts are normalized to the skin depth (c/ω_p) and the frequencies to the plasma one (ω_p). In this units, the laser has intensity of $a_0 = 3.0$, length of 5.0 c/ω_p and pulse duration of $\Delta t_p = 10.0 \ \omega_p^{-1}$. The frequency of the laser is $\omega_0 = 15.0 \ \omega_p$. In this configuration set up, the plasma is considered underdense ($\omega_0 \gg \omega_p$), as we want for the propagation of the laser throgh it.
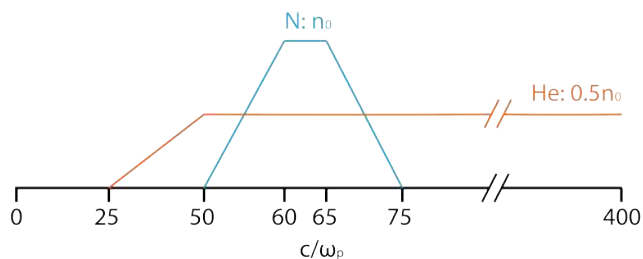

Figure 1: Shape of the density profile for Nitrogen (blue) and Helium (orange). The Nitrogen density has a peak value of n_0 instead the Helium density has a peak value of 0.5 n_0. The Nitrogen gas is mixed with the Helium after 50 skin depth, in order to permit to the laser to create the wake into the Helium plasma.

3. Preliminary results: ionization Injection

To inject electrons into the wakefield, we use a gas mixture of Helium and Nitrogen at 3 %, where the density profile of the plasma is the one shown in figure 1. The beams generated this way starts to propagate into a uniform plasma profile of density $n_{low} = 0.5 \ n_0$ where $n_0 = 5.0 \times 10^{18} \ cm^{-3}$ is the normalization density.

In this condition, the beam is afflicted by two different issues, as shown in figure 2: first, the beam is trapped in a region of non-uniform electric field. This way, different regions of the beam feel different accelerating gradients and then the energy spread increments (figure 2a).

On the other hand, as we know by the theory [9], the beam velocity is approximately the speed of light $v_e \sim c$, instead the phase velocity of the electric wake is less than c $v_\phi < c$.

As a consequence, during the evolution of the acceleration, the beam moves away from the maximum acceleration point of the wake (figure 2b) and this reduces the maximum energy reached by the beam.

4. Beam quality control: tailored profile

To solve both of the two issues described in section 3, we use the property of a plasma up ramp [9]. When the laser crosses a region of a plasma density gradient, the phase velocity of the wake is modified by a term proportional to ∇n.

When this term is dominant, we can use an up ramp of the plasma density profile to increase the phase velocity of the wake and then match the maximum acceleration point of the wake with the electron beam.

We apply this concept on a series of up ramps alternating with flat density profiles, as shown in figure 3, to balance the effects of increase and decrease of the wake phase velocity.

The choise of a stairs configuration is preferible to the one of a constant increase of the density, because
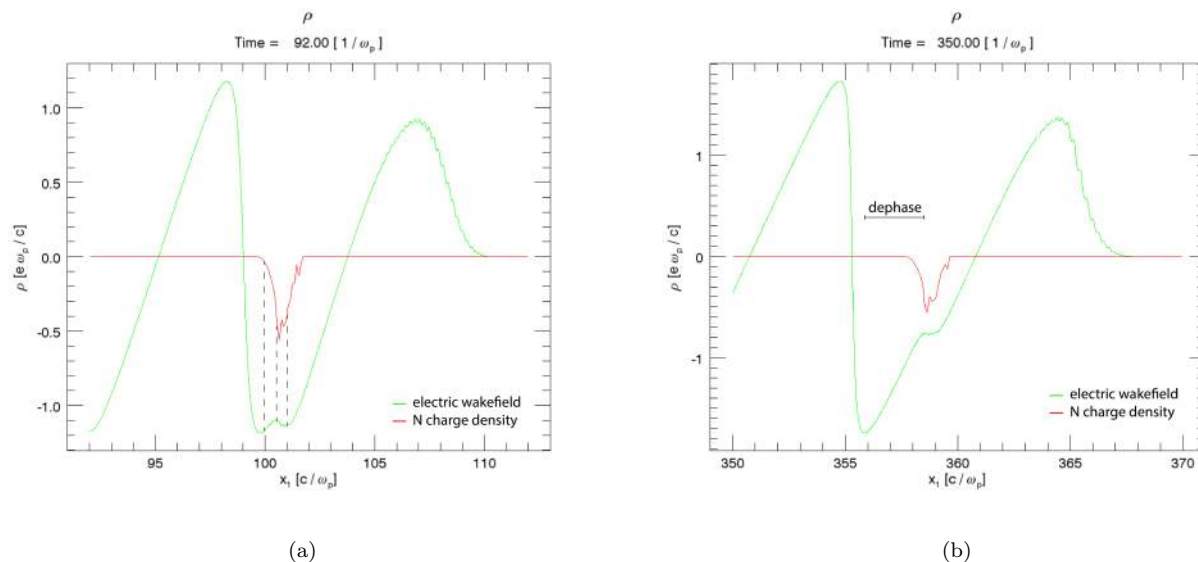
(a)

(b)

Figure 2: (a) At 92 plasma time, the electron beam is phased with a non-uniform accelerating field. This means that different regions of the beam feels a different accelerating field and that increases the energy spread of the beam. (b) At 350 plasma time, the beam is dephased with the maximum acceleration point of the wake and it feels the effect of a flat field. This means that the beam is uniformly accelerated (no increase of energy spread) but it is not accelerated at the region of the maximum field, reducing this way the maximum energy achieved by the beam.

we noticed that the decrease of phace velocity is not constant during the process. Conseguently, it is better to use a stairs profile, that permits to balance with the right increase of phace velocity due to the correct choise of up ramp strenght.
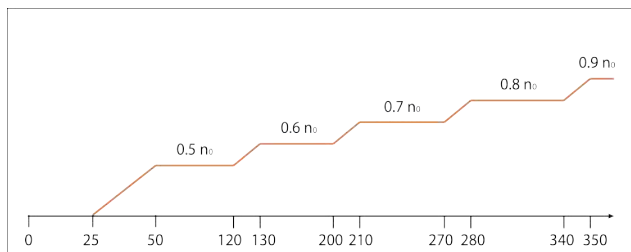

Figure 3: Tailored density profile for Helium plasma. The first 120 skin depths are the same of the simulation performed without the up ramps. Then, the density profile is increased with a stairs profile that alternates up ramps and flat profile, using the changing of the wake and the phase velocity to phase-lock the beam with the maximum acceleration point of the wake.

5. Results

We show now the effects of the tailored plasma profile on the energy quality of the beam in the configuration described in section 4. We compare the beam obtained with a flat density profile of Helium at 0.5 n_0 with the beam obtained with a step profile from 0.5 n_0 up to 0.9 n_0.

Analyzing the phase space shown in figure 4, the phase-lock of the beam with the maximum acceleration point permits to increase the maximum momentum of the beam from 340 $m_e c$ to 570 $m_e c$, that corresponds to

increase the maximum energy from 170 MeV to 285 MeV.

Figure 4 shows another important result: the shape of the beam in the phase space shows larger energy spread in the case with the tailored profile compared to the other case. Analyzing the evolution of the process,for example at 300 ω_p^{-1}, it is possible to understand the origin of this effect.

Figure 4c shows that the beam is phase-locked with the maximum acceleration point, as we want, but in this situation the backward tail of the beam feels very large decelerating field and so it is not uniformly accelerated with the rest of the beam, generating the very sharp vertical line in the phase space.

Figure 4d shows the case without tailored profile. In this situation, the beam is phased with a region of flat accelerating field. This means that the beam is uniformly accelerated and then the shape of the beam in the phase space is generated at the beginning of the process, when it feels different accelerating gradients, as described in figure 2a.

The spectrum in figure **??** also shows two important results. Using the tailored plasma profile to phase-lock the beam and the wake, a fraction of electrons injected into the beam is lost, precisely from 0.9 to 0.65 arbitrary units, that corresponds to a reduction of $\sim 28\%$ of the total charge of the beam. On the other hand, using the tailored profile, the total energy spread of the beam increases from 20 MeV to 25 MeV, but considering the increase of the maximum energy, the relative energy spread of the beam reduces from
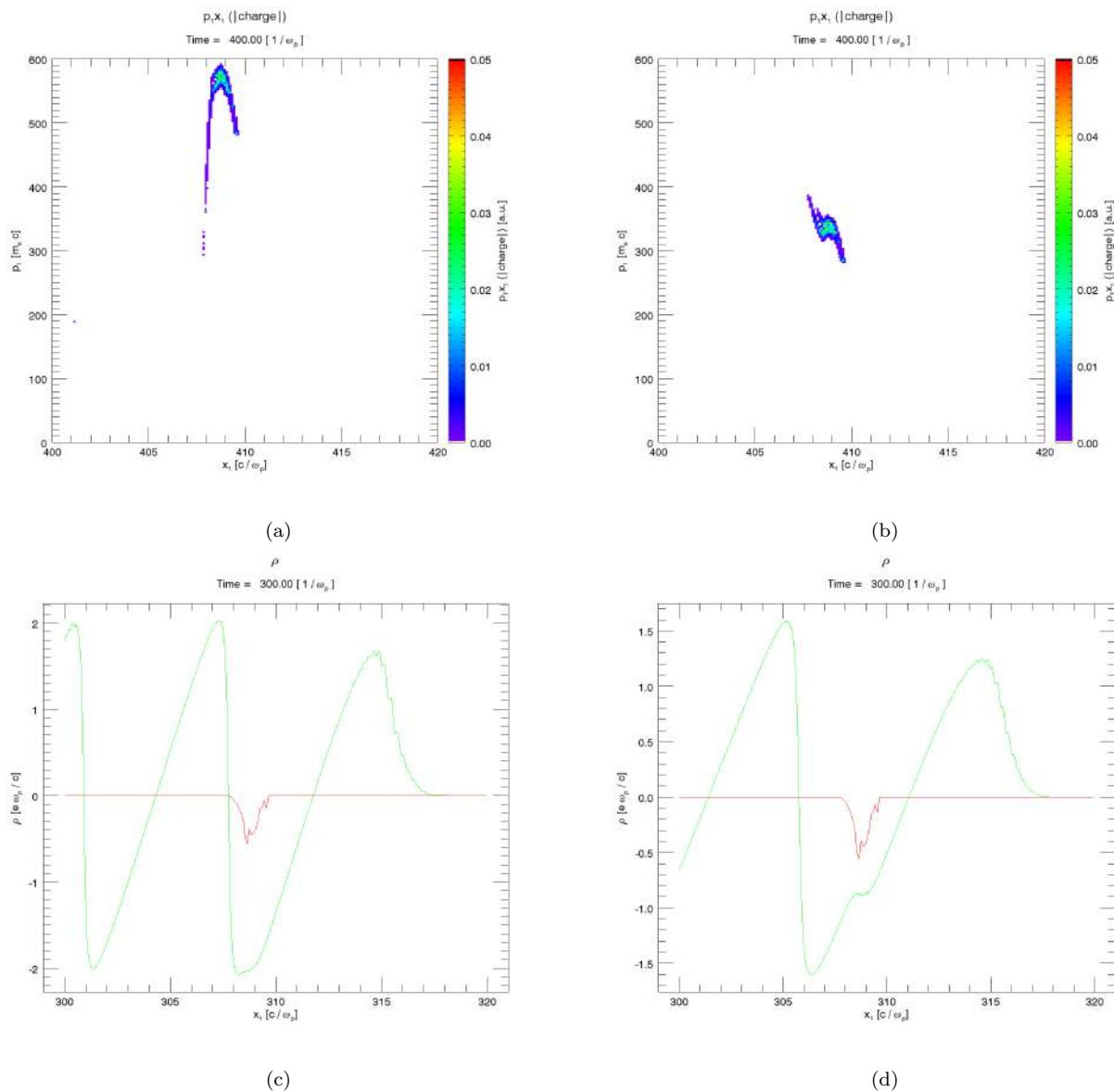
(a)

(b)

(c)

(d)

Figure 4: Comparison of ongitudinal phase space of the electron beam in the case with the stairs density profile (a) and with uniform density profile (b) at $400 \ \omega_p^{-1}$. The shape of the beam in the phase space is given by the shape of the accelerating field. Analyzing the process at $300 \ \omega_0^{-1}$, in (c) the beam is phase-locked with the maximum acceleration point of the wake. Here, the tail of the beam feels a different decelerating field and so it is not uniform accelerated with the rest of the beam. Instead in (d) the beam is in a region of flat field, and so the shape of the phase space shows less spread.

$\sim 12\%$ to $\sim 9\%$.

6. Conclusion

We used a combination of tailored plasma composition and density profile to create electron beams with a maximum energy of 285 MeV and a relative energy spread of 9%. The energy quality of the beams obtained using the tailored density profile are increased compared to the beams propagated into uniform density profile. In particular, we increased the maximum energy of the beam by 68% and reduce the

relative energy spread by 25%.

The use of the technique presented in this work also reduce the total charge of the beam to 0.65 arbitrary units, 28% less than the beam propagated into uniform density profile.

This work inspires new analysis on this technique, in particular we want to reduce the charge lost and investigate the effects of the combination of tailored composition and profile on other characteristics of the beam, as the duration of the phase-lock and wake.

[1] T. Tajima and J. M. Dawson, "Laser electron accelerator," *Phys. Rev. Lett.*, vol. 43, pp. 267–270, Jul 1979.

[2] E. Esarey, C. B. Schroeder, and W. P. Leemans, "Physics of laser-driven plasma-based electron accelerators," *Rev. Mod. Phys.*, vol. 81, pp. 1229–1285, Aug 2009.

[3] W. Lu, M. Tzoufras, C. Joshi, F. S. Tsung, W. B. Mori, J. Vieira, R. A. Fonseca, and L. O. Silva, "Generating multi-gev electron bunches using single stage laser wakefield acceleration in a 3d nonlinear regime," *Phys. Rev. ST Accel. Beams*, vol. 10, p. 061301, Jun 2007.

[4] S. Myers and E. Picasso, "The design, construction and commissioning of the cern large electron–positron collider," *Contemporary Physics*, vol. 31, no. 6, pp. 387–403, 1990.

[5] V. Malka, J. Faure, Y. A. Gauduel, E. Lefebvre, A. Rousse, and K. T. Phuoc, "Principles and applications of compact laser–plasma accelerators," *Nature Physics*, vol. 4, no. 6, pp. 447–453, 2008.

[6] J. Osterhoff, A. Popp, Z. Major, B. Marx, T. P. Rowlands-Rees, M. Fuchs, M. Geissler, R. Hörlein, B. Hidding, S. Becker, E. A. Peralta, U. Schramm, F. Grüner, D. Habs, F. Krausz, S. M. Hooker, and S. Karsch, "Generation of stable, low-divergence electron beams by laser-wakefield acceleration in a steady-state-flow gas cell," *Phys. Rev. Lett.*, vol. 101, p. 085002, Aug 2008.

[7] W. P. Leemans, A. J. Gonsalves, H.-S. Mao, K. Nakamura, C. Benedetti, C. B. Schroeder, C. Tóth, J. Daniels, D. E. Mittelberger, S. S. Bulanov, J.-L. Vay, C. G. R. Geddes, and E. Esarey, "Multi-gev electron beams from capillary-discharge-guided subpetawatt laser pulses in the self-trapping regime," *Phys. Rev. Lett.*, vol. 113, p. 245002, Dec 2014.

[8] A. Pak, K. A. Marsh, S. F. Martins, W. Lu, W. B. Mori, and C. Joshi, "Injection and trapping of tunnel-ionized electrons into laser-produced wakes," *Phys. Rev. Lett.*, vol. 104, p. 025003, Jan 2010.

[9] W. Rittershofer, C. Schroeder, E. Esarey, F. Grüner, and W. Leemans, "Tapered plasma channels to phase-lock accelerating and focusing forces in laser-plasma accelerators," *Physics of Plasmas (1994-present)*, vol. 17, no. 6, p. 063104, 2010.

[10] R. Fonseca, L. Silva, F. Tsung, V. Decyk, W. Lu, C. Ren, W. Mori, S. Deng, S. Lee, T. Katsouleas, and J. Adam, "Osiris: A three-dimensional, fully relativistic particle in cell code for modeling plasma based accelerators," in *Computational Science — ICCS 2002* (P. Sloot, A. Hoekstra, C. Tan, and J. Dongarra, eds.), vol. 2331 of *Lecture Notes in Computer Science*, pp. 342–351, Springer Berlin Heidelberg, 2002.

A review on ray propagation on turbulent media

Hugo obtained his Masters Degree in Physics Engineering in 2014, from IST/University of Lisbon. During his Erasmus experience at Padova University (Italy) in 2012, he started to become strongly interested in plasmas. Visiting RFX-mod has made him understand, in its full extension, the beauty and complexity underlying the science and engineering of Nuclear Fusion.

After that he has worked as a research fellow at IPFN from 2013 to the end of 2014, towards his MSc degree. There, he studied microwave engineering and performed the assessment and simulation of the different configurations proposed for the antennas of the plasma-position reflectometry system to be assembled on ITER.

Although he has interests in all areas of Physics, his preferences lie between modeling and experimental Physics.

Hugo Hugon

Instituto de Plasmas e Fusão Nuclear, Instituto Superior Técnico,Universidade de Lisboa, 1049-001 Lisboa, Portugal

E-mail: `hhugon@ipfn.tecnico.ulisboa.pt`

September 2015

Abstract. We make a review on propagation of light beams through turbulent media, providing the main theoretical approaches for the problem and their accuracy and application conditions, and the evolution of the subject throughout the history. We concentrate on the turbulent ray propagation in fusion plasmas, and in most recent works in the area, and point out the important aspects and results of each approach. The review embraces the subject in a way that any person with the fundamental knowledge of physics can follow, and tries to give the reader the bibliographic references to engage on a more profound manner.

1. Motivation

Ray propagation in turbulent media is important in many areas of research, from astronomy and free-space communications to fusion plasmas. In this review we discuss of the propagation of light beams through turbulent media, summarizing the main theoretical approaches for the problem, their accuracy and application conditions. We then concentrate on propagation on fusion plasmas. The objective is to point out only the important aspects and results of each approach, giving the reader with fundamental knowledge of physics the references for a more specific approach. The quality of an optical beam is significantly degraded while traversing earths turbulent atmosphere over long distances. Local temperature gradients create refractive-index fluctuations ([1], [3]), which are are responsible for beam wandering, fluctuations in the irradiance, frequency and polarization, a decrease on spatial and temporal coherence, and angle-of-arrival fluctuations ([2]). The design of free-space optical communication systems, such as satellite or radar communications ([3]), has to be designed in order to overcome the turbulence-induced degradation. This also applies for astronomy, concerning the image degradation seen on telescopes, such as image instability and twinkling of stars (so called scintillation effect, due to fluctuations in the beam intensity). Turbulence has a relevant impact in all remote sensing applications, which aim to probe turbulent plasmas, hydrodynamic flows or the atmosphere, where it is important to understand the turbulent properties of the medium. A good example is the probing of fusion plasmas in tokamaks with microwave reflectometry, where signal-to-noise ratio is dependent on the turbulence effects, which cause scattering, diffraction and refraction of the probing waves [7]. A good knowledge of ray propagation in tokamaks is important for the heating of plasma heating and current generation with rf-waves [8], [9].

2. The Theoretical Formulation

The earliest works are credited to Tatarskii (1961) [4] and Chernov (1960). They describe the propagation of an optical wave through turbulent media based on the geometrical-optics approach (WKB method, eikonal method, etc.) independent of frequency, from which the ray trajectories and the times of flight are obtained. In fact, many problems of electromagnetic wave propagation can be solved by this technique. Sound propagation has a theoretical treatment comparable to electromagnetic wave scattering. An example on the treatment of sound propagation in turbulent atmosphere can be found in [6]. Reference [10] exemplifies how broad this field can be. It presents a geometrical-optics method for isotropic and anisotropic media, as well as an elegant Lagrangean approach in dispersive media.

The variations of the refractive index are often modelled as eddy-viscosity models, where turbulence is displayed as turbulent eddies in the medium. This concept was first introduced by Kolmogorov (1941, [18]). Usually one defines the correlation distance of these eddies as the inner (l_0) and outer (L_0) scales of the turbulence. The larger eddies dissipate and transfer its initial kinetic energy into smaller eddies. This process continues into smaller and smaller scales (inertial range) until a scale where fluid viscosity effects have importance, and the kinetic energy dissipates into internal energy (see Figure 1 and Figure 2). Eddy viscosity models can be divided into algebraic, one-equation and two-equation models. They are constructed under the idea that the average turbulent flow is approximated to a certain laminar flow. In these models the turbulent conduction and viscosity are properties of the flow, and are used to express the turbulent stresses and fluxes. In zero equation models a simple algebraic equation, based on dimensional analysis, is used to close the problem in terms of the transport of the turbulent stresses and fluxes (see Prandtls mixing length model, 1925 [31] or the Cecebi-Smith model,1967 [32]). In one equation models the conduction and viscosity are expressed as functions of the turbulent kinetic energy (k), which is obtained through a partial derivative equation (PDE). Here, the pressure diffusions and the eddy dissipation rates () need to be modeled (see Spalart and Alamaras model, [33]). In two equation models two PDEs are used, one for the kinetic energy and one for the dissipation rate and viscosity are set as a function of the two variables. Because of this these are also called $k - \epsilon$ models. Laura and Sharma (1974, [34]) model is considered the standard $k - \epsilon$ model. Based on thisprinciples, a great number of free and commercial computational fluid dynamics (CFDs) codes are being used.

Geometrical optics are valid for propagation lengths of $\sim kl_0^2$ [3], where k is the wavenumber. In [11] the validity of geometrical optics is defined as $\sqrt{\lambda L} \ll l_0$, where L is the propagation path and the wavelength. Figure 1 (adapted from [11]), illustrates the validation conditions for geometrical optics, and when diffraction effects should be taken into account.

An elegant use of the eikonal method on MHD is provided in [12]. The same method is applied in [13] in toroidal ray tracing code for the study of lower-hybrid current drive. Colestock points out the importance of geometrical optics in the treatment of lower hybrid waves in uniform plasmas [14], due to the short wavelengths compared to the gradients scales. In this limit the wave amplitude varies slowing along
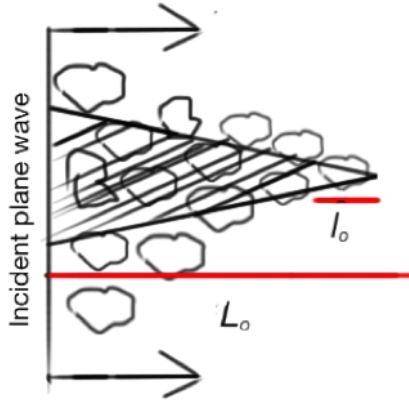
Figure 1. The shaded area correspond to the effective scattering by the turbulent eddies. L is the propagation path, and the closed structures represent the eddies. Up: condition of $\sqrt{\lambda L} \ll l_0$, where geometrical optics apply. Down; condition of $\sqrt{\lambda L} \gg l_0$, where diffraction effects should be taken into account. Figure adapted from [11].

the optical path, so that the wave parameters can be calculated locally from the dispersion relation.

Trying to improve the limitations of the geometrical approach, in the early 1960s Tatarskii and Chernov provided a more complete description of the problem, applying a method proposed by Rytov [15]. This methods results agreed with experimental data for scintillation theory in the condition of weak turbulence and for propagation paths of less than 1km. Rytovs method assumes that the wave intensity fluctuations are small compared to the turbulence scales [16]. It works well for short distances of propagation or weak turbulence conditions. However, it failed for longer paths since it does not take properly into account [3] the contribution of the turbulent eddies for the multiple wave scattering. To take these effects into account, different techniques were then used such as the Markov and Born approximations, or the method of small perturbations, first introduced by Chernov.

The refractive index is often described (without any loss in generality) as an average $\bar{n}_0$ plus a fluctuating part n_1:

$$n(r,t) = \bar{n}_0(r) + n_1(r,t), \tag{1}$$

where $\langle n_1 \rangle = 0$, by definition. Sometimes the media configuration (e.g. density fluctuations) can be considered as frozen in each individual realiztion, since the turbulent structures frequency is considerably lower than the wave frequency [8]. As stated before, the fluctuating part (n_1) has a random behavior related to the random spectral amplitude [19]. Local homogeneous fields, which allow a varying mean and statistical homogeneous fluctuations around the mean are characterized by structure functions. These functions are closely related to the correlation or

covariance function between two points in space, lets say, r_1 and r_2, with $r = |r_1 - r_2|$. The structure factor, defined as [17]:

$$D_n = \langle [n(r_1 - r) - n(r)]^2 \rangle \,(2) \tag{2}$$

Where $\langle . \rangle$ represents an ensemble average. The correlation function of two observation points a distance apart along the line-of-sight of the propagation is of great importance, since It allows the calculation of the ensemble averages over the field variables in a random media. The ergodic hypothesis states that the infinite time average of a random process is equal to the ensemble average of the same process. Since it is usually impossible to have an identical ensemble of systems that we can analyse, the ergodic hypothesis is often used with a reasonable averaging time (not infinite of course, as the ergodic hypothesis assumes) [1]. The process for the estimation of the desirable averaging time to achieve the accuracy needed can be found on [19] and [20]. Another important quantity is the power spectrum $\phi(k)$ of the refractive index fluctuations. It is, apart from constants, the Fourier transform of the correlation or the structure function. In summation, it provides the spectrum or wave number domain representation of our problem, while the structure function represents the spatial description.

Great attention was given to find the best model for the power spectrum $\phi(k)$, which reflects the statistical properties of the turbulent media. Kolmogorov, Tatarskii and von Karman dedicated some of his work on this question. Kolmogorov has the most known and simple power law spectrum [18] that considers the inner (lo) and outer scales (Lo) as zero and infinity, respectively (see eq. (2.35) and (2.36) of ref. [1]). This spectrum is commonly subject to modifications: when the inner and outer scales cannot be ignore, one needs to use, for example, Tatarskii and von Karman spectra, to obtain more physically meaningful and accurate expressions (ref.[6] is an example where the Karman spectrum is used for the sound wave propagation in turbulent atmosphere). Tatarskii spectrum extends the sadKolmogorov spectrum into the dissipation range (eddy wave number $k > 1/L_0$). Von Karman spectrum is valid for both inner and outer scale effects, such that $(0 \leq k <)$. Figure 2 shows the typical turbulence spectrum evolution with the eddy wavenumber size.

In the Kolmogorovs inertial subrange model, the structure factor has the form:

$$D(r) = C_n^2 r^{(2/3)}, \quad l_0 \ll r \ll L_0 \tag{3}$$

An example of the Karman spectrum, used by (Chernov,1961), is shown on equation (4):

$$_K arman(r,k) = 0.033 \times C_n^2 . exp[-((kl_0)/2)^2]/[k^2 + L_0^{(}-2)]^{(}11/6), \tag{4}$$
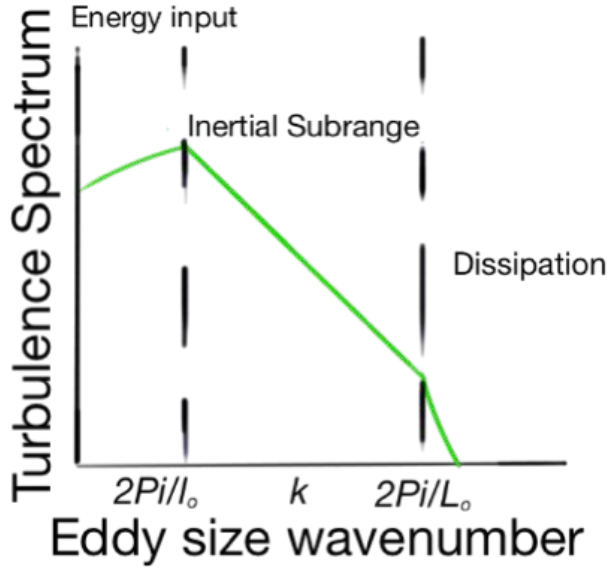
Figure 2. Turbulence spectrum evolution with the eddy size wavenumber. The energy is input at the outer scale Lo, and it cascades with the Kolmogorov law $k^{-11/3}$, where $k = 2/(\text{eddy size})$, until it reaches the l_0 scale where it dissipates.

where k is the wavenumber. Usually, the correlation functions, as well as the power spectra, are constructed with constant parameters [the structure constant C_n in equations (3) and (4)]. These parameters are dependent on the specific conditions of the application (e.g. weak or strong turbulence). It should be noted that, in practical terms C_n is not really constant, since it is a function of time and space, which describes the strength of the refractive index turbulence. The appropriate averaging times should be used to determine these constants [1]. In Figure 3 we show the example of the behaviour of C_n of the atmosphere over a period of 20 hours (image taken and adapted from ref. [1]). It illustrates how important it is the right definition of the structure factors over a time averaging for a specific application.

An example of a formal method on wave propagation is given by Tatarskii in [19]. It shows how to use the small perturbations technique to obtain the spectral amplitudes of amplitude and phase fluctuations of a plane wave incident on a random medium (note that this approach does not take into account other important quantities, such as the angle-of arrival fluctuations [1]). It starts from the Maxwell equations to obtain the wave equation for the electric field vector E for the case $\lambda \ll l_0$:

$$\nabla^2 E + k^2 n^2 E = 0, \qquad (5)$$

where n is given by equation (1), and expands E into E^m decreasing terms with powers of n_1, truncating E at the first order (single scattering): $E = E_0 + E_1 + ...$ Equation (5) is solved in this approximation, assuming

a plane wave propagates in the z direction, and that the scattering due to turbulence in the perpendicular direction is much smaller than the propagation path length in z (Fresnel approximation). The perturbative term n˙1 is treated in such a way that is statistically homogeneous in each plane perpendicular to the line-of-sight propagation, but remains a function of the z coordinate. A solution is obtained for the random spectrum fluctuations of E. Due to the assumption of statistical homogeneity, averaging of the first order fluctuations is zero by definition: $< n_1 > = < E_1 > = 0$. This is the point where the second order (or higher order, if taken into account) functions, like the covariance, correlation or the structure function of equation (2) yield a great importance in practical terms, since they use the fluctuations present in n˙1 in the time-averaging description of the experiment. It is while working with these functions that the necessity to properly define the power spectrum (k) appears.

3. Ray Propagation in Fusion Plasmas

The analysis of ray propagation is of great importance in fusion devices such as Tokamak, since just small fluctuations of the refractive index can give rise to significant scattering of electromagnetic radiation. This becomes in the use of RF-waves (e.g. electron cyclotron, lower hybrid waves) are used for auxiliary plasma-heating, current drive, temperature profile control or the construction of power deposition profiles.

In fusion experiments the wavelength is usually small compared to the gradient scales of the inhomogeneous media. This is a condition where geometric optics and ray tracing can be applied. Ray tracing gives a physical picture in terms of wave ray propagation, however typical wave effects are neglected in this approach, like interference and diffraction, or the formation of caustics (regions where the rays are densely packed), which break the geometrical approximation. These effects can be analyzed by the use of full wave solutions, quasi-linear optics or paraxial beam tracing [30] (a review on the validity of asymptotic methods such as geometrical optics and beam-tracing methods in the context of fusion experiments is given in [29]). Instead of the single use of ray-tracing, one of the most common procedures seen in the literature is the use of a ray-tracing technique coupled with a Fokker-Planck code. It aims to analyse the propagation and amplitude transport of RF waves (e.g. electron-cyclotron, lower-hybrid) in the geometrical optics limit ([8] [13] [14] [21]), with the assumption that no effect on the refraction index profile from the local intensity of the propagating wave exists. The ray tracing equations following the Hamiltonian theory are given by [13] and
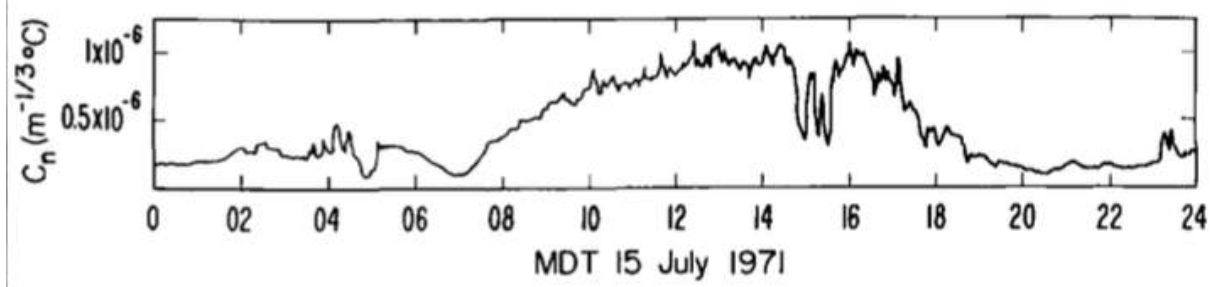
Figure 3. Variation of the refractive index structure factor Cn over a period of 24 hours on a clear sunny day, 2 meters above the ground. (image taken from ref. [1], Fig.2.1, page 21).
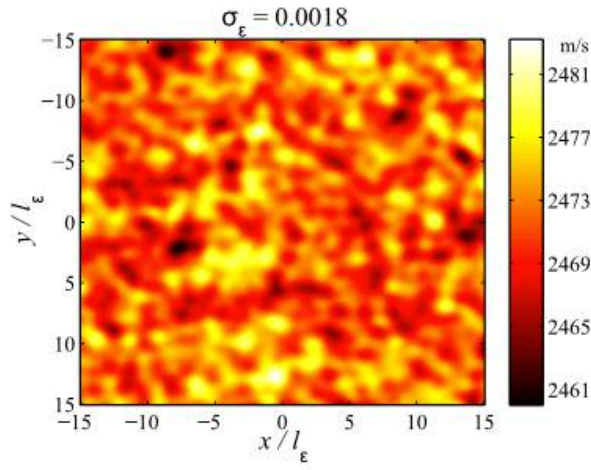

Figure 4. 2D random media created with Gaussian turbulent structures. 2D map normalized to the characteristic length of the turbulence (image taken from ref. [25], Fig.1, page 3)

[24]:

$$\frac{dX_i}{dt} = -\frac{\partial D}{\partial k_j} \Big/ \frac{\partial D}{\partial w}, \tag{6}$$

$$\frac{dk_j}{dt} = -\frac{\partial D}{\partial X_i} \Big/ \frac{\partial D}{\partial w}, \tag{7}$$

where the position coordinates X_i of the position vector X are canonical conjugates of the phase space coordinates k_j of the wavevector k. D is the dispersion relation that obeys [24]:

$$D(X, k, w, t) = 0, \tag{8}$$

and w is the constant wave frequency imposed by the generator and t is the time evolution parameter subject to $\partial D/\partial t = 0$. Figure 4 (taken and adapted from [25]) shows a generated 2D random media with Gaussian random structures. The red colour indicates stronger turbulence.

Figure 5 (taken and adapted from [25]) shows the ray propagation through the Gaussian random media of Figure 4 via a ray tracing technique [25].

In the combined ray-tracing and Fokker-Planck code, ray-tracing is used to compute the quasilinear diffusion coefficient necessary as an input for the Fokker-Planck equation, that works as a master equation [13]. In [21], Bizarro et al addresses the problem of stochastic divergence of the rays, since as the ray paths become longer, geometrical optics break down and probabilistic processes have to be used. It shows that ray stochasticity cannot be ignored for models used to compute power-deposition profiles. Ref. [22] provides an analytical method for the analysis of LH wave propagation, using a cold-plasma approximation and a Hamiltonian approach, in order to overcome some of the ray-tracing limitations. More recently, Peysson, et al [24] developed a new ray-tracing code to study rf waves, which uses magnetic flux coordinates instead of the common toroidal coordinate system. This methodology gives rise to a more complex problem in terms of metrics. However, it has the advantage of allowing a much less time consuming method than the codes with toroidal geometry. An example of the usage of this code (C3PO) is presented in [23] for RF waves for current drive applications. As before, in this procedure the code is completed with a Fokker-Planck code.

Random inhomogeneities create often a complicated scenario to be described deterministically. Also, a large number of random media scenarios are needed to provide a statically complete description of ray tracing.

This often leads to very time-consuming, repetitive and computationally heavy processes making room for cumulative numerical errors. Concerning this, as in [21], Bo Lu [25] shows the advantages of a stochastic approach over a deterministic one (geometric optics method coupled with Runge Kutta technique) using a stochastic modelling technique. The validity of using stochastic perturbations on the electron density profile is mainly because the beam lives for a much longer time than the correlation time of the turbulence [26]. In this work a new Monte-Carlo code (WKBeam) is used. This code is used in [27] to show that in ITER,
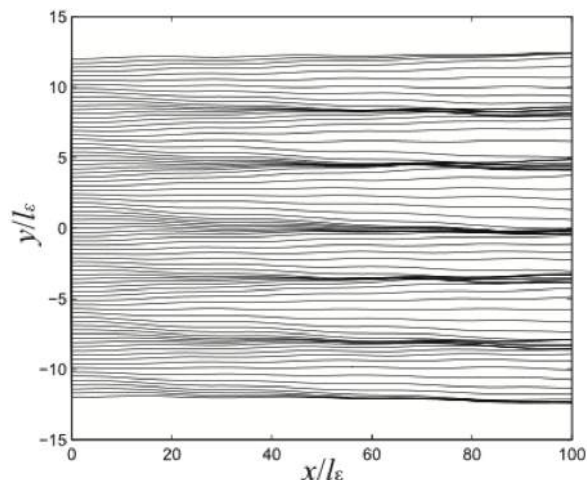
Figure 5. Ray tracing of a pencil of rays through the 2D random media created with Gaussian turbulent structures of Figure 5 (image taken from ref. [25], Fig.2, page 4).
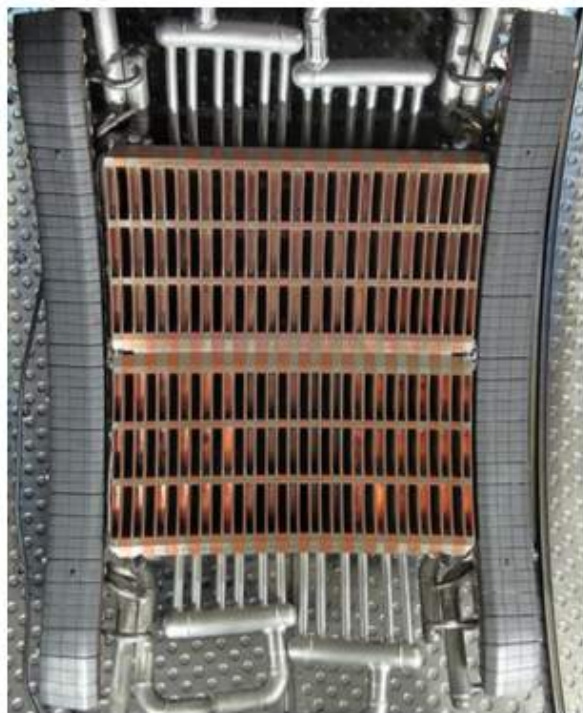

Figure 6. Array of Lower Hybrid antennas, designed for Tore Supra tokamak. Image taken from [30].

fluctuations $\delta n_e / n_e \sim 10\%$ around the plasma edge can broaden of the absorption profile by about a factor of two A different approach is the use of stochastic rendering, which can be compared to bump mapping of images to smooth their surfaces. It consists of a set of pre-computed vectors that perturb the rays following the stochastic model suitable for the application [28].

4. Conclusion

Ray propagation in turbulent media is a subject of great interest in a wide range of areas. The first works from Tatarski and Chernov were focused on the atmospheric turbulence, and set the foundations for ray propagation in turbulent media theory. One of the most important problems is the definition of the turbulence random fluctuations and how to treat them with a physical meaning, by means of correlation or structure functions of the wave field variables. Different asymptotic methods are available, which can differ more or less from geometrical optics. While the validity of geometrical optics breaks down for long propagation paths, it is widely used in the study of ray propagation in fusion plasmas. Great part of the literature is focused on the use of rf waves for current drive and plasma heating or temperature control applications. The most common approach is the hybrid use of geometrical optics (ray tracing) with a Fokker-Planck equation, and one of the critical aspects of the procedure is the model of the refractive index fluctuations. One of the problems of ray tracing is that it does not take into account wave effects, and its validity breaks down in several situations. Recently, several studies show the construction of new codes to overcome the limitations of ray tracing, such as quasi-optical or paraxial ray tracing, finite element methods or stochastic and monte-carlo modelling.

5. Aknowledgements

References

[1] Clifford, S. F., The Classical Theory of Wave Propagation in a Turbulent Medium, Vol.25, Topics in Applied Physics, pp.9-43, July 2005

[2] Clifford, S. F., The Classical Theory of Wave Propagation in a Turbulent Medium, Vol.25, Topics in Applied Physics, pp.9-43, July 2005

[3] Wang, F. et al,Propagation of Partially Coherent Beam in Turbulent Atmosphere: A Review, Progress In Electromagnetics Research, Vol. 150, 123143, 2015.

[4] Fante, Ronald L., Electromagnetic Beam Propagation in Turbulent Media, Proceedings of the IEEE, Vol. 63, No. 12, December, 1975

[5] V. I. Tatarski, Wave Propagation in a Turbulent Medium. New York: McGraw-Hill, 1961

[6] L. Chernov, Wave Propagation in a Random Medium, MacGraw Hill, New York, 1960

[7] A.P. Oliveira, The effect of wind and turbulence on sound propagation in the atmosphere, Master Thesis, Technical University of Lisbon, Portugal, 2012.

[8] Varela, P., Automatic time-frequency analysis for plasma density profile evaluation from microwave reflectometry, PhD Thesis, Universidade Tcnica de Lisboa, Instituto Superior Tcnico, July 2002.

[9] Hansen, F.R, et al, Ordinary Wave Propagation in a Tokamak with Density Fluctuations, IOP Nucl. Fusion, 28, pp. 769-778, 1988.

[10] Peysson Y, et al, RF current crive and plasma fluctuations, Plasma Phys. Control. Fusion, 53, 045003 (16pp), 2011

[11] Kravtsov, Yu. A., et al., Geometrical Optics of Inhomogeneous and Nonstationary Dispersive Media, Proceedings of the IEEE, Vol.62, 11, November 1974

[12] J.W.Strohbehn, Line-of-Sight Wave Propagation Through the Turbulent Atmosphere, Proc. IEEE , 56, 1301

[13] Weinberg, Steven, Eikonal Method in Magnetohydrodynamics, The Physical Review, Second Series Vol. 126, 6, pp.1899-909, 1962

[14] Bonoli P T, et al 1986 Simulation model for lower hybrid current drive Phys. Fluids, no. 29, pp. 293750

[15] Colestock, Geometric Optics of Lower Hybrid Waves in Nonuniform Plasmas IEEE Transactions on Plasma Science, Vol. Ps-8, 2, pp. 71-77, June 1980

[16] S.M. Rytov, Modulated oscillations and waves, Tr.Fiz. Imt. Akad.NaukSSSR, vol. 2, pp.40-133, 1940

[17] Prokhorov, A.M., et al., Laser irradiance propagation in turbulent media, Proceedings of the IEEE, Vol. 63, 5, pp. 790-811, May, 1975

[18] Yuksel,H., Studies of the Effects of Atmospheric Turbulence on Free Space Optical Communications, PhD Thesis, Faculty of the Graduate School of the University of Maryland

[19] Kolmogorov, A. N., The local structure of turbulence in incompressible viscous fluid for very large Reynolds numbers Doklady Akademiia Nauk SSSR, Vol. 30, No. 4, 301305, 1941.

[20] V. I. Tatarski, The effects of the turbulent atmosphere on wave propagation, Jerusalem: Israel Program for Scientific Translations, 1971

[21] Taylor, G. I., Eddy motion in the atmosphere, Phil. Transactions R. Soc. Lond., 215, pp.1-26, 1915

[22] Bizarro, J. P. et al., On ray stochasticity during lower-hybrid current drive in tokamaks, Phys. Fluids B 5 (4), April 1993

[23] Esterkin, A. R. et al., Analytical approach to lower hybrid ray tracing Nuclear Fusion, Vo1.32, No.6, pp.927-32, 1992

[24] Peysson Y, et al, RF current crive and plasma fluctuations, Plasma Phys. Control. Fusion, 53, 045003 (16pp), 2011

[25] Peysson Y, et al, A versatile ray-tracing code for studying rf wave propagation in toroidal magnetized plasmas, Plasma Phys. Control. Fusion, 54, 045003 (16pp), 2012

[26] L, Bo et al, Stochastic simulation of the high-frequency wave propagation in a random medium, Journ. Of Applied Physics, 112, 054902, 2012 Hannes Webber, 2015

[27] Poli, E., et al, Scattering of electromagnetic wave beams from density fluctuations in tokamak plasmas, 42nd EPS Conference on Plasma Physics, P1.174, 2015

[28] Starn, J. et al., Ray Tracing in Non-constant Media

[29] Tsironis, C., On the Simplification of the Modeling of Electron-Cyclotron Wave Propagation in Thermonuclear Fusion Plasmas, Progress In Electromagnetics Research B, Vol. 47, 3761, 2013

[30] Horton, W. et al., Penetration of lower hybrid current drive waves in tokamaks , Phys. Plasmas 20, 112508 2013

[31] Prandtl, L., On Fully Developed Turbulence, Z.A.M.M.,Vol.5, pp.136-139, 1925

[32] Smith, A.M.O. and Cebeci, T., "Numerical solution of the turbulent boundary layer equations", Douglas aircraft division report DAC 33735, 1967

[33] Spalart, P. R. and Allmaras, S. R., "A One-Equation Turbulence Model for Aerodynamic Flows", La Recherche Aerospatiale, n 1, pp. 5-21, 1994

[34] Launder, B. E., and Sharma, B. I. "Application of the Energy Dissipation Model of Turbulence to the Calculation of Flow Near a Spinning Disc", Letters in Heat and Mass Transfer, vol. 1, no. 2, pp. 131-138, 1974.

Low temperature plasma medicine

Marija comes from Serbia, where she received BSc and MSc degree in general physics from University of Nis. After her master studies, she worked as a teaching associate at the Faculty of Science and Mathematics, where she graduated.

Her interest for physics began in the earliest stages of her education. That interests towards science led her to enroll in a special class for physics, which is one of a kind in Serbia. During her studies, she participated in organizing of a few seminars, science festivals, as well as advertising of the grammar class she attended.

Throughout the studies, she found the courses regarding plasma physics the most appealing, and this is the area of physics where she wishes to engage in scientific research.

Marija Grofulović

Instituto de Plasmas e Fusão Nuclear, Instituto Superior Técnico, Universidade de Lisboa
Avenida Rovisco Pais, 1049-001 Lisboa, Portugal

E-mail: `m.grofulovic@gmail.com`

Abstract. Biomedical applications, recently became an increasing application field of gas discharges. Gas discharge plasmas formed at atmospheric pressure and near room temperature are potentially useful for surface and wound sterilization, antisepsis, bleeding cessation, wound healing and cancer treatment. Plasma medical devices and associated biochemical effects are complex and still not fully understood, which makes this field very challenging. Plasma jets and floating-electrode dielectric barrier discharges (FE-DBDs) are presented in this paper as plasma sources successfully used in many studies on this mater. Reactive oxygen and nitrogen species (RONS), created in plasma, are stressed out as the most probable agents responsible for the success of plasma-based medical applications. Cancer therapy is presented as a very promising application of cold atmospheric plasmas.

1. Introduction

Biomedical devices working with near-room temperature gas discharge plasmas at atmospheric pressure is now well established. Plasmas have been used in biomedicine for a long time for sterilization of medical equipment, packaging in the food industry, implants, blood coagulation, etc [1]- [8].

In recent years, the devices that use cold (less than 40 ^{o}C at the point of application) atmospheric plasmas have been developed that provide the possibility to extend plasma treatment to living tissue. Usually they use either rare gas (He, Ne, Ar) jets or dielectric barrier discharge (DBD) in air. These simple devices are shown to be effective in killing bacteria, viruses and fungi in solution and on surfaces [10].

Besides the new developing technologies based on cold atmospheric plasmas, there are also plasma-based electrosurgical devices and technologies that had been used for decades. In surgery, plasma devices are used in applications including tissue cutting, coagulation, desiccation (water removal) and cauterizing or fulgurization. One example of such a device is the Argon Plasma Coagulator (APC) [9]. These technologies operate via heating the tissue with electrical current and so the effects are primarily thermal. We can not say the same for the cold atmospheric plasma devices that transfer little heat. The effectiveness of cold atmospheric plasma might be due to electric field, photons, charge accumulations, but central to their treatment success are probably reactive chemical species created in plasma [29].

The mechanisms of mammalian cells reaction to cold atmospheric plasmas are yet not fully known. Moreover, we do not know for certain what chemical species created in plasma are most biologically important. What has been observed is that in general when plasma is operated at higher power for longer times and closer to the treated tissue, the effects are more pronounced. This means that the treatment with cold atmospheric plasma is dose-dependant [29], as stated in the study presented in section 4.

The most likely active agents responsible for the observed effects are the reactive chemical species, especially reactive oxygen and nitrogen species (RONS) created in plasma. One of the reason for this is the fact that RONS are known to be centrally important in animal and plant immune systems. RONS are used in the fight against invading microbes and parasites, against tumors and in response to wounds. Even different therapies are known to directly or indirectly involve RONS. An interested reader can find a more detailed review on the role of RONS in plasma biomedicine that was recently published [11].

The most commonly used plasma devices in biomedical applications are presented in the following section. The third section emphasizes the importance of RONS in the biochemistry of the immune system. Cancer therapy is presented in the forth section as a promising area for using plasma techniques.

2. Structure and composition of plasma jets

One of the most common configurations used for the cold atmospheric plasma treatment is the rare gas plasma jet. The gas used here is usually He or Ar, pure or with small amounts of molecular gas such as O_2 and/or N_2. The device is composed of a dielectric tube on the order of 1 cm in diameter and one or two ring electrodes placed around it peripherally. Figure 1 shows a plasma needle as an example of cold atmospheric plasma devices. In AC-driven devices, the operating conditions are the following: the applied powers are usually around 1W; gas temperature is on the order of 300-350 K; the excitation voltage is usually $\sim$5-20 kV and frequency $\sim$1-30 kHz [29]. Laroussi *et al* presented AC-driven, pulsed DC-driven and RF-driven plasma jets in a review on cold atmospheric plasma jets [18].

The other commonly used configuration is the floating electrode dielectric barrier discharge (FE-DBD) shown in figure 2. With this device, the plasma is generated between a quartz-insulated high-voltage electrode and the sample which is not grounded and remains at a floating potential. Applying a high-voltage (10-40 kV), the discharge ignites when the distance between the powered electrode and the sample is less than 3 mm. The working gas is ambient air. Typical values of input power are around 35 W resulting in a surface power density of 0.5-1.0 W/cm^2 [31, 32, 33].
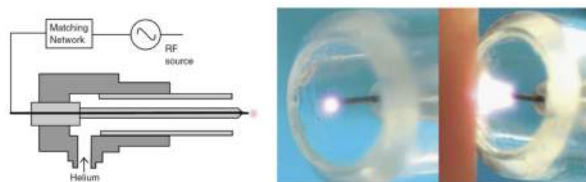

Figure 1. Left: schematic drawing of the plasma needle [16]. Right: Plasma needle in operation mode [17].

There are several other types of cold atmospheric plasma devices that have been tested over the last several years, including microwave plasmas and dielectric barrier discharges, where the discharge is sustained between two electrodes separated by an insulating dielectric barrier in air [13, 14]. Regardless of the type of plasma source, they all produce significant quantities of reactive species, and especially reactive oxygen and nitrogen species. These species are important players in normal biochemistry.
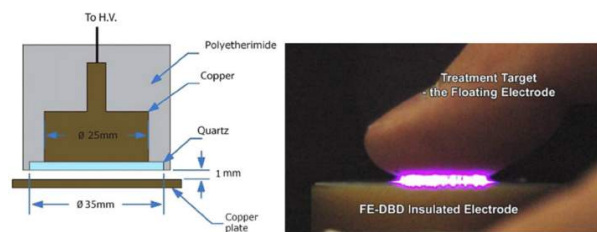
Figure 2. Left: schematic of the cylindrical round floating electrode dielectric barrier discharge (FE-DBD). Right: FE-DBD in action [33].

3. RONS in the immune system

RONS are known to be involved in functioning of the immune system. Macrophages and neutrophils (white blood cells) defend an organism by creating and using various RONS.

ROS	Formula	Plasma reactions
Hydrogen peroxide	H_2O_2	$OH \cdot + OH \cdot \rightarrow H_2O_2$
Hydroxyl radical	$OH \cdot$	$e + N_2 + M \rightarrow N_2^+ + 2e + M^{a)}$ $N_2^+ + H_2O \rightarrow N_2 + H_2O^+$ $H_2O^+ + H_2O \rightarrow OH \cdot + H_3O^+$
Superoxide	O_2^-	$e + O_2 + M \rightarrow O_2^- + M$
Singlet oxygen	$O_2(^1\Delta_g)$	$O_2 + e \rightarrow O_2(^1\Delta_g) + e$

$^{a)}$(M – Third body particle)

Figure 3. Cold atmospheric plasma production of biologically relevant ROS [25]

RNS	Formula	Plasma reactions
Nitric oxide	NO	$N_2 + e \rightarrow N + N + e$ $N + O + N_2 \rightarrow NO + N_2$
Peroxynitrite	ONOO-	$NO + O_2^- \rightarrow ONOO^-$
Nitrite	NO_2^-	$NO + O_3 \leftrightarrow NO_2 + O_2$ $2NO_2 + H_2O \rightarrow HNO_2(aq) + HNO_3(aq)$

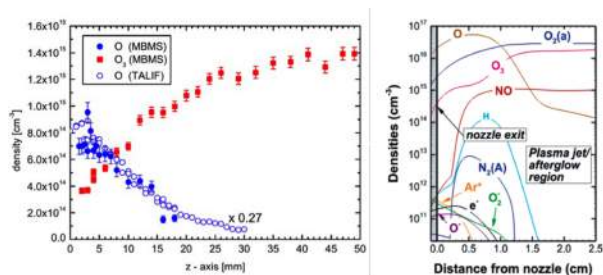**Figure 4.** Cold atmospheric plasma production of biologically relevant RNS [25]

Figure 5. Left: Model predictions of chemical species as a function of distance from an Ar/O_2 plasma jet tip. [19] Right: Model predictions of chemical species as a function of distance from an Ar/O_2 plasma jet tip. [19]
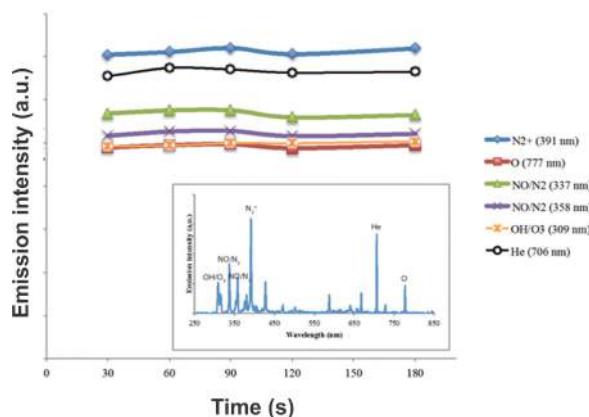
Cold atmospheric plasma devices produce a

Figure 6. Spectral Characterization of He plasma jet [34]

variety of reactive oxygen (ROS) and reactive nitrogen species (RNS) in gas phase, including hydrogen peroxide (H_2), hydroxyl radical (OH^*), hydrogen peroxide (H_2O_2), superoxide (O_2^-), singlet delta oxygen ($O_2 \ a^1\Delta_g$), ozone (O_3), nitric oxide (NO) and peroxynitrite ($ONOO^-$). The major reactions occurring in plasma which create biologically relevant ROS and RNS are shown in figures 3 and 4, respectively. Figure 5 on the left is a plot of measured O and O_3 profiles as a function of distance from the tip of a He/O_2 jet [15]. Figure 5 on the right plots the predicted neutral species as a function of distance from the tip of an Ar/O_2 plasma jet [19].

The effects of RONS produced in cold atmospheric plasma devices are probably indirect: the reactive species created in the gas phase enter the liquid phase and then react with bio-macromolecules (proteins, lipids, carbohydrates, amino acids, etc.) and these relatively stable species are the ones that alter cell signaling processes, modify gene expression, influence immune system response, disrupt cell cycle, induce apoptosis (programmed cell death), and no doubt get involved in other cellular processes.

Figure 7. Viability of three glioma cell lines, A172, U373, and U87 treated with varying durations of cold atmospheric plasma. The cell viability is calculated relative to control [34].

Many of the plasma-produced ROS/RNS are also created in cells and perform biological functions. Endothelial cells produce H_2O_2 and O_2 - at low
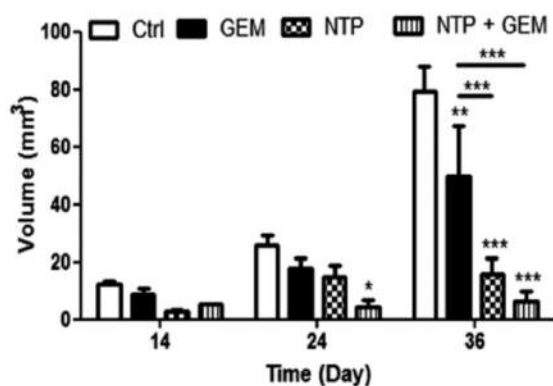
Figure 8. Results indicating the effects of the gemcitabine drug treatment (GEM), application of the plasma (NTP for nonthermal plasma), and the combination of the two treatments on tumor volume in a set of mice. The mice were followed for a maximum of 36 days. The results show promising evidence of a positive additive effect of plasma and drug treatment [26]

concentrations to increase cell proliferation and migration. At low concentrations, H_2O_2 takes part in intracellular signaling while high H_2O_2 concentrations are associated with DNA, lipid and protein damage. Due to its high reactivity, OH^* reacts with many cell components namely DNA, lipids, proteins, amino acids and sugars, leading to loss of cell integrity and function. O_2 $a^1\Delta_g$ produced during inflammation helps fight infection, and it also triggers DNA repair processes. NO promotes cell survival and angiogenesis, both *in vivo* and *in vitro*. ONOO- reacts directly with amino acids such as cysteine, tryptophan and methionine, and NO_2 may take part directly in intracellular signaling [25].

Therefore, it is highly probable that observed success of the cold atmospheric plasma treatment is due to the species common for both air plasma and white blood cells - RONS.

4. Cancer therapy

Probably the most exciting area of plasma medicine is the treatment of cancer. Schlegel *et al.* [22] evidenced that many different types of cancer cells shows sensitivity to plasma treatment. Moreover, it is noticed that cells resistant to radiation and chemotherapy seem especially sensitive to plasma therapy [23, 24]. Most of the studies are done *in vitro*.

Siu *et al.* analysed dose-dependent cold atmospheric plasma treatment effects on the glioma cell lines *in vitro*. The He plasma jet was applied for different time periods, i.e. 60 seconds, 90 seconds, 120 seconds and 180 seconds. The ionized nitrogen species and highly reactive oxygen radicals are present in the spectrum in figure 6, which was stable over time, and consisted largely reactive nitrogen and oxygen species.

The *in vitro* exposure of all three glioma cell lines resulted in a dose-dependent and predictable decline in viability, as shown in figure 7. At maximal treatment duration of 180 seconds, viability decreased to less than 15% compared to control by 24 hours post-treatment for all three cell lines. 60 seconds treatment had only modest effects depending on the cell line (figure 7). The shortest cold atmospheric plasma treatment duration that produced a global decline across all three glioma cell lines was 120 seconds. Cold atmospheric plasma treatment for 90 seconds resulted in sustained decline even at 72 hours post-treatment.

One recent example of an *in vivo* study is the research done by Brulle *et al.* (2012) [26]. These authors tested plasma He jet created in a thin capillary tube in an open air environment. The mice were implanted with human pancreatic cancer cells and the treatment was done alone or with combination with the drug gemcitabine (common pancreatic cancer chemotherapeutic agent). The results of the study are shown in figure 8. The combination of the plasma treatment and chemotherapy seems to be the promising cancer treatment.

5. Concluding remarks

Gas discharge plasmas formed at atmospheric pressure and near room temperature have advanced rapidly and have been applied in a variety of applications with a success. Very promising results are observed ranging from treating infected tissue to shrinking tumors. By now, two cold atmospheric plasma devices have received CE ("CE" stands for the device which conforms to European Union regulations) marking in Germany in 2013 for wound healing applications.

Despite the excellent results, there are still many opened questions regarding the mechanisms relevant in the cold plasma treatment. A better understanding will allow further improvement of the technology and may even offer a new set of applications. The similarity between the chemical agents created in plasma and in the mammalian immune system suggest that the reactive oxygen and nitrogen species created by cold atmospheric plasma are probably central to their effectiveness. This is the point of view taken in this article, but one must keep in mind that the other mechanisms could be important in plasma therapeutics as well. Here we refer to effects of electric field, photons, and charge accumulations.

Assuming the plasma acts by creating and delivering biochemically active chemical species, the question that arises is the uniqueness of plasma. It is possible to create at least some of the species delivered by plasma in some other way. Answer to

this question probably lies in the flexibility and power of plasma technology, but the detailed explanation will require a very close collaboration between plasma specialist, microbiologists, medical researchers and biochemists. Plasma medicine is by now the most important application of the cold atmospheric plasmas and it is expected to develop significantly in years to come.

References

[1] Deng S, Ruan R, Mok C K, Huang G, Lin X and Chen P, 2007, Inactivation of Escherichia coli on almonds using nonthermal plasma, *J. Food Sci.* 72 M626 (2007)

[2] Deilmann M, Halfmann H, Bibinov N, Wunderlich J and Awakowicz P, 2008, Low-pressure microwave plasma sterilization of polyethylene terephthalate bottles, *J. Food Prot.* 71 21 (2008)

[3] Fridman G, Friedman G, Gutsol A, Shekhter A B, Vasilets V N and Fridman A, 2008, Applied plasma medicine, Plasma Process. Polym. 5 50333 (2008)

[4] Moreau M, Orange N and Feuilloley M G J, 2008, Non-thermal plasma technologies: new tools for bio-decontamination, *Biotechnol. Adv.* 26 6107 (2008)

[5] Selcuk M, Oksuz L and Basaran P, 2008, Decontamination of grains and legumes infected with Aspergillus spp. and Penicillum spp. by cold plasma treatment *Bioresour. Technol.* 99 51049 (2008)

[6] Deng X, Shi J J and Kong M G, 2007, Protein destruction by a helium atmospheric pressure glow discharge: capability and mechanisms *J. Appl. Phys.* 101 074701 (2007)

[7] Morrison J C F, 1977, Electrosurgical method and apparatus for initiating an electrical discharge in an inert gas flow US Patent No. 4,040,426 (1977)

[8] Grund K E, 1994, Technology of argon plasma coagulation with particular regard to endoscopic applications Endosc. *Surg. Allied Technol.* 2 717 (1994)

[9] Robotis J, Sechopoulos P, Rokkas Th, 2003, Argon plasma coagulation: Clinical application in gastroenterology", *Ann. Gastroenterol.* 16(2), 131-137 (2003).

[10] Woedtke Th, Reuter S, Masur K, and Weltmann K, 2013, Plasmas for medicine, *Physics Reports*, http://dx.doi.org/10.1016/j.physrep.2013.05.005

[11] Graves D B, 2012, The emerging role of reactive oxygen and reactive nitrogen species in redox biology and some implications for plasma applications to medicine and biology, *J. Phys. D* 45, 263001 (2012).

[12] Emmert S, Brehmer F, Hanble H, Helmke A, Mertens N, Ahmed R, Simon D, Wandke D, Maus-Freidrichs W, Daschlein G, Schon M P, and Viol W, *Clin. Plasma Med.* 1(1), 2429 (2013)

[13] Isbary G, Morfill G, Schmidt H U, Georgi M, Ramath K, Heinlin J, Karrer S, Landthaler M, Shimizu T, Steffes B, Bunk W, Monetti R, Zimmerman J L, Pompl R, and Stolz W, 2010 A first prospective randomized controlled trial to decrease bacterial loads using cold atmospheric argon plasma on chronic wounds in patients, *Br. J. Dermatol.* 163(1), 7882 (2010).

[14] Maisch T, Shimizu T, Li Y F, Heinlin J, Karrer S, Morfill G E, and Zimmerman J L, 2012 Decolonisation of MRSA, S. aureus and E. coli by cold atmospheric plasma using a porcine skin model in vitro, *PLoS One* 7(4), e34610 (2012).

[15] Ellerwig D, Benedikt J, von Keudel A, Knake N, and Schulz-von der Gathen V, 2010, Characterization of the effluent of a He/O 2 microscale atmos- pheric pressure plasma jet by quantitative molecular beam mass spectrometry, *New J. Phys.* 12, 013021 (2010).

[16] Kieft I, van der Laan E, Stoffels E, 2004, Electrical and optical characterization of the plasma needle, *New J. Phys.* 6 (2004) 149.

[17] Stoffels E, Kieft I, Sladek R E J, van den Bedem L J M, van der Laan E P, Steinbuch M, 2006, Plasma needle for in vivo medical treatment: recent developments and perspectives, *Plasma Sources Sci. Technol.* 15 (4) (2006) S169S180.

[18] Laroussi M, Akan T, 2007, Arc-free atmospheric pressure cold plasma jets: a review, *Plasma Process. Polym.* 2007, 4, 777788

[19] S. Zhang, W. van Gaens, B. van Gessel, S. Hofman, E. van Veldhuizen, A. Bogaerts, and P. Bruggeman, Spatially resolved ozone densities and gas temperatures in a time modulated RF driven atmospheric pressure plasma jet: An analysis of the production and destruction mechanisms, J. Phys. D 46, 205202 (2013).

[20] F. Vatansever, W. C. M. A. de Melo, P. Avci, D. Vecchio, M. Sadasivam, A. Gupta, R. Chandran, M. Karimi, N. A. Parizotto, R. Yin, G. P. Tegos, and M. R. Hamblin, Antimicrobial strategies centered around reactive ox- ygen speciesbactericidal antibiotics, photodynamic therapy, and beyond, FEMS Microbiol. Rev. 37(6), 955989 (2013).

[21] C. Wrenger, I. Schettert, and E. Liebau, Oxidative stress in human infec- tious diseasespresent and current knowledge about its druggability, in Drug Discovery, edited by H. El-Shemy (InTech, 2013).

[22] J. Schlegel, J. Koritzer, and V. Boxhammer, Plasma in cancer treatment, Clin. Plasma Med. 1, 27 (2013).

[23] J. Kortizer, V. Boxhammer, A. Sch afer, T. Shimizu, T. G. Kl ampfl, Y.-F. Li, C. Welz, S. Schwenk-Zieger, G. E. Morfill, J. L. Zimmerman, and J. Schlegel, Restoration of sensitivity in chemoresistant glioma cells by cold atmospheric plasma, PLoS One 8(5), e64498 (2013).

[24] Utsumi F, Kajiyama H, Nakamura K, Tanaka H, Mizuno M, Ishikawa K, Kondo H, Kano H, Hori M, and Kikkawa F, 2014, Effect of indi- rect nonequilibrium atmospheric pressure plasma on anti-proliferative ac- tivity against chronic chemo-resistant ovarian cancer cells in vitro and in vivo, *PLoS One* 8(12), e81576 (2014).

[25] Arjunan K P, 2011, PhD thesis: Plasma Produced Reactive Oxygen and Nitrogen Species in Angiogenesis, Drexel University 2011

[26] Brulle L, Vandamme M, Ries D, Martel E, Robert E, Lerondel S, Trichet V, Richard S, Pouvesle J M, and Le Pape A, 2012, Effects of non thermal plasma treatment alone or in combination with gemcitabine in a MIA PaCa2-luc orthotopic pancreatic cancer model, *PLoS One* 7(12), e52653 (2012).

[27] Walk R M, Snyder J A, Srinivasan P, Kirsch J, Diaz S O, Blanco F C, Shashurin A, Keidar M and Sandler A D, 2013, Cold atmospheric plasma for the ablative treatment of neuroblastoma, *J. Pediatric Surg.* 48, 6773 (2013).

[28] Acworth I, 2003, The Handbook of Redox Biochemistry, *ESA Biosciences*, Chelmsford, MA, USA, 2003

[29] Graves D B, 2014, Low temperature plasma biomedicine: A tutorial review, *PHYSICS OF PLASMAS* 21, 080901 (2014)

[30] Kong M G, Kroesen G, Morfill G, Nosenko T, Shimizu T, J. van Dijk J and Zimmermann J L, 2009, Plasma medicine: an introductory review, *New Journal of Physics* 11 (2009) 115012

[31] Stoffels E, Roks A J M, Deelman L E, 2008, Delayed effects of cold atmospheric plasma on vascular cells, *Plasma Processes Polym.* 5 (6) (2008) 599605.

[32] Dobrynin D, Fridman G, Friedman G, Fridman A, 2009,

Physical and biological mechanisms of direct plasma interaction with living tissue, *New J. Phys.* 11 (11) (2009) 115020.

[33] Fridman G, Peddinghaus M, Balasubramanian M, Ayan H, Fridman A, Gutsol A and Brooks A, 2006, Blood coagulation and living tissue sterilization by floating-electrode dielectric barrier discharge in air, *Plasma Chem. Plasma Process.* 26 (4) (2006) 425442.

[34] Siu A, Volotskova O, Cheng X, S. Khalsa S, Bian K, Murad F, Keidar M, Sherman J H, 2015, Differential Effects of Cold Atmospheric Plasma in the Treatment of Malignant Glioma, PLoS One. 10(6):e0126313.

Foundational Review on GMHD - Strong Gravity Effects in Ideal Plasmas

Between music and physics, Rogério pursued the Bachelor and Masters degree in Engineering Physics at IST, the place where he is now in the scope of a joint PhD together with EPFL, Switzerland. This is a continuation of the MSc Thesis work developed at EPFL with the title Simulation of Plasma Blobs in Realistic Tokamak Geometry, a collaboration between IPFN and CRPP. Besides nuclear fusion, his research interests include the study of Meyers-Perry black holes and the physics of music non-linear acoustics.

As an undergraduate student he was awarded a scholarship from the Calouste Gulbenkian program Novos Talentos em Matemática and performed an internship at Laboratório de Instrumentacão e Partículas within the CMS experiment. As a graduate student he was the Vice-President of NFIST, ISTs Engineering Physics Student Association, co-founder of the online education channel portaldasabedoria.pt, and he tutored several undergraduate students in Physics and Mathematics.

Rogério Jorge[1]

[1] Instituto de Plasmas e Fusão Nuclear, Instituto Superior Técnico,Universidade de Lisboa, 1049-001 Lisboa, Portugal

E-mail: `rogerio.jorge@tecnico.ulisboa.pt`

Abstract. A review is done on gravity effects in the dynamics of ideal plasmas, specifically generalizing the ideal MHD equations for a non-flat spacetime. As a first step, the 3+1 formulation of general relativity is applied to the problem of an energy-momentum tensor with a perfect fluid and electromagnetic components coupled to the ideal MHD condition, yielding the GMHD equations that can be numerically solved with different integration techniques. On the second part, we present how spacetime effects can generate vorticity even if the initial magnetic field is set to zero. The new terms can be estimated to give a significant contribution, which can be amplified by known magnetic dynamo mechanisms.

1. Introduction

Nowadays, to improve our understanding of astrophysical processes near compact objects, large-scale three-dimensional simulations provide the most accurate and powerful results (as done in [1], [13] and [6]) to pursue the study of such systems. Together with the numerical solution of the full system of equations, some theoretical understanding has been put out recently on spacetime curvature effects on plasmas ([3], [6] and [14]). This is a difficult job due to the coupled system of time-dependent partial differential equations of gravitomagnetohydrodynamics (GMHD), which describe a perfect fluid, coupled with gravity and electromagnetic interactions.

As black-holes cannot be seen directly, we rely on indirect observations to assert their existence. With enormous gravitational fields, the surrounding plasma will be affected by such objects and so plasma physics problems in the context of general relativity can provide a way to assert the nature of this astrophysical system. Even the final fate of many of these systems may be directly related to the magnetic field generated during their evolution and can be promising sources of gravitational radiation for detection, as pointed in [5]: the merger of binary neutron stars, core collapse in a supernova, the generation of gamma-ray bursts and supermassive star collapse. On a second note, the problem of magnetic field generation is of great interest and also explored in this paper. In the accepted paradigm today, magnetic fields were amplified by some dynamo mechanism from a pre-existing weaker one and the explanation of this cosmological magnetic "seed" is still under devevelopment.

Here, we review the 3+1 formulation of General Relativity in the context of GMHD, presenting the system of equations that can be evolved numerically as cast in [2], [5] and [7] and applied in numerical codes, such as [6]. As the physical mechanisms present are not quite undestood yet, we leave the 3+1 formulation as way to apply different approximations and assess the relevance of each term in the aforementioned description. The magnetic "seed" problem is formulated in the magnetofluid description [8]. We look at the general relativistic version of Maxwell's equations and how to describe the fluid and electromagnetic properties of the plasma in an unified magnetofluid tensor $M^{\mu\nu}$, adding at the end a new vorticity generating term and estimating its magnitude.

2. 3+1 Formulation of General Relativity

2.1. Decomposition of Einstein Field Equations

In this section we shall describe the 3+1 formalism on general relativity. This approach is crucial to understand physical phenomena as seen in 3 space and 1 time dimensions and lies on the basis of modern numerical relativity. As described in [2], it has its origin in the 1920's with the works of Georges Darmois and in the 60's it has served as the foundation of Hamiltonian formulations of general relativity (such as the ADM one). Note that the concept of spacetime doesn't specify *a priori* the number of space or time dimensions, so the constraints we describe constitute a specific formulation of Einstein's field equations that can describe any number of dimensions (coordinates).

As fas as notation goes, greek indices $\mu, \nu, ...$ represent general spacetime coordinates, latin letters a, b, c, d represent 3+1 spacetime coordinates and i, j, k only the 3 space coordinates (usual x, y, z). We start with the Einstein Field Equations (EFE)

$$G_{\mu\nu} = R_{\mu\nu} - \frac{g_{\mu\nu}}{2}R = T_{\mu\nu}, \tag{1}$$

where $G_{\mu\nu}$ is the Einstein tensor, $R_{\mu\nu}/R$ are the Ricci tensor/scalar, $g_{\mu\nu}$ the metric tensor and $T_{\mu\nu}$ the energy-momentum tensor. With the EFE we can find the differential equations that dictate the spacetime curvature $g_{\mu\nu}$ and $T_{\mu\nu}$ has a specific form for each physical situation (fluids, electromagnetic fields, vacuum...). Applying the covariant divergence to Eq. (1) we find the conservation of energy-momentum

$$\nabla_\mu T^{\mu\nu} = 0. \tag{2}$$

Now, given a 4-metric $g_{\mu\nu}$, we want to level our three-dimensional spacetime by a scalar function, which we choose to be the time t. Defining $\Omega_\mu = \nabla_\mu t$ we find the lapse function α such that

$$|\Omega|^2 = g^{\mu\nu}\nabla_\mu t\nabla_\nu t = -\alpha^{-2}, \tag{3}$$

that allows us to define the unit normal vector $n^\mu = -\alpha g^{\mu\nu}\Omega_\nu$ (where $n^\mu n_\mu = -1$) and the spatial metric $\gamma_{\mu\nu} = g_{\mu\nu} + n_\mu n_\nu$. The time vector is given by $t^a = \alpha n^a + \beta^a$, where β^a is called the shift vector. In a coordinate system aligned with t^μ, we have

$$n_\mu = (-\alpha, 0, 0, 0) \text{ and } n^\mu = \alpha^{-1}(1, -\beta^i). \tag{4}$$

These definitions will allow us to decompose any 4 dimensional tensor in its space and time components. The spatial components are found with the spatial projection operator $\gamma_\mu^\nu = \delta_\mu^\nu + n_\nu n^\nu$ and the time ones with the timelike projection operator $N_\mu^\nu = -n^\nu n_\mu$ (and they are orthogonal to each other $\gamma_\mu^\nu N_\nu^\mu = 0$). With this, the 3 dimensional covariant derivative is simply $D_\alpha T_\gamma^\beta = \gamma_\alpha^\rho \gamma_\sigma^\beta \gamma_\delta^\tau \nabla_\rho T_\tau^\sigma$. In the following, we

shall use the concept of extrinsic curvature and Lie derivative. These are defined by

$$K_{\mu\nu} = -\gamma_\mu^\alpha \gamma_\nu^\beta \frac{\nabla_\alpha n_\beta + \nabla_\beta n_\alpha}{2}, \tag{5}$$

$$\pounds_X T_\nu^\mu = X^\alpha D_\alpha T_\nu^\mu - T_\nu^\alpha D_\alpha X^\mu + T_\alpha^\mu D_\nu X^\alpha. \tag{6}$$

The Lie derivative can be thought as a geometrical generalization of a directional derivative and the extrinsic curvature measures the changes in the normal vector under parallel transport. Its trace is given by $K = K_\mu^\mu = -\nabla^\mu n_\mu$. After decomposing the EFE (1) into its spatial and timelike parts, we find the Gauss, Codazzi, Ricci, momentum and Hamiltonian constraint equations (which can be found in [2]). This equations can be numerically integrated with Riemann solvers as in [3] (for a specific GMHD case).

2.2. GMHD in the 3+1 formulation

Although general relativistic magnetohydrodynamics has been subject of treatment for many decades, we can find the first efforts to formulate it in a 3+1 formulation in [4]. When treating ideal plasmas (otherwise called charged fluid), it's energy-momentum tensor is

$$T_{\mu\nu} = hU_\mu U_\nu + pg_{\mu\nu}, \tag{7}$$

including the enthalpy density h, the pressure p and the plasma four-velocity $U_\mu U^\mu = -1$. Recall that an ideal fluid (with isotropic pressure p and mass density ρ) has an energy momentum tensor of $T_{\mu\nu} = (\rho + p)U_\mu U_\nu + pg_{\mu\nu}$. The equations of motion are given by the conservation equation of the energy-momentum tensor that mediate the electromagnetic interactions

$$\nabla^\nu T_{\mu\nu} = qn F_{\mu\nu} U^\nu, \tag{8}$$

where $F_{\mu\nu} = \partial_\mu A_\nu - \partial_\nu A_\mu$ is the electromagnetic field tensor, ∇^ν is the covariant derivative and A_μ the electromagnetic four-potential.

In [5] we can find Maxwell's equations in the 3+1 form, by decomposing the EM tensor as $F_{\mu\nu} = n_\mu E_\nu - n_\nu E_\mu + \epsilon_{\mu\nu\delta} B^\delta$, the electromagnetic four-current $J_\mu = n_\mu \rho_e + \bar{J}_\mu$, where $\rho_e / \bar{J}_\mu$ is the charge density/current, Maxwell's equations in tensor form are simply

$$\nabla_\mu F^{\mu\nu} = 4\pi J^\nu, \tag{9}$$

which can also be decomposed in 3+1 form after introducing the electromagnetic vector potential $A_\mu = (\phi, \vec{A})$ (with the usual $B^\mu = \epsilon^{\mu\nu\delta} A_\delta$) and the determinant γ of the spatial metric γ_{ij} yields (with $\pounds_\beta$ the Lie derivative along the shift vector β)

$$\left. \frac{\partial \vec{E}}{\partial t} \right|_i = \frac{1}{\sqrt{\gamma}} \frac{\partial}{\partial x^j} \left[\alpha\sqrt{\gamma}(\gamma^{il}\gamma^{jm} \right.$$
$$\left. - \gamma^{im}\gamma^{jl}) \frac{\partial A_m}{\partial x^l} \right] - 4\pi\alpha\vec{J} + \alpha K\vec{E} + \pounds_\beta \vec{E}, \tag{10}$$

$$\frac{\partial \vec{A}}{\partial t} = -\alpha\vec{E} - \nabla(\alpha\phi) + \pounds\vec{A}. \tag{11}$$

To derive the ideal MHD formula, we start by Ohm's law (as seen, e.g., in Jackson's "Classical Electrodynamics", problem 11.16) and, dividing it by the conductivity and letting it $\to \infty$ yields the perfect conductivity condition $U_\mu F^{\mu\nu} = 0$. This result implies that the electric field in the fluid rest frame vanishes $U_\mu E^\mu = 0$ which is the same as (with v^j the fluid velocity vector)

$$\alpha E_i = -\epsilon_{ijk}(v^j + \beta^j)B^k. \tag{12}$$

which is the ideal MHD relation in this case. The equation above, combined with the trace of Faraday's law and defining the magnetic vector density $\vec{\mathcal{B}} = \sqrt{\gamma}\vec{B}$ yields

$$\frac{\partial \mathcal{B}^i}{\partial t} = \frac{\partial}{\partial x^j}\left(v^i \mathcal{B}^j - v^j \mathcal{B}^i\right) \text{ and } \nabla \cdot \vec{\mathcal{B}} = 0. \tag{13}$$

Lastly, we have to take into account the fluid characteristics of our system. For a perfect fluid, the energy momentum tensor reads as in Eq. (7). The equation of motion (8) can be cast in multiple forms and, following [5] (and usual notation on general relativistic hydrodynamics papers) we define for a rest-mass density ρ_0, a rest-mass density variable $D \equiv \rho_0 W$, an internal energy density variable $E \equiv \rho_0 \epsilon W$, a momentum variable $S_\mu = \rho_0 h W U_\mu = (D+E+PW)u_\mu$ and W can be found from the normalization of $U^\mu U_\mu = -1$ as $W = \alpha U^t = (1+\gamma^{ij}U_i U_j)^{1/2}$ and $v^i = \frac{\alpha\gamma^{ij}U_j}{W} - \beta^i$ (with U^t the temporal part of U). The final set of equations contain the Euler equation

$$\frac{1}{\sqrt{\gamma}}\frac{\partial}{\partial t}(\sqrt{\gamma}S_i) + \frac{1}{\sqrt{\gamma}}\nabla\cdot(\sqrt{\gamma}S_i\vec{v})$$
$$= -\alpha\frac{\partial P}{\partial x^i} + \frac{S_a S_b}{2S_t}\frac{\partial g^{ab}}{\partial x^i} + \alpha\frac{E_i}{4\pi}D_k E^k - \frac{\mathcal{B}_i}{4\pi}. \tag{14}$$

where

$$\mathcal{B}_i = B^j\left[\epsilon_{ijk}\left(\frac{\partial E^k}{\partial t} - \vec{\beta}\cdot\nabla E^k + \vec{E}\right.\right.$$
$$\left.\left.\cdot\nabla\beta^k - \alpha K E^k\right) + \frac{\partial}{\partial x^i}\alpha B_j - \frac{\partial}{\partial x^j}\alpha B_i\right]. \tag{15}$$

The same authors in [5] note that in the Newtonian limit and cartesian coordinates, $\gamma = 1$, $g_{00} = -(1 + 2\phi)$ (where ϕ is the gravitational potential) we have the usual equation for conservation of momentum in ideal MHD

$$\rho\frac{d\vec{v}}{dt} = -\nabla(P + B^2/8\pi) - \rho\nabla\phi + \frac{1}{4\pi}(\vec{B}\cdot\nabla)\vec{B} + \rho_e\vec{E}. \tag{16}$$

To study the motion of the plasma in the ideal MHD limit we can assign a background metric $g_{\mu\nu}$ and, to study the backreaction effects on the spacetime metric, we need to rely on modern numerical relativity. An application of these equations to Bondi-Hoyle accretion can be found in [13].

2.3. Schwarzschild Dispersion Relation

In [7] we can find the linearization of the GMHD equations near a Schwarzschild black hole for a two-fluid plasma, comprised of electrons and ions (or positrons). As the Schwarzschild metric is the simplest solution in general relativity (for a spherical mass with no electric charge, angular momentum nor cosmological constant), it is useful for describing many stars, planets and black holes and the simplest way to extract gravitational corrections to the classical formulas. The metric tensor in this case is given by

$$ds^2 = -\alpha^2 + \frac{dr^2}{\alpha^2} + r^2(d\theta^2 \ \sin^2\theta d\phi^2) \tag{17}$$

$$\alpha^2 \equiv \frac{d\tau}{dt} = 1 - \frac{2M}{r}. \tag{18}$$

Also, the gravitational acceleration measured by an observer at rest is $\vec{a} = -\nabla \ln \alpha = -\frac{M}{\alpha r^2}\hat{e}_r$ and the convective derivative is $\frac{D}{D\tau} \equiv \frac{\partial_t}{\alpha} + \vec{v} \cdot \nabla$.

The derivation of the 2 fluid equations is done in 3+1 notation, with the energy-momentum tensor the perfect fluid one with the electromagnetic. After reducing them to one dimensional wave propagation, the linearization procedure takes place on a Rindler coordinate system (locally Cartesian) and introduces a linear perturbation on the species velocity (and Lorentz factor γ), mass density, pressure (and hence temperature), charge density and to the electric and magnetic fields. All the values are expressed in terms of the freefall velocity $v_{ff} = \sqrt{1 - \alpha^2}$ and a local approximation on $\alpha^2 \ll 1$ is done. The resulting dispersion relation is then (see [7])

$$K_\pm \left(K_\pm \pm \frac{i}{r_H} \right) - \omega^2 + \frac{1}{4r_H^2}$$
$$= \alpha_0^2 \left[\frac{\omega_{p1}^2(\omega - u_{01}K_\pm)}{u_{01}K_\mp - \omega - \alpha_0\omega_{c1}} + \frac{\omega_{p1}^2(\omega - u_{02}K_\pm)}{u_{02}K_\mp - \omega - \alpha_0\omega_{c2}} \right], \tag{19}$$

where, for the species s, $\omega_{cs} = e\gamma_{0s}n_{0s}\frac{B_{0s}}{\rho_{0s}}$, $K_\pm = \alpha_0 k \pm \frac{i}{2r_H}$, α_0 is the mean-field value of α and r_H is the horizon radius. A numerical implementation and discussion of results is also performed on [7].

3. Generation of Primordial Magnetic Fields

3.1. Magnetofluid Unification Equations

In the previous section, we presented the 3+1 model of gravitational MHD in the ideal limit. This prescription is suited to implement numerical codes in order to solve the equations of motion but, in order to perform an analytical study on the magnetic field generation we shall use the formalism described in [8] - the Magnetofluid formalism. Defining the auxiliary thermodynamic function

$$f = f(T) = \frac{h}{mn}, \tag{20}$$

that for a Maxwellian function reads $\frac{K_3(m/T)}{K_2(m/T)}$, where K_i is the modified Bessel function of the second kind, T the temperature and the fully antisymmetric second-rank "flow" tensor

$$S_{\mu\nu} = \nabla_\mu(fU_\nu) - \nabla_\nu(fU_\mu), \tag{21}$$

we can rewrite the equation of motion (8) using the magnetofluid field $M_{\mu\nu} = F_{\mu\nu} + \frac{m}{q}S_{\mu\nu}$ and the entropy density σ from $\nabla_\mu\sigma = \frac{\nabla_\mu p}{nT} - m\frac{\nabla_\mu f}{T}$ as

$$qu^\nu M_{\mu\nu} = T\nabla_\mu\sigma. \tag{22}$$

Just to make sure that the equations agree on the non-relativistic limit with the usual ones, using a flat Minkowski spacetime where $\nabla_\mu \to \partial_\mu$, $\gamma \simeq 1 + v^2/2$, and for $f \simeq 1$ (which neglects spatial temperature variations), the equation of motion (22) reduces to Eq. (16), which is the standard equation of motion for a non-relativistic ideal plasma. This has introduced corrections to the Newtonian formula $-r^2p'(r) = GM(r)\rho(r)$ and has used the same energy-momentum tensor (7) to obtain the differential equations. The formalism described in this paper introduces the additional equation of motion (8), i.e., electromagnetic effects.

In the case of a fluid with constant $\sigma = \ln\left[\frac{p}{K_2}\left(\frac{m}{T}\right)^2 e^{-\frac{m}{T}\frac{K_3}{K_2}}\right]$ (which is purely fluid (thermal) dependent quantity), the equation of motion is $u_\mu M^{\mu\nu} = 0$. Recall that $U_\mu F^{\mu\nu}$ is the expression for the electromagnetic force, which as pointed by [8], tells us that the unification of the flow field and the electromagnetic field exert no net force on the fluid. We note that the presence of EM effects is mediated by the substitution

$$S^{\mu\nu} \to S^{\mu\nu} + \frac{q}{m}F^{\mu\nu} \text{ and } fU^\nu \to fU^\nu + \frac{q}{m}A^\nu. \tag{23}$$

The term unification comes from the analogy with the minimal coupling description to insert the EM effects in particle dynamics $mu^\nu \to mu^\nu + qA^\nu$. In the low temperature regime f tends to unity and we recover the minimal coupling prescription.

3.2. Magnetic Field Generation

We will present two derivations, in the context of the magnetofluid unification formalism, for the generation of magnetic fields from a zero initial value. The first one, described in [9], just uses Eq. (22) and presents its vector part in Minkowski spacetime as

$$q\left[\hat{\mathbf{E}} + \mathbf{u} \times \hat{\mathbf{B}}\right] = \frac{cT}{\gamma}\nabla\sigma. \tag{24}$$

Here, the generalized electric field $\hat{E}^j = E^j + \frac{m}{q}S^{0j}$ satisfies Faraday's law $\frac{\partial \hat{\mathbf{B}}}{\partial t} = -\nabla \times \hat{\mathbf{E}}$. Taking the curl of Eq. (24), we find the source for magnetic field $\hat{\mathbf{B}} = \mathbf{B} + \frac{m}{q}\nabla \times (f\gamma\mathbf{v})$ generation, that can be broken in the familiar baroclinic term plus the relativistic induced new term

$$\frac{\partial \hat{\mathbf{B}}}{\partial t} - \nabla \times (\mathbf{v} \times \hat{\mathbf{B}}) = \mathbf{\Omega}_B + \mathbf{\Omega}_R$$
$$= -\frac{1}{q\gamma}\nabla T \times \nabla\sigma - \frac{\gamma T}{2q}\nabla u^2 \times \nabla\sigma. \tag{25}$$

We can estimate the ratio of these two terms as $\frac{|\mathbf{\Omega}_R|}{|\mathbf{\Omega}_B|} \sim \frac{(v/c)^2}{1-(v/c)^2}$, which tells us that for highly relativistic flows (or even for any universal phenomena with $\nabla T = $ or $\neq 0$) $\mathbf{\Omega}_R$ is dominant.

In order to work out the effects of spacetime curvature on magnetic field generation, we follow [10] and express the metric tensor $g_{\mu\nu}$ with the coefficients α, β_i and γ_{ij} as

$$ds^2 = -\alpha^2 dt^2 + \gamma_{ij}(dx^i + \beta^i dt)(dx^j + \beta^j dt). \tag{26}$$

In this reference, the authors study spacetimes where the shift vector $\vec{\beta}$ can be consistently put to zero, using the rest frame of our system. The same definitions (4) are still valid, but with $\vec{\beta} = 0$. The four-velocity is $u^\mu = (\gamma, \gamma\vec{v})$ and, since $n_\mu u^\mu = \alpha\gamma$, the decomposition $u^\mu = -\alpha\gamma n^\mu + \gamma\gamma^\mu_\nu v^\nu$ yields the Lorentz factor expression

$$\gamma = \left(\alpha^2 - \gamma_{\mu\nu}v^\mu v^\nu\right)^{-1/2}. \tag{27}$$

If the shift vector would be not zero we would have $\gamma = \left[\alpha^2 - \gamma_{ij}(\beta^i\beta^j + 2\beta^i v^j + v^i v^j)\right]^{-1/2}$. In this framework, Maxwell's equations (9) in the general relativity limit with no shift vector have the simplified form (see [10])

$$\nabla \cdot \vec{E} = 4\pi q n\alpha\gamma, \tag{28}$$

$$\nabla \times (\alpha\vec{B}) = 4\pi q n\alpha\gamma\vec{v} + \frac{\partial\vec{E}}{\partial t}, \tag{29}$$

$$\nabla \cdot \vec{B} = 0, \tag{30}$$

$$\nabla \times (\alpha\vec{E}) = -\frac{\partial\vec{B}}{\partial t}. \tag{31}$$

Now, in the magnetofluid formulation, we decompose in the same manner the tensor $M^{\mu\nu}$ with the generalized electric field $e^\mu = n_\nu M^{\mu\nu}$ and magnetic field $b^\mu = \frac{n_\rho}{2}\epsilon^{\rho\mu\sigma\tau}M_{\sigma\tau}$. We can now rewrite the magnetofluid tensor as $M^{\mu\nu} = e^\mu n^\nu - e^\nu n^\mu - \epsilon^{\mu\nu\rho\sigma}b_\rho n_\sigma$ and obtain the explicit expressions

$$\vec{e} = \vec{E} - \frac{m}{\alpha q}\nabla(f\alpha^2\gamma) - \frac{m}{\alpha q}\frac{\partial}{\partial t}(f\gamma\vec{v}), \tag{32}$$

$$\vec{b} = \vec{B} + \frac{m}{q}\nabla \times (f\gamma\vec{v}). \tag{33}$$

The spacelike projection of the equation of motion (22) with γ^β_μ yields the momentum evolution equation $\alpha\gamma\vec{e} + \gamma\vec{v} \times \vec{b} = \frac{T}{q}\nabla\sigma$. Using the antisimmetry of the unified tensor $M^{\mu\nu}$ we can arrive to the vorticity equation, recognizing the baroclinic term Ω_B from Eq. (25) and the generalization of the relativistic term as $\Omega_R = \frac{T}{q\gamma^2}\nabla\gamma \times \nabla\sigma = \frac{T\gamma}{2q}[-\nabla\alpha^2 + \nabla(\gamma_{ij}v^i v^j)] \times \nabla\sigma$. In it's full form we can write the general vorticity equation

$$\frac{\partial\vec{b}}{\partial t} - \nabla \times (\vec{v} \times \vec{b}) = \Omega_B + \Omega_R. \tag{34}$$

In the same work [10] it is found also an estimate for the magnetic field seed generated in gauss for a test plasma matter accreting at a distance of $5r_0$ of a black hole of stellar mass as $|\Omega_R| \sim 5 \times 10^{-6}G$ which, at this strong gravity and/or relativistic regimes contributes much more than the baroclinic term.

4. Conclusion

We have presented the GMHD system of equations in a form suited for numerical studies and can be used for the study of a wide range of processes (static background, gravity-plasma backreaction). On the second part of the paper we have adressed the problem of magnetic "seed" created by the interaction between gravity and inhomogeneous plasma thermodynamics. These seeds can be amplified by, for example, Parker's mechanism or the *shearing* of the magnetic field. This mechanism has been applied to spacetimes with no shift vector, but further studies need to be done more general metrics, like rotating black holes (Kerr metric) or in more sophisticated intricate cosmological models, with and without (as [11]) minimal coupling. From a different point of view, the GMHD dynamics can be seen from conservation laws [12] and can even be applied to the case of resistive MHD [14].

References

[1] K. Nishikawa, *The Astr. Jour.*, **625** 1 (2005)
[2] É. Gourgoulhon, arxiv:0703035 (2007)
[3] L. Antn et. al, *The Astr. Jour.*, **637** 296-312 (2006)
[4] Xiao-He Zhang, *Phys. Rev. D*, **39** 10 (1989)
[5] T. Baumgarte et. al, *The Astr. Jour.*, **585** 921-929 (2003)

[6] P. M'osta et. al, *Clas. Quantum Grav.*, **31** 015005 (2014)

[7] V. Buzzi et. al, *Phys. Rev. D*, **51** 12 (1995)

[8] S. Mahajan, *Phys. Rev. Lett.*, **90** 3 (2003)

[9] S. Mahajan et. al, *Phys. Rev. Lett.*, **105** 095005 (2010)

[10] F. Asenjo et. al, *Phys. Plasmas*, **20** 022901 (2013)

[11] C. Bhattacharjee et. al, arxiv:1410.7732v2 (2015)

[12] J. Bekenstein et al, *Phys. Rev. D*, **18** 6 (1978)

[13] A. Penner, *Mon. Not. R. Astron. Soc.*, **414** 1467-1482 (2011)

[14] K. Dionysopoulou, *Phys. Rev. D*, **88** 044020 (2013)

Review of Ultracold Neutral Plasmas

Rolando is from La Paz, Bolivia. He obtained a Bachelor degree in Physics at Mayor de San Andrs University in La Paz with the research paper called Study of the solution of the Schrdinger equation for an unharmonic potential well using the Numerov method.

As an undergraduate student, he became a teacher assistant for various subjects in theoretical physics and math applied to physics. He also worked as a tutor in physics and mathematics for high school and college students and was part of several Physics fairs organized for the public by the Physics department of the Mayor de San Andrs University.

After graduating, he was granted a scholarship from the Swedish government to continue his studies at Ume University in Northern Sweden. His main field of study was computational physics. After two years of study he obtained a MSc. in Physics with his research in plasma physics. The title of his Masters thesis was Cyclotron damping in Magnetized Plasmas.

Rolando Ayllon

Instituto de Plasmas e Fusão Nuclear, Instituto Superior Técnico, 1049-001 Lisboa, Portugal

E-mail: `rsalinas@ipfn.ist.utl.pt`

September 2015

Abstract. Photoionization of samples of laser-cooled atoms has allowed the creation of ultracold neutral plasmas. They represent a new frontier in the study of neutral plasmas, this new kind of plasma blur the boundaries of plasma, atomic, condensed matter, and low temperature physics. This document describes some of the main topics of research in the area of ultracold neutral plasmas. We have made a description of the process to create the plasma in this range. Since ultracold plasmas are not confined, experimentally it was observed a rapid expansion of the plasma, the expanding plasma is a complex dynamic system who has attracted the attention of researchers. Another observed phenomena in these plasmas was the recombination of the plasma into Rydberg atoms even at very low plasma densities. Finally, because the expansion will have an impact on the temperature of the plasma, it is important to be able to measure the temperature. For that reason develop new techniques to measure the temperature in this plasmas has become important research topic.

1. Introduction

In plasma physics, high temperatures are needed to sustain ionization. The electron temperature defines the scale, and the temperature is a defining feature of the plasma. However, in the recent years has been introduced a new domain of plasma physics where the mentioned requirement of high temperatures are not more fullfiled. This new branch is known as ultracold neutral plasmas.

Ultracold neutral plasmas are formed by photoionizing laser-cooled atoms near the ionization threshold and the range of electron temperature are from 1 to 1000 K and ion temperatures of around 1 K. These plasmas can be in or near the strongly coupled regime. The strongly coupled regime become an interesting research area because many of the classical plasma assumptions are not longer valid. The strong-coupling regime for electrons is characterizedby the dimensionless Coulomb coupling parameter

$$\Gamma = \left(\frac{e^2}{4\pi\epsilon_0 a} \right) \frac{1}{k_B T}, \tag{1}$$

where e is the electron charge, k_B is the Boltzmann constant, and a is the Wigner-Seitz radius $a = (3/4\pi n)^{1/3}$.

Strongly coupled plasmas exist in dense astrophysical systems, matter irradiated with intense laser fields, colloidal or dusty plasmas of highly charged macroscopic particles, and non-neutral trapped ion plasmas that are laser cooled until they freeze into an arrange that minimizes the potential energy known as Wigner crystals.

Recombination of electrons and ions to form neutral atoms is a fundamental process in plasma physics. At typical plasma temperatures of 1000 K or higher, radiative recombination (RR), dielectronic recombination (DR), and three-body recombination (TBR) are the dominant processes. Lowering the temperature, TBR becomes dominant compared to RR and DR, since this kind of recombination scales as $T^{-9/2}$. Understanding of this process is of importance to possible creation of anti-hydrogen through recombination of positron and anti-proton. Also, experimental evidence of formation of Rydberg atoms [1], due TBR has been observed in ultracold neutral plasma, and the inverse process, this is spontaneous evolution of a cold gas of Rydberg atoms into a plasma, also has been reported [2].

2. Creation of Ultracold Neutral Plasmas

The first ultracold plasma experiments were performed at the National Institute of Standards and Technology in Gaithersburg (NIST). The creation of ultra-cold plasmas are described in [3]. The production starts
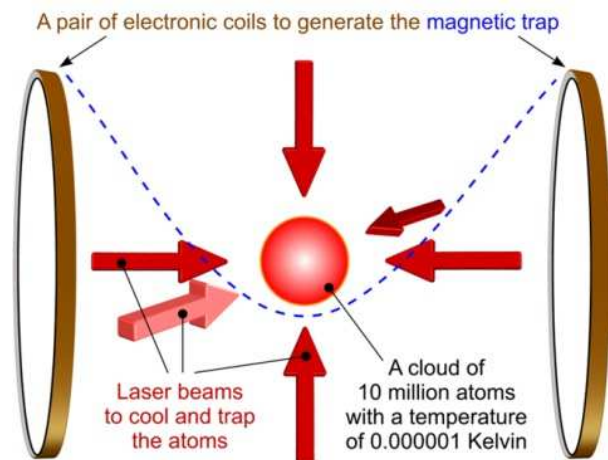

Figure 1. Schematic setup of a typical ultracold plasma experiment, using strontium atoms.

with laser-cooled and trapped neutral atoms in a magnetic optical trap (MOT)‡. In Figure 1, there is the schematic configuration of the MOT. The most common used atoms to be cooled down in a MOT are Xenon [3, 4, 5, 6], Strontium [7, 8], calcium [9] and Rubidium [10, 11] to typical densities of $10^9\,\text{cm}^{-3}$ and temperatures near $10\,\mu\text{K}$.

A pulsed dye laser excites the laser-cooled atoms above the ionization threshold. Because of their light mass, the electrons have an initial kinetic energy E_e approximately equal to the difference between the photon energy and the ionization potential. The temperature E_e/k_B can be as low as the bandwidth of the ionizing laser, which is $\sim 100\,\text{mK}$ with standard pulsed dye lasers. But most studies so far have dealt with temperatures between 1 and 1000 K.

Most ultracold plasma experiments have used two-photon ionization, in which one photon from the continuous-wave (CW) cooling laser excites atoms to the upper level of the cooling transition, and a pulsed laser then excites them to the continuum. The excited-state fraction during normal MOT operation is typically about 10%, but an extra excitation beam may also be used to reach up to 50%. Highly saturating the transition with a pulsed-dye-amplified beam yields have been proved to give better results [9].

Immediately after the photoionization, the electrons are monoenergetic, with a kinetic energy given by the excess energy of the ionizing photon above the ionization limit. The electrons carry off almost all of this excess of energy and the ions receive very little of

‡ A MOT uses an arrangement of laser beams close to the resonance frequency of the atom in order to slow down the neutral atoms. And the magnetic field affects the resonance frequencies of the atom, so that the laser photons push the atoms as if they were attached to the trap center by a spring.
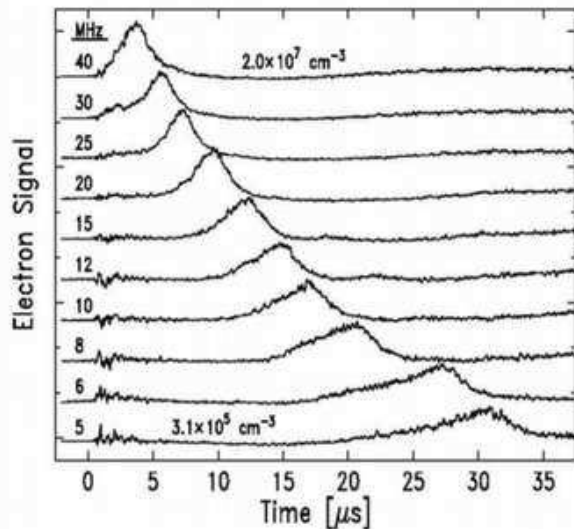
Figure 2. Plasma response to applied RF fields.The applied RF frequency (MHz) is shown on the left [5].

Figure 3. The asymptotic expansion velocity of the plasma as a function of the initial energy imparted to the electrons by the photoionization [5].

it. This is due to the large ratio in masses between the ions and electrons. The ions will only gain 4×10^6 of the initial energy, remaining in the sub-mK temperature range. This means the ions can be considered to be essentially stationary at short timescales. As the electrons thermalize, some of them scape from the cloud. This creates a residual positively charged cloud, which begins to act as an attractive potential for the remaining electrons. This process will continue until the potential is as deep as the temperature of the electrons, at which point they are trapped, forming a neutral plasma.

3. Plasma Expansion

The electrons are trapped by the field produced by the ions, this kind of plasma is not confined so it will expand due to the electron pressure. The dynamics of the expanding plasma has been reason of study, experimentally [1, 4] and theoretical [12].

The expansion rate was measured by observing the response of the plasma to an RF electric field [5, 4]. The plasma oscillation is independent of the temperature, but depends on the electron density. When the density of the plasma was such that a large fraction of the plasma could be excited by the RF coupling to this plasma mode, energy was pumped in and electrons were boiled off. These electrons then appeared as a peak in detected electron current at a certain time after plasma creation Figure 2. By interpreting the time of the peak of this response as the time when the plasma had the average density corresponding to the density that would be resonant wi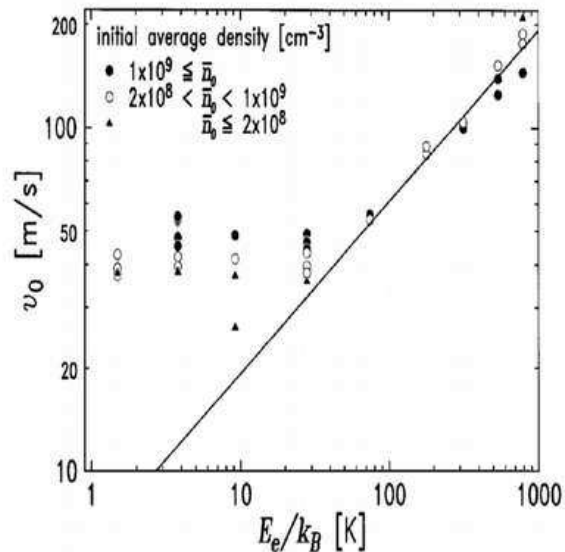th the applied RF drive, it is possible to extract the density vs. expansion time, this is the plasma expansion rate Figure 3.

If we imagine the electrons oscillating in the Coulomb potential created by the excess ions, whenever an electron is turned around by the potential it exerts a force on the ions, leading to an outward expansion of the ions. It should be emphasized that this increase in ion velocity does not correspond to an increase in the ion temperature, as it represents a coherent expansion. The ion temperature can still be cold. This rapid expansion has been successfully modeled with a Fokker- Planck treatment [13] as well as molecular dynamics simulations [14].

4. Rydber atoms formation

Kulin et al. [5], found that there was an anomalous excess expansion velocity at low temperatures that could not be explained by electron pressure Figure 3. This might seem troubling because it would imply there was more energy in expansion than had been supplied by the photons doing the ionization. Of course energy conservation must hold, which means there must also be present a source of negative energy. In an experiment performed by Killian [1], looking for the formation of Rydberg atoms § in ultracold neutral plasmas. These Rydberg atoms were detected by using selective field ionization after the plasma was created. It was found that as much as 30% of the plasma

§ Rydberg atoms are atoms with valence electrons in states of very large principal quantum number.

recombines into Rydberg atoms and viceversa [15].

An examination of the possible recombination mechanisms rules out all processes at low temperatures except three-body recombination, which is predicted to scale as $T^{-9/2}$ [16] and could be quite large at low temperatures. In three-body recombination (TBR), an electron and an ion recombine to form a highly excited Rydberg atom, while a second electron participates in the collision to conserve energy and momentum. TBR is an important process in ultracold neutral plasma, in contrast to conventional plasmas where this process is only in dense plasmas. At low densities, recombination typically proceeds by radiative recombination and dielectric recombination.

The classical three-body recombination theory, which is not questioned for high-temperature plasmas, predicts a total recombination rate per ion of

$$K_{tbr}^{(tot)} \approx 3.8 \times 10^{-9} T_e^{-9/2} \rho_e^2 \quad [\text{s}^{-1}], \tag{2}$$

where T_e is given in K and the density ρ is in cm^{-3}. For typical parameters of $T_e = 9\,\text{K}$ and $\rho_e = 3 \times 10^9\,\text{cm}^{-1}$ this yields an extremely large recombination rate of $K_{tbr}^{tot} \approx 10^6\,\text{s}^{-1}$. Hence, one would expect the plasma to almost completely convert into a Rydberg gas within a few microseconds. Contrary to this, only a few percent of recombination is observed after $12\,\mu\text{s}$ for the above initial conditions.

The last evidence has motivated investigations into whether TBR theory must be modified in the ultracold regime. In addition to the fundamental interest in TBR at low temperatures, the process is important in the formation of cold antihydrogen through positron-antiproton recombination. In ion storage rings, collisions between ions and electrons in electron coolers can be in the 10 to 100 K energy range, and anomalously large recombination rates have been observed for highly charged ions.

5. Temperature mesurements

Once the plasma is created at a particular temperature, that temperature is not expected to remain constant as the dynamics during its expansion will also have a great impact. As the plasma expands, the electron thermal energy is converted into ion expansion velocity, resulting in strong adiabatic cooling of the electron cloud. In addition, it was observed electrons leaking out of the plasma after the initial burst that escapes when the initial confinement and charge imbalance occurs during formation, and this results in evaporating cooling [17].

These cooling mechanisms are in competition with the heating due to three-body recombination. Because of the strong inverse temperature dependence, we would expect the recombination will try to act as a temperature moderator in any circumstance where a

significant number of electrons recombine. Any cold plasma will have a fast recombination rate that will then in turn heat the plasma.

Measuring the temperature of such an ultracold plasma is a challenge, as its transient nature and the low temperatures means that invasive physical probes such as used with traditional plasmas will not work. One possible avenue that has been used in plasma physics is to measure the ion acoustic velocity which is proportional to $T_e^{1/2}$. There is evidence for ion acoustic waves under various parameters, where it was observed multiple peaks in the response of the plasma to the RF field that excites plasma oscillations. The interpretation of these peaks as ripples in the density profile is due to the excitation of ion acoustic waves at the plasma formation [4]. Such waves have also been seen in theory simulations [13]. The problem with using them as a measure of the temperature is that these waves are traveling on a expanding density profile that is expanding with essentially the same velocity as the acoustic wave. This along with the inhomogeneous density profile makes any simple analysis impossible.

The most common diagnostic for studying ultracold plasmas is detection of charged particles after they have left the plasma. The initial experiments at NIST on plasmas produced by direct photoionization detected electrons as source of measurement [5, 17]. Experiments exploring the spontaneous evolution of Rydberg atoms into a plasma [15] and dynamics of Rydberg atoms embedded in an ultracold plasma [18, 19] have used both ion and electron detection. For monitoring electrons that escape the plasma during normal evolution, an electric field is required to guide them to the detector. However, the field must be less than about $5\,\text{mV/cm}$ to avoid perturbing the plasma. This produces a time-of-flight delay for electrons until they reach the detector on the order of $1\,\mu\text{s}$. In addition, at such low fields the detection efficiency is not 100%. The electric field can easily be ramped to much larger values that can quickly dump all charged particles of a given sign on the detector. With careful design, values well in excess of $100\,\text{V/cm}$ can be obtained, which are also useful for pulsed field ionization of Rydberg atoms [20].

Another techniques were proposed by Simien et al. [8] and McQuillen[21] et al. using optical approaches. Simien in his work used an adaptation of absorption imaging, which is one of the most powerful techniques for studying laser cooled and trapped neutral atoms. McQuillen in his work, used spatially resolved fluorescence spectroscopy to measure ion temperature evolution during the expansion of an UNP. Implementation of these probes to study ultracold plasmas requires much higher temporal resolution than typically needed for neutral atom

experiments because the plasma evolves quickly, i.e. be in the range of nanoseconds in some cases.

To record an absorption image of the plasma, a collimated laser beam tuned near resonance with the principal transition in the ions illuminates the plasma and falls on an image-intensified CCD camera. Ions scatter photons out of the laser beam and create a shadow that is recorded by the camera. The experimentally measured optical depth is defined in terms of the image intensity without the plasma and with the plasma present. By varying the delay between the formation of the plasma and image exposure, the time evolution of the plasma can be studied. The minimum camera exposure gate width for standard intensified CCD cameras is 10 ns. Valuable information is provided by the absorption spectrum, which can be recorded by varying the frequency of the probe beam.

6. Future work

The study of ultracold neutral plasmas are both interesting and challenging, experimentally and theoretically. At the moment we do not have a viable temperature measurement technique in this region. While techniques exist to study electron temperature at later times, at present there is no experimental diagnostic to cleanly explore the electron equilibration phase because electrons evolve so quickly. The development of such diagnostic will be a significant advance.

Exactly what is happening at long times is clearly one of the outstanding questions. Whether the plasma is becoming strongly-coupled and what the mechanism for atom formation is at long times are unknown. Proposals of using molecular dynamics simulations to answer some of these questions have been made, but this problem is exceedingly demanding on such techniques due to the wide range of relevant timescales in the computation. To correctly model the electron motion including such things as capture into Rydberg states requires time steps in the fs - ps range. But to model the expansion requires timescales in the 10 to 100 µs timescales. Coupled with the need for a sufficient number of particles to get a good ensemble average makes the computational demands extreme, beyond current capabilities. That is why the study of this systems with PIC simulations or hybrid methods has attracted the attention of group of research. Since these methods, can reduce the computational effort.

As the field grows, there is great possibility to increase the connection to traditional areas of plasma physics. The role of strong coupling and the equilibration and expansion dynamics partly resemble the behavior of laser-produced plasmas in high energy density experiments. The slower time scales, excellent diagnostics, and control over initial conditions in ultracold plasmas provide unique opportunities to make significant contributions to these other areas.

The recent production of cold Rydberg gases and plasmas in strong magnetic fields of several Teslas [22, 23] has opened up a new regime where the atomic scale and macroscopic system dynamics is fundamentally different from the field-free situation. Theory has just started to treat collisional [24, 25, 26] and radiative [27, 28] processes under such conditions, while the macroscopic dynamics of magnetized ultracold µm-scale neutral plasmas still awaits a deeper understanding. This will help to continue studies of cold antihydrogen atoms.

References

[1] Killian T C, Lim M J, Kulin S, Dumke R, Bergeson S D and Rolston S L 2001 *Phys. Rev. Lett.* **86** 3759

[2] Robinson M P, Tolra B L, Noel M W, Gallagher T F and Pillet P 2000 *Phys. Rev. Lett.* **85** 4466

[3] Killian T C, Kulin S, Bergeson S D, Orozco L A, Orzel C and Rolston S L 1999 *Phys. Rev. Lett.* **83** 4776

[4] Fletcher R S, Zhang X L and Rolston S L 2006 *Phys. Rev. Lett.* **96** 105003

[5] Kulin S, Killian T C, Bergeson S D and Rolston S L 2006 *Phys. Rev. Lett.* **85** 318

[6] Zhang X L, Fletcher R S and Rolston S L 2008 *Phys. Rev. Lett.* **100** 235002

[7] Chen Y C, Simien C E, Laha S, Gupta P, Martinez Y N, Mickelson P G, Nagel S B and Killian T C 2004 *Phys. Rev. Lett.* **93** 265003

[8] Simien C E, Chen Y C, Gupta P, Laha S, Martinez Y N, Mickelson P G, Nagel S B and Killian T C 2004 *Phys. Rev. Lett.* **92** 143001

[9] Cummings E, Daily J, Durfee D and Bergeson S 2005 *Phys. Rev. Lett.* **95** 235001

[10] Choi J, Knuffman B, Zhang X H, Povilus A P and Raithel G 2008 *Phys. Rev. Lett.* **100** 175002

[11] Tanner P J, Han J, Shuman E S and Gallagher T F 2008 *Phys. Rev. Lett.* **100** 043002

[12] T Pohl T P and Rost J M 2004 *Phys. Rev. Lett.* **92** 155003

[13] Robicheaux F and Hanson J D 2002 *Phys. Rev. Lett.* **88** 055002

[14] Mazevet S, Collins L A and Kress J D 2002 *Phys. Rev. Lett.* **88** 0550001

[15] Hung J, Sadeghi H, Schulz-Weiling M and Grant E R 2014 *J. Phys. B: At. Mol. Opt. Phys.* **47** 155301

[16] Mansbach P and Keck J 1969 *Phys. Rev.* **181** 275

[17] Roberts J L, Fertig C D, Lim M J and Rolston S L 2004 *Phys. Rev. Lett.* **92** 253003

[18] Vanhaecke N, Comparat D, Tate D and Pillet P 2005 *Phys. Rev. A* **71** 013416

[19] Walz-Flannigan A, Guest J, Choi J H and Raithel G 2004 *Phys. Rev. A* **69** 63405

[20] Gallagher T 1994 *Rydberg Atoms* (Cambridge: Cambridge University Press)

[21] McQuillen P, Strickler T, Langin T and Killian T C 2015 *Phys. Plasmas* **22** 033513

[22] Choi J H, Guest J, Povilus A, Hansis E and Raithel G 2005 *Phys. Rev. Lett.* **95** 243001

[23] Choi J H, Guest J, Hansis E, Povilus A and Raithel G 2005 *Phys. Rev. Lett.* **95** 253005

[24] Hu S, Vrinceanu D, Mazevet S and Collins L 2005 *Phys. Rev. Lett.* **95** 163402

[25] Pohl T, Sadeghpour H and Gabrielse G 2006 *Phys. Rev. Lett.* **97** 143401

[26] Robicheaux F 2004 *Phys. Rev. A* **70** 022510
[27] Guest J, Choi J H and Raithel G 2003 *Phys. Rev. A* **68** 022509
[28] Topcu T and Robicheaux F 2006 *Phys. Rev. A* **73** 022509

Can X-ray pulses for Ultrafast Microscopy be focused with a Kirkpatrick-Baez-optics?

Thomas received his MSc degree in Physics from the Ruhr-Universitt Bochum in 2014. In his bachelor thesis he worked on the galactic outflow of starburst galaxies and presented his results at the Annual Meeting of the German Astronomical Society in Tbingen 2013.

In his master thesis he analyzed the structure of bow shocks around run-away stars. In a collaboration between the Astronomical Institute and colleagues of the chair of Theoretical Space and Astrophysics he provided data on a promising bow shock candidate in order to simulate its astrosphere. He has co-authored a paper on these simulations.

During his time at the Astronomical Institute he gained experience in teaching and outreach by being a teaching assistant of two lectures on Astronomy and working with school classes at the Planetarium Bochum.

T. Wodzinski

Instituto de Plasmas e Fusão Nuclear, Instituto Superior Tecnico, Avenue Rovisco Pais, 1049-001 Lisboa, Portugal

E-mail: `thomas.wodzinski@tecnico.ulisboa.pt.`
September 2015

Abstract. Focusing of X-ray pulses is necessary to perform Ultrafast Microscopy. A Kirkpatrick-Baez (KB) setup has been realized in the L2I lab of the Group of Lasers and Plasmas of IPFN at IST. An optical laser was used to test the focusing performance. With a motorized mount it was possible to optimize the focal spot and reduce the aberrations. The reliability of a wavefront sensor to measure the quality of the focus has been compared to CCD measurements, resulting in comparable results. An estimated increase of fluence for a XUV pulse of a factor 1000 after passing through the KB setup can be reported.

1. Introduction

1.1. Motivation

In order to perform attosecond microscopy it is necessary to have laser pulses with short wavelengths. In the L2I lab of the Group of Lasers and Plasmas (GoLP) of IPFN at IST, high harmonic generation is used to create pulses in the XUV range (10 nm to 121 nm) with wavelengths as short as 20.6 nm [1].

So called 'X-ray optics' are applicable in the range from XUV to X-rays. Having lenses in the soft X-ray region is difficult, since materials are strongly absorbing. Focusing of soft X-rays requires therefore other solutions. One possibility is to make use of the growing reflectivity of mirrors when they are hit by X-rays in a low angle of incidence (see figure 1).

We want to investigate the ability of a Kirkpatrick-Baez (KB) mirror pair in focusing an X-ray beam generated by high harmonics. During this project we are focusing an optical beam coming from a Helium-Neon laser.

In the experimental setup for the X-ray beam it will not be possible to measure the quality of the beam in the focal spot directly with a camera, since it will be placed in a vacuum chamber. Therefore we are measuring the properties of the beam with a wavefront sensor and comparing these measurements with images obtained with a CCD camera positioned at the focal plane.

Adjusting the mirrors by hand is not accurate enough for getting an optimal result. Therefore we are putting the mirrors into motorized mounts, which will additionally allow to remotely adjust the mirrors in the X-ray setup.

1.2. Kirkpatrick-Baez optics

1.2.1. Principle
Kirkpatrick and Baez proposed in 1948 a combination of two sequentially arranged curved mirrors to focus X-ray light [2]. The beam hits both mirrors at a grazing incidence. This makes use of the fact, that the reflectivity of mirrors increases with the angle of incidence becoming smaller (see figure 1). The database for *X-ray Interactions With Matter* at the *Center for X-ray Optics* [3] provides information about the reflectivity of a thick SiO_2 mirror, used in this experiment. At grazing incidence of $\theta = 10°$ X-rays with a wavelength of $\lambda = 30$ nm (XUV) have a reflectivity of 60 % (see figure 1).

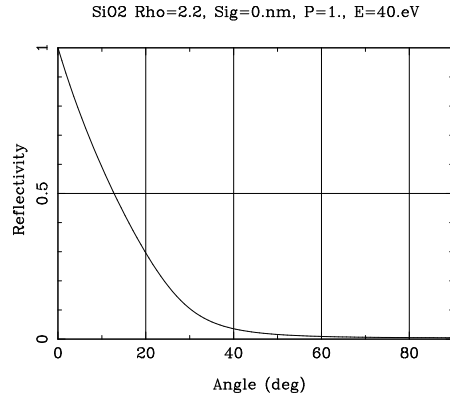Figure 1: Calculated reflectivity in dependence of angle of incidence of X-rays with a wavelength of $\lambda = 30$ nm for a thick SiO_2 mirror (from [3]). With lower angle of incidence the reflectivity increases.

The two mirrors are set up orthogonally to each other (see figure 2). This way, the horizontal line focus created by one mirror together with the vertical line focus by the other mirror will create a point focus if they are arranged in such a way, that their focus points match. The focal length $f_{grz}(\theta)$ under a grazing incident angle θ is given for a curved mirror with a focal length f by:

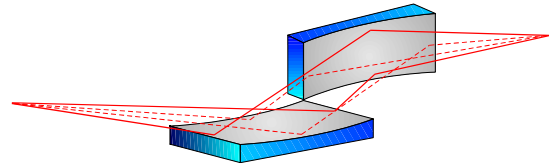$$f_{grz}(\theta) = f \cdot \sin \theta \tag{1}$$

Figure 2: Principle of Kirkpatrick-Baez-optics. Arrangement of two concave mirrors at small grazing angles. (Figure adapted from [4].)

KB mirrors are working with the principle of total reflection. Other devices working on other principles, like diffractive zone plates and refractive lenses are more difficult to use in preserving the wavefront and creating precise alignments. KB optics are the most promising option for focusing hard X-rays [5]. Their principle of grazing incidence reflection has an even higher efficiency for light in the XUV range.

1.2.2. Expected aberrations The line focus used in the KB-optics is a result of an aberration called astigmatism. Together with coma, these two major aberrations will be expected to appear in the measurements.

Astigmatism When a laser beam is hitting a curved mirror off-axis, in our case in an grazing incidence angle of $10°$, the circular beam is projected in from of an ellipse on the surface of the mirror. The rays from the major and minor axis of the ellipse will focus at different positions, leading to a horizontal and vertical line focus (see figure 3).
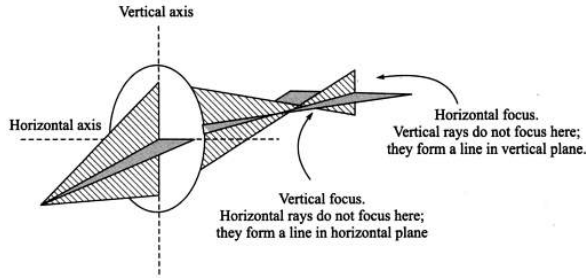
Figure 3: Astigmatism is the result of a beam hitting the surface of the mirror off-axis. Due to the elliptical shape of the beam projected on the mirror, a horizontal and vertical line focus is created. (Figure adapted from [6, p.180].)

Coma Like Astigmatism, comatic aberration is the result of the laser beam hitting the mirror off-axis. The beam is focused asymmetrically at different locations of the image plane. The further off-axis the rays are hitting the mirror, the larger images they form. The resulting shape resembles comets, which lead Astronomers to name this aberration accordingly [6, p.179].
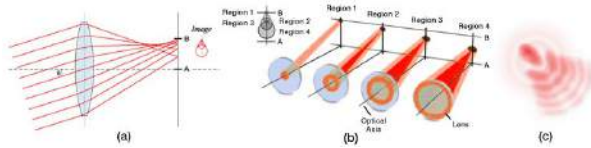

Figure 4: Illustration of the aberration coma. An off-axis beam is focused asymmetrically at different locations of the image plane. (Figure adapted from [7])

1.3. Strehl ratio

The quality of the focused beam can be described by the Strehl ratio (SR). It is defined for a beam in focus

as [8]:

$$SR = \frac{\text{peak intensity of measured beam}}{\text{peak intensity of theoretical beam}} \tag{2}$$

We compare the SR calculated by the Wavefront Sensor software with the one determined from the CCD image.

1.4. Wavefrontsensor

A wavefrontsensor delivers information about the intensity and phase of a beam. We used a PHASICS SID4 wavefrontsensor. It is working on the principle of lateral shearing interferometry.

2. Experimental setup

A Helium-Neon laser emits a beam with a wavelength of $\lambda = 632\,\text{nm}$. Figure 5 shows the path of the beam in the complete setup. After passing a beam expander it is guided with mirrors until it reaches the setup for the KB-optics, also shown in figure 6 from the side and from the top. It consists of two planar mirrors PM1 and PM2 which pre-compensate the beam in such a way, that it will go again after passing through the actual KB-optic consisting of two spherically curved mirrors CM1 and CM2, with a radius of curvature of $r_{\text{CM1}} = 3\,\text{m}$ and $r_{\text{CM2}} = 2\,\text{m}$, respectively.
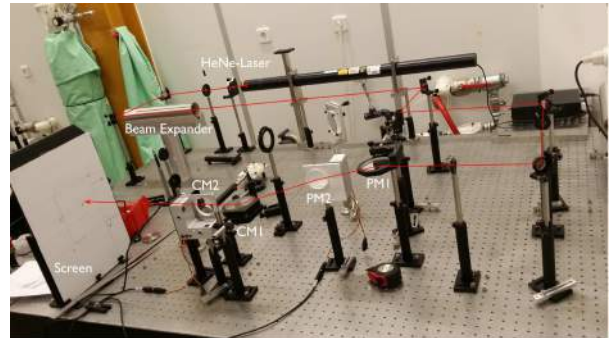

Figure 5: Experimental setup showing the beam of a He-Ne laser being expanded and guided to the setup for the KB optics. Two planar mirrors PM1 and PM2 are precompensating the beam, so that it will go straight again after leaving the KB optic with two curved mirrors CM1 and CM2. The angle of the mirrors is determined by calculating the necessary deflection for an angle of $10°$ on a screen. The mirrors PM2 and CM2 are placed into motorized mounts for better adjustment of the focus.

According to expression 1, the expected focal length for a grazing angle of $10°$ for both curved mirrors is presented in table 1.

The alignment procedure is realized by calculating the necessary deflections of the beam on a screen. After
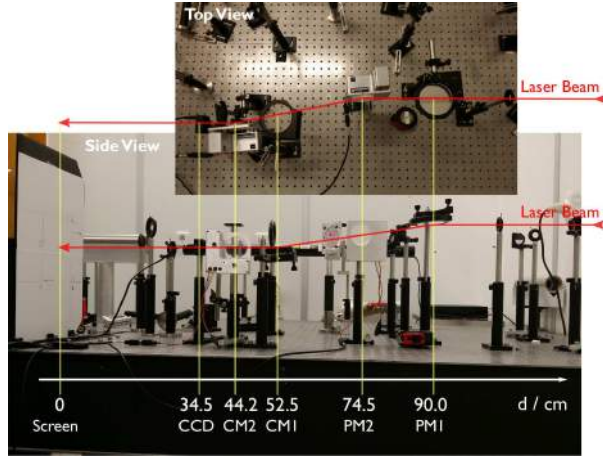
Figure 6: Side and top view of the experimental setup

Table 1: Calculated focal lengths of the two spherical mirrors under a grazing incidence angle of $\theta = 10°$ and the focal lengths determined in the experiment.

Mirror	CM1	CM2
r/m	3	2
f/cm	1.5	1
$f_{\text{grz}}(10°)$/cm	26	17
$f_{\text{grz}}(\text{exp})$/cm	18	9

fixing the position of the first planar mirror PM1, the necessary deflection for an angle of 10° is marked on the screen and the angle of the mirror adjusted accordingly. This process is repeated for the other mirrors. The positions illustrated in figure 6 for the two KB mirrors CM1 and CM2 vary slightly from these values. In order to achieve a good focus the position and angles are adjusted, which leads to focal lengths of 18 cm for CM1 and 9 cm for CM2 (see figure 7). This results in a beam leaving the KB that is not longer going straight.

The vertically aligned curved mirror CM2 of the KB as well as the corresponding pre-compensating planar mirror PM2 are placed into motorized mounts in order to adjust the beam focus more precisely.

3. Data analysis

3.1. CCD camera

The size of the elongated focal spot at Full width at half maximum (FWHM) is determined by fitting Gaussian to line profiles after rotating the image to align the major and minor axis (see figure 9). We estimate a spot size at FWHM of around $42\,\mu\text{m} \times 72\,\mu\text{m}$.

The diameter Δ of a diffraction-limited focal spot can be estimated by

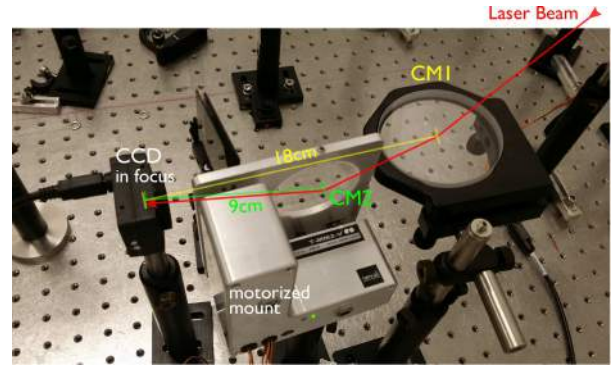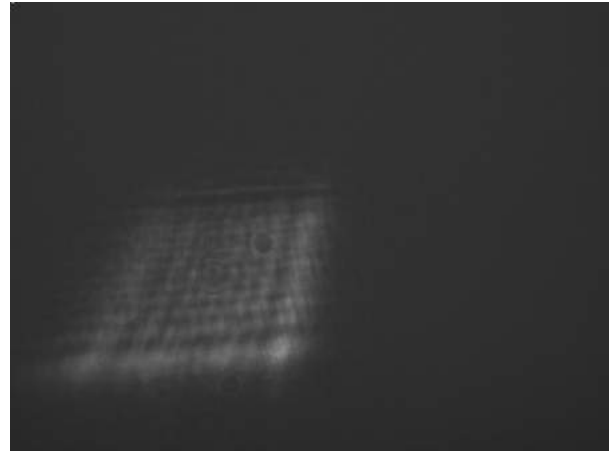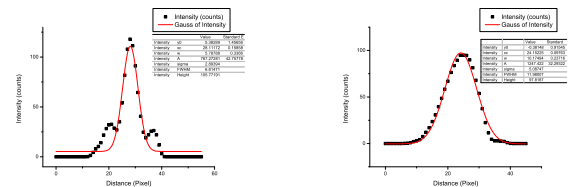$$\Delta = 1.44 \times \frac{\lambda}{d/f} \tag{3}$$

Figure 7: Up close view on the KB optics. The focal positions of both mirrors match and the CCD camera is positioned at this focus. Displayed are the experimental focal lengths for $\theta = 10°$. The focus in the experiment is found to be at 18 cm from CM2.

Figure 8: Image of the CCD camera positioned out of focus after best adjustment in focus. (24 cm from CM2 out of focus).

(a) Minor Axis FWHM = 7 px = 42 μm

(b) Major Axis FWHM = 12 px = 72 μm

Figure 9: Fitting of a Gaussian to the minor and major axis of the focal spot to determine the respective FWHM. We determine a size at FWHM of around $42\,\mu\text{m} \times 72\,\mu\text{m}$.

with the focal length f and aperture diameter d [9].

In order to calculate the Strehl ratio according

to equation 2, we have to determine the theoretical peak intensity. Figure 10 shows a comparison between the measured CCD image and a Gaussian, which approximates the theoretical spot. Due to the two focal lengths of the two mirrors of the KB optic, we calculate with equation 3 a spot size of $7.3\,\mu m \times 14.6\,\mu m$.

The expression for the 2D-Gaussian is:

$$I_{\text{theory}} = I_{\text{theory},0} \exp\left(-\left(\frac{(x-x_0)^2}{2\sigma_x{}^2} + \frac{(y-y_0)^2}{2\sigma_y{}^2}\right)\right) \quad (4)$$

with

$$\sigma = \frac{\Delta}{2.35482} \quad (5)$$

The theoretical peak intensity $I_{\text{theory},0}$ is determined by adjusting its value until the number of counts in the FWHM area matches the experimental one. This leads to a Strehl ratio of $SR \approx 4\,\%$.
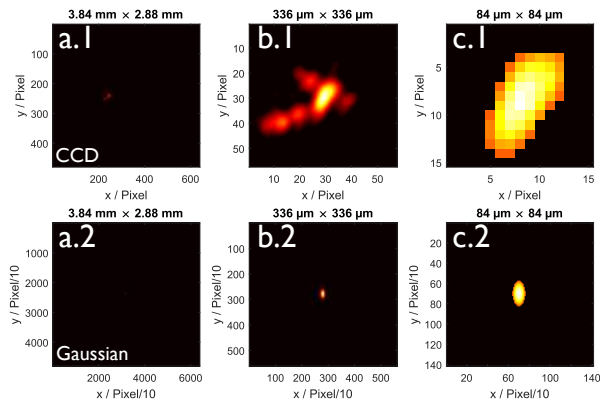

Figure 10: Comparison between actual CCD image (top, index 1) with theoretical image approximated by a Gaussian (bottom, index 2). From left to right: **(a)** Full chip ($3.84\,mm \times 2.88\,mm$), **(b)** Magnified ($336\,\mu m \times 336\,\mu m$), c) just those pixels, that have a value higher than half of the maximum intensity; to determine the FWHM.

3.2. Wavefront Sensor

The intensity and phase profile measured with the wavefront sensor away from the focus can be seen in figure 11. The shape of the intensity profile matches the one measured with the CCD camera away from the focus.

The wavefront sensor software calculates various beam parameters (see table 2). The calculated minimum waist from the software is determined to $2W_0 = 498\,\mu m$. This differs largely from the value determined by measuring the FWHM from the CCD image. There we determine a spot size of $42\,\mu m \times 72\,\mu m$, which is by a factor of 10 smaller. A possible explanation can be found by looking at the
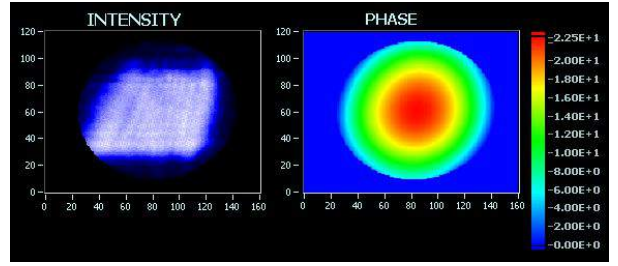

Figure 11: Intensity and phase measured with the wavefront sensor outside of the focus

determined waist profile by the software (see figure 12 and table 2). The minimum waist $2W_0$ in x-direction differs by a distance of $20\,mm$ from the one in y-direction. The software might be interpreting the KB-optics consisting of two mirrors as one single lens and tries to fit the minimum waist accordingly, which results in a value that is not accurate. The software documentation does not offer enough information regarding the calculations it is performing. The Strehl Ratio is calculated to a value of $4\,\%$ and matches the one calculated from the CCD image (see section 3.1).

The software also calculates a far-field image, which is supposed to give the image at the focal plane. Comparing this estimated image away from the focal spot with the one taken with the CCD camera (see figure 13), shows a lack of similarity. The reason for this might be the same as the one given for the inaccurate calculated minimum waist. The fact, that we are using to mirrors, each creating a big astigmatism, might confuse the software.

The major aberrations predicted to appear in the section about the KB optics (see section 1.2.2) are confirmed by the software in calculating the Zernike-coefficients, representing different aberrations (see table 3). Defocus is the strongest one and prevents us from seeing the effects of astigmatism in the phase profile (see figure 11). There is also coma, but astigmatism is around a factor of 10 stronger.
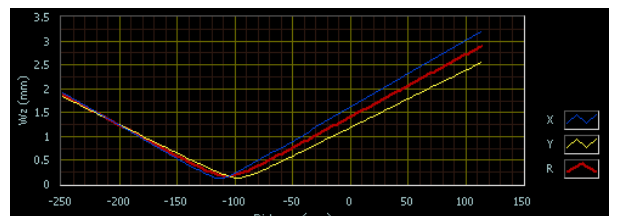

Figure 12: Waist profile determined by the wavefront sensor software. Blue and yellow show the waist diameter in x and y direction, respectively. The red plot shows it in radial direction. The minimal waist in x and y is $20\,mm$ apart.

Table 2: Beam parameters determined by the Wavefrontsensor software

Parameters	Unit	R	Min	Max
M^2	–	8.344111		
PtV	λ	22.528		
RMS	λ	5.897		
Strehl Ratio	%	4		
$2W_0$	mm	0.498130	0.255377	0.262385
z_0	mm	-105.873542	-113.193238	-97.295733
z_R	mm	19.053480	9.051823	10.898754
$2W$	mm	2.812398	3.203687	2.357022
Divergence	mrad	13.071879	14.106375	12.037383
Azimuth NF	°	14.759688		
Azimuth FF	°	-7.975810		

Table 3: Zernike coefficients calculated by the wavefront sensor software. Defocus is the strongest aberration. Astigmatism is also high compared to coma.

Defocus	Astig 0°	Astig 45°	Coma X	Coma Y	Spherical aberr.
-5.793	-0.931	0.564	0.081	0.000	0.023

4. Discussion

4.1. Further improvement

There is still room for improving the KB setup. As can be seen in figure 12 (see section 3.2), the focal spots of the KB mirrors CM1 and CM2 are still 2 cm apart from each other.

The trapezoidal shape of the image out of focus (see figure 8), and the fact that the structures stretching out from the hot spot in the image in focus (see figure 13) shows, that the KB-mirrors are still not orthogonal enough. Improving their orthogonality requires to adjust the pre-compensation of the beam with the planar mirrors PM1 an PM2. By doing so, it is possible to increase the Strehl ratio from 4 % up to 20 %.

Unfortunately, these measurements have not been recorded and the KB setup was not fixed in this improved position, which did not allow to quickly reproduce these results.

4.2. Increased fluence

For knowing, weather using this KB setup is useful for focusing X-rays, we can estimate the resulting increase of fluence.

Given the reflectivity of these mirrors at an angle of 10° and a focus with a Strehl ratio of 4 % to 20 %, we can estimate the number of photons per cm^2 for an incoming beam of 10^9 photons.

Assuming a wavelength of the high harmonic XUV pulse of $\lambda \approx 30$ nm we read from figure 1 a reflectivity of $r \approx 60$ %.

Energy of $\lambda \approx 30$ nm photons:

$$E = 41.3 \, \text{eV} = 6.621\,486 \times 10^{-18} \, \text{J} \tag{6}$$

The fluence of the beam before entering the KB optics is:

$$H_0 = \frac{10^9 \, \text{photons}}{\pi \cdot (9.5/2 \, \text{mm})^2} \tag{7}$$

$$= 1.44 \, \text{cm}^{-2} \cdot 10^9 \, \text{photons} \tag{8}$$

$$H_0 = 9.535 \times 10^{-9} \, \text{J} \, \text{cm}^{-2} \tag{9}$$

After passing the two spherical mirrors the number of photons has decreased from 10^9 photons to:

$$0.6 \times 0.6 \times 10^9 \, \text{photons} = 0.36 \times 10^9 \, \text{photons} \tag{10}$$

Reading the number of counts inside the FWHM and comparing it with the total number of counts in the focal plane, we get a ratio of counts inside the spot of 28 %. We get an estimation of the photons in the focal spot of 10 % from the initial number:

$$0.28 \times 0.36 \times 10^9 \, \text{photons} \approx 0.10 \times 10^9 \, \text{photons} \tag{11}$$
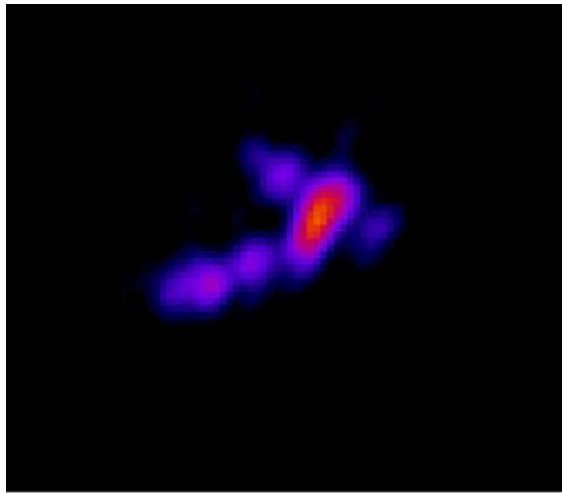
The fluence of the focal spot is:

$$H_{\text{spot}} = \frac{0.10 \times 10^9 \, \text{photons}}{\pi \cdot 35 \, \mu\text{m} \cdot 60 \, \mu\text{m}}$$

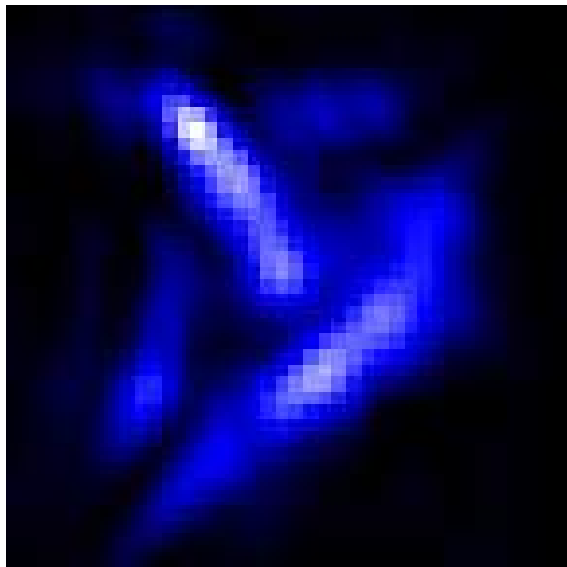$$10.03 \times 10^{-6} \, \text{J} \, \text{cm}^{-2} \tag{12}$$

This is a factor of

$$\frac{H_{\text{spot}}}{H_0} = \frac{10.03 \times 10^{-6}}{9.535 \times 10^{-9}} \approx 1052 \tag{13}$$

We therefore gain a factor of 1000 higher fluence by using this KB setup. Calculating the value for the

(a) CCD image

(b) Far-Field from Wavefront-Sensor

Figure 13: Comparison of the actual CCD image in the focal plane with the calculated Far-Field image from the Wavefront-Sensor software.

20 % Strehl ratio is difficult, because we do not have measurements from where we can read the number of photons in the FWHM of the corresponding spot. But we can estimate, that we would get a factor of around 5 times more fluence than with a Strehl ratio of 4 %.

4.3. Perspectives

The next steps following this project would be the following:

At first, the motor movements have to be calibrated, so that one has a relationship between the adjusted angles and motor steps.

With this information the change of aberrations introduced by the movement of the KB-mirror can be mapped against the motor movements.

Similar to an experiment realized by [8], this will allow to design a procedure to systematically increase the focus and reduce the aberrations to a minimum.

5. Bibliography

[1] Fajardo M Coherent x-ray sources
[2] Kirkpatrick P and Baez A V 1948 *JOSA* **38** 766–773
[3] X-ray database of the center for x-ray optics
[4] Ehlers B and Verman B 2010 Investigation of aberrations of kirkpatrick-baez mirrors *SPIE Optical Engineering+ Applications* (International Society for Optics and Photonics) pp 78020F–78020F
[5] Yumoto H, Mimura H, Koyama T, Matsuyama S, Tono K, Togashi T, Inubushi Y, Sato T, Tanaka T, Kimura T *et al.* 2013 *Nature Photonics* **7** 43–47
[6] Neeraj M *Applied Physics for Engineers* (PHI Learning Pvt. Ltd.) ISBN 9788120342422
[7] Thorlabs inc
[8] Planchon T A, Mercere P, Cheriaux G and Chambaret J P 2003 *Optics communications* **216** 25–31
[9] Sauneuf R, Dalmasso J M, Jalinaud T, Le Breton J P, Schirmann D, Marioge J P, Bridou F, Tissot G and Clotaire J Y 1997 *Review of scientific instruments* **68** 3412–3420
[10] Attwood D Ast210/ee213 - soft x-rays and extreme ultraviolet radiation
[11] Barty A, Küpper J and Chapman H N 2013 *Annual review of physical chemistry* **64** 415–435
[12] Chao W, Harteneck B D, Liddle J A, Anderson E H and Attwood D T 2005 *Nature* **435** 1210–1213
[13] Chapman H N and Nugent K A 2010 *Nature photonics* **4** 833–839
[14] Chen B, Dilanian R A, Teichmann S, Abbey B, Peele A G, Williams G J, Hannaford P, Van Dao L, Quiney H M and Nugent K A 2009 *Phys. Rev. A* **79** ISSN 1094-1622
[15] Christian M and Markus O 2010 *X-Ray Optics and Instrumentation* **2010**
[16] Corkum P B and Krausz F 2007 *Nat Phys* **3** 381387 ISSN 1745-2481
[17] Eden J G 2004 *Progress in Quantum Electronics* **28** 197–246
[18] Ge X, Boutu W, Gauthier D, Wang F, Borta A, Barbrel B, Ducousso M, Gonzalez A, Carré B, Guillaumet D *et al.* 2013 *Optics express* **21** 11441–11447
[19] Geary J 1995 *Introduction to Wavefront Sensors* SPIE tutorial texts (SPIE Optical Engineering Press) ISBN 9780819417015
[20] Ice G E, Budai J D and Pang J W 2011 *Science* **334** 1234–1239
[21] Kapilashrami M, Liu Y S, Glans P A and Guo J 2015 *Soft X-Ray Spectroscopy and Electronic Structure of 3d Transition Metal Compounds in Artificial Photosynthesis Materials* (Springer)
[22] Krause J L, Schafer K J and Kulander K C 1992 *Physical Review Letters* **68** 3535
[23] Krausz F and Ivanov M 2009 *Reviews of Modern Physics* **81** 163
[24] Kroch S Astigmatism
[25] Last A X-ray optics
[26] Liu W, Ice G E, Tischler J Z, Khounsary A, Liu C, Assoufid L and Macrander A T 2005 *Review of Scientific Instruments* **76** 113701 ISSN 0034-6748
[27] Mercère P, Idir M, Moreno T, Cauchon G, Dovillaire G, Levecq X, Couvet L, Bucourt S and Zeitoun P 2006 *Optics letters* **31** 199–201

[28] Midorikawa K 2011 *Jpn. J. Appl. Phys.* **50** 090001 ISSN 1347-4065

[29] Mills B 2009 *Focussing and Diffraction using a High Harmonic Source* Ph.D. thesis

[30] Osterhoff M 2012 *Wave Optical Simulations of X-ray Nano-focusing Optics* Göttingen Series in X-ray Physics (Univ.-Verlag Göttingen) ISBN 9783863950545

[31] Popmintchev T, Chen M C, Arpin P, Murnane M M and Kapteyn H C 2010 *Nature Photonics* **4** 822–832

[32] Popmintchev T, Chen M C, Popmintchev D, Arpin P, Brown S, Ališauskas S, Andriukaitis G, Balčiunas T, Mücke O D, Pugzlys A *et al.* 2012 *science* **336** 1287–1291

[33] Ravasio A, Gauthier D, Maia F, Billon M, Caumes J, Garzella D, Géléoc M, Gobert O, Hergott J F, Pena A *et al.* 2009 *Physical review letters* **103** 028104

[34] Roberts Jr L C, Perrin M D, Marchis F, Sivaramakrishnan A, Makidon R B, Christou J C, Macintosh B A, Poyneer L A, van Dam M A and Troy M 2004 Is that really your strehl ratio? *SPIE Astronomical Telescopes+ Instrumentation* (International Society for Optics and Photonics) pp 504–515

[35] Sakdinawat A and Attwood D 2010 *Nature photonics* **4** 840–848

[36] 2013 *Springer Series in Optical Sciences* ISSN 1556-1534

[37] Yamanouchi K and Midorikawa K (eds) 2012 *Multiphoton Processes and Attosecond Physics* (Springer Berlin Heidelberg) ISBN http://id.crossref.org/isbn/978-3-642-28948-4

[38] Phasics - wavefront sensors - lateral shearing interferometry, shack-hartmann wavefront sensors: Phasics